Interface modification by ion implantation and optical characterization of high-efficiency Cu(In,Ga)Se$_2$ solar cells

Dissertation zur Erlangung des akademischen Grades

doctor rerum naturalium (Dr. rer. nat.)

vorgelegt dem Rat der Physikalisch-Astronomischen Fakultät

der Friedrich-Schiller-Universität Jena

von Jakob Haarstrich

geboren am 7. Februar 1982 in Bergisch Gladbach

Gutachter:

1. **Prof. Dr. Carsten Ronning**   Friedrich-Schiller-Universität Jena

2. **Prof. Dr. Rüdiger Goldhahn**   Otto-von-Guericke-Universität Magdeburg

3. **Prof. Dr. Susanne Siebentritt**   Universität Luxemburg

Tag der Disputation: 24.11.2011

Contents

1 Introduction

The need for the use of renewable energy sources for the global energy supply is widely accepted in our society – more than ever after the recent accidents in the nuclear power station of Fukushima and on the oil rig "Deep water horizon" in the Gulf of Mexico. Renewable energy already plays an important role in the global electricity supply (18% share in 2009) and photovoltaic energy is becoming an essential part of it (2% of all renewable sources at a growth rate above 50% per year) [Ren10]. In Germany, already 2% of the electricity is supplied by photovoltaics [BMU10]. The potential of solar energy conversion can be illustrated very easily: The sun supplies the earth with the enormous amount of $3 \cdot 10^{24}$ Joules per year, which is approximately 10,000 times more than the global annual energy consumption. Therefore, it would be enough to cover 0.1% of the Earth's surface (approximately the land area of Spain) with solar cells with 10% conversion efficiency. Today, the terrestrial use of solar cells and modules is mainly limited by the high cost of these devices.

One approach to reduce the costs is the development of thin-film solar cells. The advantages of these devices are their low material usage, the low energy consumption for fabrication and the application of large scale integrated fabrication processes. Among the different thin-film technologies, $Cu(In,Ga)Se_2$ based structures are well established: the heterostructure device $ZnO/CdS/Cu(In,Ga)Se_2/Mo$ shows the best performance of all thin-film solar cells. Efficiencies of 20.3% on laboratory scale [Jac10], 17.2% in a pilot line [Sol11] and 15.7% in large-scale production [Mia10] have proven the high-level performance of the $Cu(In,Ga)Se_2$ technology, but still there is much room for improvement and a need for fundamental research.

Three different issues of current $Cu(In,Ga)Se_2$ research will be addressed in this work:

(1) High-efficiency $Cu(In,Ga)Se_2$ solar cells use a CdS buffer layer deposited in a chemical bath (CBD). The use of the CBD-CdS buffer layer in the structure is undesirable from a technological as well as an environmental perspective. Therefore, the replacement of the CBD-CdS buffer layer by a non-toxic alternative buffer is one of the major challenges for the research and development of the thin-film solar cell based on the $Cu(In,Ga)Se_2$ material. Many Cd-free alternative buffers {e.g. In_xS_y [Har96], $Zn(S,O,OH)$ [Bha04]} and other deposition processes (e.g. sputtering [Min01; Gri10], ILGAR [Fis10], thermal evaporation [Pis09], atomic layer deposition [Nag03]) have been tested, but there is still a lack in

efficiency, reproducibility and stability of the alternative buffer devices compared to that of the CdS buffer devices. The advantage of the CdS buffer is suggested to be due to the beneficial formation of an inverted buffer/absorber interface during the growth of the buffer from the chemical bath solution [Kle01]. Hence, it may be possible to completely omit the buffer layer if this inversion is deliberately introduced to the interface. In Chapter 4, the effect of low-energy ion implantation of n-type dopants in the absorber layer on material properties is investigated in order to prepare completely buffer-free $Cu(In,Ga)Se_2$ solar cells.

(2) The absorber layer of high-efficiency $Cu(In,Ga)Se_2$ solar cells exhibits an in-depth band-gap grading, which is discussed to be beneficial for solar cell performance [Dul01]. It has also been shown that a careful design of the grading is necessary [Glo05b; Gre09] and, hence, an efficient control of the grading by different characterization techniques is needed. One standard technique to study the optical and the defect properties of semiconductors is the analysis of the luminescence (about 40 articles every year only in this material system). In the recent literature, numerous investigations on the luminescence of Ga-graded $Cu(In,Ga)Se_2$ thin-films can be found, which interpret the spectra in relation to the integral stoichiometry and, thus, disregard the presence of the grading [Con09; Ish09; Slo10; Paw11; Zac11]. In Chapter 5, the influence of the grading on the luminescence properties is discussed and a model is developed, which establishes a basis for the application of luminescence methods on band-gap graded thin-films. In order to lay a sound foundation, the physical principles of the luminescence technique (with a focus on cathodoluminescence) are described in Section 2.3.

(3) Solar cells based on $Cu(In,Ga)Se_2$ absorbers are discussed to be limited in efficiency by severe band-gap as well as electrostatic fluctuations or barriers at grain boundaries [Wer05; Sie11]. These inhomogeneities are found to be stronger at lower deposition temperatures (smaller grain sizes and increased segregation of In- and Ga-rich phases) [Kes04; Rud05; Ish08; Kau09]. As the best cells are still produced on Na-containing float glass (soda lime glass) [Rep08; Jac10], the deposition temperature on glass is limited by the softening point of the substrate between 500 and 550°C. Therefore, a high-temperature resistant, Na-containing glass has been developed by Schott AG Mainz [Win09] in order to investigate the deposition at temperatures above 600°C. In Chapter 6, high-temperature absorbers deposited at a nominal substrate temperature of 610°C are compared with absorbers from the standard process at 530°C. This comparison also serves as an application of the model developed in Chapter 5.

2   Background: Cu(In,Ga)Se$_2$ for photovoltaics and cathodoluminescence of Cu(In,Ga)Se$_2$

In this chapter, a review is given on the technological and physical basis of the main topics addressed in this thesis:

- the Cu(In,Ga)Se$_2$ material properties, especially the role of the homogeneity of the absorber layer for solar cell performance (Section 2.1),
- the functionality of the buffer/absorber interface (Section 2.2) and
- the fundamentals of cathodoluminescence and its application to Cu(In,Ga)Se$_2$ (Section 2.3).

The chapter gives an overview of the current status in research and defines the starting point of the investigations done in this thesis.

2.1   Basics of Cu(In,Ga)Se$_2$ solar cells

After describing the basic material properties of the Cu(In,Ga)Se$_2$ (Section 2.1.1) and describing the set-up and functionality of a typical Cu(In,Ga)Se$_2$ solar cell (Section 2.1.2), the role of the absorber homogeneity is described in some more detail in Section 2.1.3.

2.1.1   Material properties of Cu(In,Ga)Se$_2$

The ternary compounds CuInSe$_2$ and CuGaSe$_2$ crystallize in the chalcopyrite structure [Sha75] with a tetragonal lattice, in which each cation is surrounded by four anions and vice versa (Grimm-Sommerfeld rule [Gri26]). The CuInSe$_2$-CuGaSe$_2$ system shows high solubility at high temperatures [Mar97], which allows for the formation of the quaternary compound Cu(In,Ga)Se$_2$ in the full range of In-Ga-stoichiometry, but also phase separation is observed at typical thin-film deposition temperatures below 600°C [Mar97].

As shown in Figure 2.1(a), the pseudo-binary phase diagram of CuInSe$_2$ allows for some deviations from nominal 1:1:2 stoichiometry [Haa98]: The chalcopyrite phase (α-phase) shows a very high tolerance in stoichiometry: It exists in a region of the Cu-content from about 22% to 25% at common deposition temperatures around 500°C. Cu$_2$Se segregates in the region of higher Cu-content, the α-phase and the β-phase (CuIn$_3$Se$_5$) co-exist on the Cu-poor side.

In Cu(In,Ga)(S,Se)$_2$ thin-films used for high-efficiency solar cells, a gradient in band-gap is intentionally introduced in the absorber layer. This gradient is introduced by the variation of the ratio [Ga]/([Ga]+[In]) (hereafter: GGI) and/or [S]/([S]+[Se]) with depth [Ram03a; Bär04; Kau09;

Sey11]. Inserting sulfur or gallium into CuInSe$_2$ leads to an increase of the band-gap energy (CuInSe$_2$ $E_{gap} = 1.046\ eV$, CuGaSe$_2$ $E_{gap} = 1.731\ eV$ [Mud98], CuInS$_2$ $E_{gap} = 1.555\ eV$ [Bin82] at $T \leq 10\ K$); thus, the grading in composition also introduces a grading in the band-gap. The increase of the band-gap by the addition of Ga is shown experimentally and theoretically to primarily occur in the conduction band position while the valence band remains mainly unaffected, whereas in case of the addition of sulfur in CuInSe$_2$ (instead of selenium), the band-gap widening occurs rather equally in both the conduction and the valence band [Wei95; Tur01].

Due to its direct band-gap, the material shows very high absorption coefficient α_{CIGSe} in the order of $10^5\ cm^{-1}$ [Fon81]. Therefore, most of the incident light with photon energies above the band-gap is absorbed in a layer with a thickness of $d \approx 0.5\ \mu m$. This high absorption allows to work with low absorber thicknesses and, thus, short transport lengths in solar cell devices made from the material [Fon81]. The luminescent properties of Cu(In,Ga)Se$_2$, which are essential for this work are discussed in more detail in Section 2.3.4. The doping properties are described in Section 2.2.2 and 2.2.3. For a more extended description of structural and electronic properties and phase formation of Cu(In,Ga)Se$_2$ thin-films for solar cell applications, the reader is referred to compendia [Sha75; Roc91; Mar97; Rau99b].

2.1.2 Cu(In,Ga)Se₂ solar cells

Cu(In,Ga)Se$_2$ thin-film solar cells consist of a number of thin layers (thicknesses in the order of $1\ \mu m$, see also Figure 3.1). which are deposited onto a rigid (glass) or flexible (polyimide, metal foil) substrate. First, the non-transparent back-contact, typically molybdenum, is deposited by RF- or DC-sputtering. It is covered by the p-type chalcopyrite absorber film, which is commonly applied by co-evaporation of the constituent elements (see e.g. [Kau09]) or by selenization of metallic precursors (reactive annealing) [Pal04]. The heterojunction is formed between the absorber and a very thin n-type buffer layer (mostly CdS) and a heavily doped (n$^+$-type) wide-band-gap semiconductor, which serves as a transparent front-contact (mainly ZnO:Al).

Figure 2.1(b) shows a schematic band-edge diagram of the device. The light is absorbed in the p-type absorber layer and photo-excited electrons drift into the n-type region once they have diffused into the built-in field of the heterojunction – the built-in field in the interface region of the p- and n-type layers (p-n-junction) separates the photo-generated positive and negative charges. In a heterojunction device, band-offsets in the conduction and/or valence band may occur at the p-n-interface, which may act as a barrier for charge carriers as discussed in detail in Section 2.2.
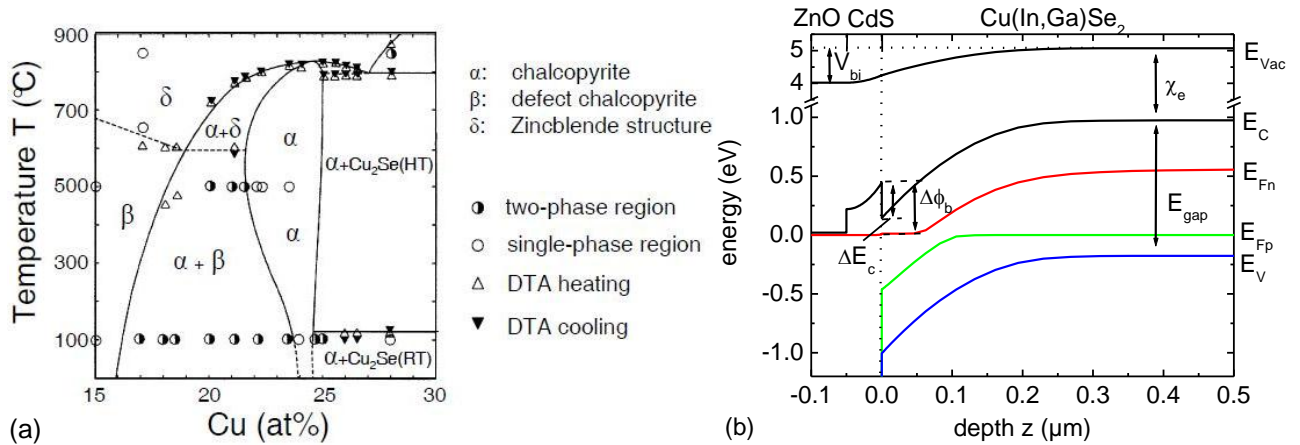
Figure 2.1: (a) Phase diagram for the quasi-binary systems of Cu_2Se-In_2Se_3 obtained by differential thermo-analysis (DTA) taken from [Haa98]. (b) Band-diagram of the near-surface region of a ZnO/CdS/Cu(In,Ga)Se₂ solar cell; indications are explained in the text.

2.1.3 Homogeneity of the Cu(In,Ga)Se₂ absorber

Thin-film solar cells based on Cu(In,Ga)Se₂ have recently reached an efficiency of 20% [Jac10] – but this still is far from the efficiency limits calculated from physical principles [Sie11]. In recent literature, it has been suggested that the homogeneity of the Cu(In,Ga)Se₂ absorber layer may be a key issue in production of high-efficiency thin-film solar cells [Bau05; Gra05; Wer05; Mat07; Mal09; Rau09; Bro10; Haf10; Sie11]. The influence of band-gap- as well as electrostatic fluctuations in the grains (potential fluctuations due to localized charges) or at grain boundaries and dislocations (charged defects) are discussed therein. Theoretical investigations clearly show that lateral variations of the local open-circuit voltage can deteriorate the global solar cell performance [Kar02; Kan07; Mal09]. Experimentally, the global loss of open circuit voltage has been quantified from the lateral variation of the quasi-Fermi-level splitting by measuring the lateral variation of the PL intensity [Bau05]. Also, a lateral variation of the photon energy of the dominating DA-transition was observed in CL measurements [Rom03a] at low temperatures.

The origin of lateral inhomogeneities is also discussed [Gra05; Mat07; Mal09; Sie11]. Fluctuations of the local band-gap on a length scale below 100 *nm* may be produced by variations in composition or alloy disorder [Mat07; Mal09]. Inhomogeneities of the chemical potential can be caused by fluctuations in the local electronic quality of the material and might appear on a length scale of a few microns [Gra05]. The role of grain boundaries in Cu(In,Ga)Se₂ thin-film solar cells and different grain boundary models are also widely discussed, which include strong band-bending at grain boundaries [Rom03a; Han06; Het06; Abo09; Nic09; Rau09; Haf10; Sie10]. Although it seems that grain boundaries in Cu(In,Ga)Se₂ are much less harmful than in other semiconductor materials, a beneficial effect of a large number of grain boundaries is rather unlikely [Sie10]. All these fluctuations are presumed to possibly cause a loss in open-circuit voltage of up to 100 *mV*.

Furthermore, the band-gap grading is subject to critical examinations: It has been shown by simulation and experiment that the vertical Ga-grading in the absorber can be beneficial, but can also be detrimental for solar cell performance [Glo05b; Lun05; Gre09]. The Ga-grading is inherent to the deposition process and although different shapes of the grading can be found in different processes [Bas96; Han07; Web07], there always seems to be a tendency to phase separation, which is often explained by the differences in the diffusion behavior of gallium and indium (kinetic explanation). If this is the case, the interdiffusion can presumably be enhanced at increasing deposition temperatures – this trend is also observed in low-temperature deposition processes [Kes04; Rud05; Web07; Kau09]. Another explanation for the observed disorder may be that the phase separation is energetically favored as recently suggested by Ludwig et al. [Lud10], but also in this case the disorder is observed to decrease at higher temperatures. The experimental investigation of high-temperature deposition processes on soda-lime glass is hindered by the softening point of the glass substrate.

In Chapter 6, the material properties of absorber layers deposited at temperatures above 600°C on soda lime glass are investigated for the first time. This was possible only after the development of a suitable glass substrate. The influence of the deposition temperature on the homogeneity both laterally and vertically is examined using different methods.

2.2   Interface engineering in Cu(In,Ga)Se$_2$ solar cells

Thin-film solar cells are based on p-n-heterojunctions and, thus, on the functionality of the interface between p- and n-type semiconductor. High-efficiency Cu(In,Ga)Se$_2$ thin-film solar cells commonly use a thin CBD-CdS buffer as an n-type partner to the p-type Cu(In,Ga)Se$_2$ absorber layer. The functionality of the buffer layer has been subject to numerous studies in the last decade (reviewed in [Sie04a; Har05; Nag10]). The principle functionality of the buffer/absorber interface is described in Section 2.2.1 as discussed in recent literature. As this work aims on manipulation of the interface by extrinsic doping of the near-surface region of the absorber by ion implantation, the doping properties of Cu(In,Ga)Se$_2$ are described in Section 2.2.2; the literature on ion implantation in Cu(In,Ga)Se$_2$ is revised in Section 2.2.3.

2.2.1   The buffer-absorber interface in Cu(In,Ga)Se$_2$ solar cells

The basic function of the buffer layer is to transmit most of the light and to form the p-n-heterojunction such that low interface recombination is obtained. To achieve this, the following issues are discussed to be essential:

(1) A large band-gap for high optical transmission.

(2) A complete coverage of the surface (at low film thickness) to prevent shunting.

(3) No surface damage due to the deposition process (e.g. sputtering) [Rau99b; Can00; Shi08] to prevent a high near-interface trap density.

(4) A good lattice match to reduce the interface trap density [Abo05].

(5) Adjusted conduction band off-set ΔE_C to Cu(In,Ga)Se$_2$ [Kle01; Min01; Glo05c; Gri10; Kie10]. An electron barrier $\Delta\phi_b$ [$\Delta E_C \leq \Delta\phi_b$, see Figure 2.1(b)] below +0.5 eV is found to be benign or even beneficial for device performance [Nie95; Kle01; Glo05c; Pud05], while a larger barrier can obstruct the current flow over the. A negative band off-set (cliff) leads to a reduced barrier for interface recombination [Kle01].

(6) A stable interface inversion, i.e. the electron quasi-Fermi level E_{Fn} being close to the conduction band E_C at the interface [Nak99; Kle01; Glo05c; Kie10]. The inversion has been shown to effectively reduce interface recombination also at high trap densities, because the minority carriers (electrons) generated in the absorber are majority carriers at the interface: in other words, the inversion leads to a strong reduction of the number of holes being available for recombination [Kle01].

A thin layer of CdS fulfills all of these criteria as a buffer on low-GGI Cu(In,Ga)Se$_2$ absorbers when prepared by chemical bath deposition [Con02; Har05; Nag10]:

(1) It is a direct semiconductor with a band-gap of 2.4 - 2.5 eV [Dut58], which leads to current losses of only about 1 $mA\ cm^{-2}$ [Heg04].

(2) Full coverage is already reached at a thickness of 10 nm [Rau99b].

(3) The chemical bath is a soft-deposition technique and the CdS layer protects the surface during subsequent ZnO sputter deposition.

(4) A very good lattice match is found, which may be associated with a low trap density [Abo05].

(5) The conduction band off-set ΔE_C changes with the GGI due to the variation of the electron affinity χ_e [Wei95; Tur01]; a (beneficial) conduction band off-set (moderate spike) is found for a GGI below 0.5 [Sch04; Glo05c].

(6) The interface is assumed to be inverted, but it is still under discussion if this is due to a natural n-type surface layer in the absorber (Cu-poor surface) and the influence of surface oxygenation [Cah91; Sch93; Rau99a] or the in-diffusion of Cd into the absorber surface [Nak98; Hes99; Lia03; Abo05; Coj11].

A typical band structure of the interface region of a ZnO/CdS/Cu(In,Ga)Se$_2$ solar cell under AM1.5 illumination is shown in Figure 2.1(b). The bands feature discontinuities at both interfaces with the

conduction band off-set ΔE_C leading to an electron barrier $\Delta\phi_b$. If the electron quasi-Fermi level E_{Fn} is close to the conduction band at the interface ($\Delta E_C \approx \Delta\phi_b$), the barrier is reduced and interface recombination is minimized due to inversion. In addition, the built-in voltage V_{bi}, defined by the drop of the vacuum-level E_{vac} over the p-n-junction ($V_{bi} = 0.9\text{-}1.0$ V [Gla05; Sie11]), almost completely drops in the absorber in case of an inverted interface leading to improved collection and an enlarged width w_{SCR} of the space charge region (SCR).

If the CdS buffer is omitted and the interface is formed directly between ZnO and the absorber, strongly decreased device performance is observed (e.g. [Can00; Pla03; Hul11]). While Platzer-Björgman et al. [Pla03] presume the losses in V_{oc} to be due to the cliff in the conduction band, Canava [Can00] finds the lower efficiencies to be also due to the sputtering damage by comparing devices with ZnO-window prepared by sputtering and atomic layer epitaxy (ALE). Moreover, surface inversion may not be given in this configuration [Pla03].

In this work, an alternative approach of interface engineering is investigated, which has been proposed by Klenk [Kle01] and is based on point (6) in the above lists: If a surface layer of the absorber is intentionally inverted to n-type, the p-n-junction position is shifted away from the semiconductor (hetero-)interface into the absorber, which is commonly called a buried interface. An n-type surface layer of homogeneous thickness in the absorber might also be able to fulfill most of the above conditions, but the thickness of the inverted layer needs to be sufficiently small (< 50 nm), because carriers generated in the n-type part are not expected to contribute to the current collection [Kle01]. Sputtering damage at the interface will occur and the lattice match might not be as good as for CdS, but as the p-n-junction is moved away from the interface, a high defect density at the interface might not be harmful. The conduction band off-set between ZnO and Cu(In,Ga)Se$_2$ is found to be rather small with a tendency to a cliff [Sch96; Pla03; Wei03]. The controlled inversion of the near-surface region of the absorber is investigated in Chapter 4 and shall be reached by extrinsic doping (see next section).

2.2.2   Doping of Cu(In,Ga)Se$_2$

The Cu(In,Ga)Se$_2$ films are intrinsically p-type when grown Cu-poor or under sufficient Se-excess [Tel72; Mig75; Yu75a]. The p-type doping is assumed to be due to doping by Cu-vacancies (V_{Cu}), which act as shallow acceptor-like defects [Zha98]. The high tolerance of the compound to stoichiometry variations (see Section 2.1.1) is commonly explained by the formation of the electronically neutral defect-pair ($2V_{Cu}+In_{Cu}$) [Zha98]. The formation energy of the Cu-vacancy is found to be very low and to depend on the Fermi-level position [Zha98; Per05], which can explain the high degree of self-compensation found for the material [Dir98; Sie06]. Due to the complexity

of the deposition process and the strong self-compensation, a doping profile based on intrinsic doping will not be controllable on a depth scale below 100 *nm* [Sie10].

Extrinsic n-type doping is also complicated by the strong self-compensation. The doping of CuInSe$_2$ has been found both theoretically and experimentally to be still easier than that of the wider band-gap compound CuGaSe$_2$ due to differences in the V$_{Cu}$-formation energy [Sch00b; Sie02; Per05]. N-type doping has been achieved in p-type Cu(In,Ga)Se$_2$ using cadmium [Mig75; Tel76; Yu76a], zinc [Mig75; Tel76; Yu76b; Sug00; Nis03; Gri07; Sug08], chlorine [Yu76b], copper [Zeg95] and hydrogen [Yak94; Ott01; Ott03]. For Cu-poor and In-rich material as it is used for solar cell fabrication, Persson et al. [Per05] find n-type doping using group two elements (e.g. Cd, Zn, Mg) to be most favorable, because the dopant will preferably occupy the Cu-sites (II$_{Cu}$) due to a high number of Cu-vacancies being available. But also in this case, doping is predicted to be very ineffective (doping efficiency about 1%) due to high self-compensation and compensation by group-II-elements on In-sites II$_{In}$; even lower doping efficiencies are found in experiment [Yu75b; Yu76b]. The choice of group-II-atoms as dopants is supported by the fact that in well-working buffer/absorber interfaces using CdS or Zn-compound buffers, the interface type-conversion at the surface is presumed to be connected to Zn [Pla03; Gri07; Shi08] or Cd [Nak00; Lia03; Coj11] diffusion into the absorber surface (see Section 2.2.1). This assumption is supported by experiments with a Cd- or Zn-containing partial electrolyte (PE) baths (like a CdS or ZnS bath, but without the sulfur compound). The PE bath is shown to clearly improve the solar cell performance [Ram03b], which has been explained by a change in the conduction band off-set and the near-interface Fermi-level position (inversion) [Ram03b; Wei03]. Even p-n-homojunctions have been fabricated in p-type Cu(In,Ga)Se$_2$ by Zn- or Cd-in-diffusion or implantation [Yu75a; Yu75b; Mat87; Sug00; Sug08]. Extrinsic n-type doping has been successfully performed in Cu(In,Ga)Se$_2$ either during the growth process [Sug00], after growth by subsequent thermal in-diffusion [Mig75; Yu75a; Sug08] or by ion implantation [Yu75b; Yu76b; Sch99].

2.2.3 Ion implantation and defect annealing

The method of ion implantation is a standard method in material science and is also applied for doping in industrial semiconductor device fabrication [Nas06]. The method of ion implantation allows to adjust the implantation depth (determined by the ion energy) independently from the ion concentration (determined by the ion fluence) and, therefore, a high-precision control of the implantation profile. As mentioned in Section 2.2.1, the buried-junction has to be very shallow below the interface in order to prevent current losses. At the same time, very high dopant concentrations may be needed due to the strong self-compensation of the material, which can also be

easily obtained by ion implantation. Thus, ion implantation is the method of choice for investigating the influence of near-interface doping in Cu(In,Ga)Se$_2$ solar cells.

Ion implantation is always accompanied by the creation of implantation defects and subsequent annealing of the defects will be necessary for re-crystallization of the host-lattice and dopant activation [Nas06]. Successful n-type doping has been achieved in Cu(In,Ga)Se$_2$ applying annealing temperatures of 300 - 400°C for 10 - 60 *min* [Yu75b; Yu76b; Sch98] – thus, these temperatures are presumed to be sufficient for the recovery of the damage and electrical activation of the dopants.

The adjustment of an appropriate doping profile is very important for device functionality. If the accuracy of the implantation profile shall be preserved for the doping profile, the required annealing step must not lead to considerable diffusion of the dopants. As the thickness of the n-type layer should be smaller than 50 *nm*, also the diffusion length L_{diff} should be below this value. According to

$$L_{diff} = \sqrt{D\, t_{ann}} \qquad\qquad\qquad (2.1)$$

[Sze81], a critical diffusion length $L_{diff,crit}$ of 50 *nm* is reached after an annealing time t_{ann} of 30 *min* for a diffusion coefficient D_{crit} of 10^{-14} *cm^2 s^{-1}*.

The diffusion of Zn [Sug00; Nis03; Ben05; Shi08; Sug08] and Cd [Kaz79; Nak98; Nak00; Lia03; Kij08; Rus09] in Cu(In,Ga)Se$_2$ has been investigated in the literature, but these studies have lead to strongly deviating results. Earlier investigations on the motion of p-n-homojunctions in CuInSe$_2$:Cd presumably measure the out-diffusion of Se rather than the in-diffusion of Cd [Yu75a; Tel76; Mat87]. Therefore, no reliable values can be given here, but the data suggest that diffusion coefficients of 10^{-14} *cm^2 s^{-1}* may be already reached at temperatures of 200 - 300°C (data of [Ben05] shown in Section 4.3); activation energies in the order of 1 - 1.5 *eV* are found in [Kaz79; Nis03; Ben05] (partially obtained by re-evaluation of the data). Very recent and unpublished results [Bas11; Hie11] seem to deliver a more reliable basis, but cannot be cited here. Furthermore, the diffusion coefficient of atoms in an ion-implanted, "amorphous" material may significantly differ from the one measured on undisturbed single-crystals [Nas06].

2.3   Fundamentals of cathodoluminescence and application to Cu(In,Ga)Se$_2$

Luminescence techniques are used to analyze the radiative recombination (optical transitions) in semiconductors. That way, one can gain access to band-gap-energies and defect-related levels. In this work, luminescence methods shall be applied to band-gap graded thin-films; therefore, the principle processes taking place in semiconductors during luminescence measurements from excitation to detection are described in this chapter: the generation of electron-hole pairs (Section

2.3.1), the motion of electrons and holes within their lifetime (Section 2.3.2), the recombination processes (Section 2.3.3) and signal detection (Section 2.3.5). While most points apply to all luminescence techniques, the excitation issue is discussed with a special focus on the cathodoluminescence. Additionally, an overview is given on the luminescence of Cu-poor Cu(In,Ga)Se$_2$ (Section 2.3.4).

2.3.1 Excitation and distribution of charge carriers

All luminescence techniques such as cathodoluminescence (CL), photoluminescence (PL) or electroluminescence (EL) are based on the detection of photons in the UV, VIS or IR range, which originate from recombination of electron-hole pairs (e-h-pairs) in the sample. In CL, e-h-pairs are generated using a focused electron beam. The beam of a scanning electron microscope (SEM) is ideal for this purpose, as it offers high lateral resolution for spatially resolved CL measurements [Yac86]. The electron energy E_e, typically between 1 and 30 keV, is sufficient to excite electrons from the valence to the conduction band for any semiconductor. The average energy needed for the creation of an e-h-pair E_{EHP} is empirically found to be approximately $E_{EHP} \approx 3\ E_{gap}$ [Kle68]. Thus, a single electron with an energy of $E_e = 10\ keV$ is capable to excite approximately 3000 e-h-pairs in a Cu(In,Ga)Se$_2$ sample with $E_{gap} \approx 1.15\ eV$. The energy transferred from the incident electrons to the sample is furthermore reduced due to backscatter processes. Thus, the integral number of excited e-h-pairs per incident electron G_0 can be calculated to [Par07]

$$G_0 = \frac{E_e}{E_{EHP}} \left(1 - \frac{E_{be}}{E_e} Y_{be}\right).$$
(2.2)

Here, E_{be} is the average energy per backscattered electron and Y_{be} the backscattering yield. The average backscattering energy and yield can be determined using the Monte-Carlo code "**Mo**nte **CA**rlo **SI**mulation of ElectroN Trajectory in **SO**lids" (Casino) [Dro07] to $E_{be} \approx 0.7\ E_e$ and $Y_{be} \approx 0.35$ for Cu(In,Ga)Se$_2$, both numbers being only weakly dependent on E_e and GGI.

In order to estimate the injection density in the layer, it is necessary to account for the spatial distribution of the generation density $g(x,y,z)$ per incident electron with

$$G_o = \iiint g(x, y, z)\, dxdydz\,.$$
(2.3)

The injection density Δn can then by calculated to be

$$\Delta n(x, y, z) = \frac{I_b \tau_e}{e} g(x, y, z) \equiv N_e\, g(x, y, z)$$
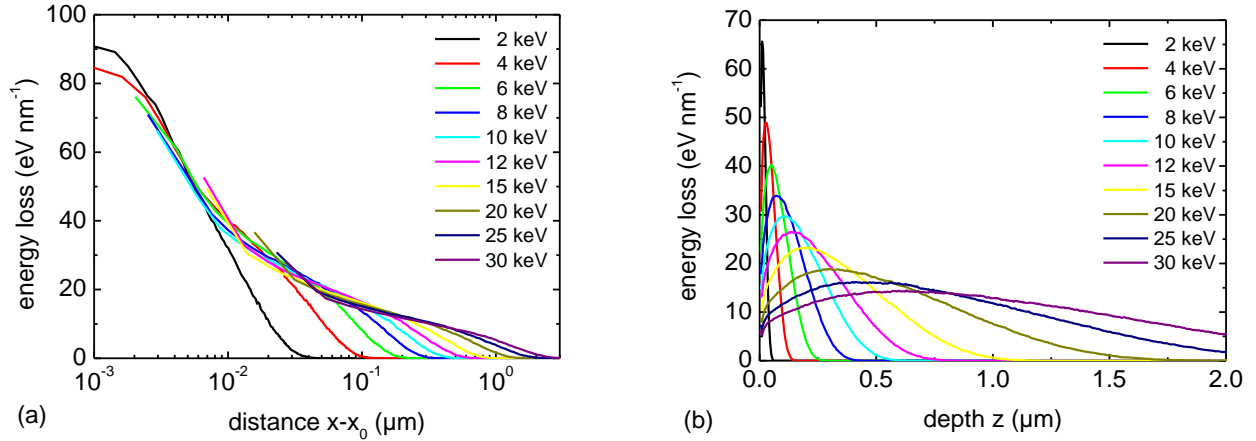(2.4)

Figure 2.2: Lateral profile (a) and depth profile (b) of the energy loss in Cu(In$_{0.7}$Ga$_{0.3}$)Se$_2$ for different electron energies.

defining N_e as the number of electrons hitting the sample at the beam current I_b during one minority carrier lifetime τ_e (e stands for the elementary charge).

Using Casino [Dro07], the three dimensional distribution of the energy loss (associated with the e-h-pair generation distribution [Tot98]) can be determined for the impact of an electron into the surface ($z = 0$) at a certain spot (x_0, y_0). The lateral and the in-depth distribution $\varepsilon(x-x_0)$ and $\varepsilon(z)$ are displayed for a set of electron energies E_e for a Cu(In,Ga)Se$_2$ sample with a GGI of 0.3 in Figure 2.2 (a) and (b), respectively. Similar results were obtained using Monte-Carlo methods in [Kni09] and by the use of empirical expressions [Eve71; Rec00]. The depth profile $\varepsilon(z)$ gives an estimation of the excitation depth z, which can be useful for depth-resolved CL analysis (see also Section 5.3.1); the lateral profiles $\varepsilon(x-x_0)$ give a lower limit of the resolution of lateral CL profiles (see also Section 5.2). From those profiles, the 90%-quantile is obtained for each electron energy and displayed in Figure 2.3(a).
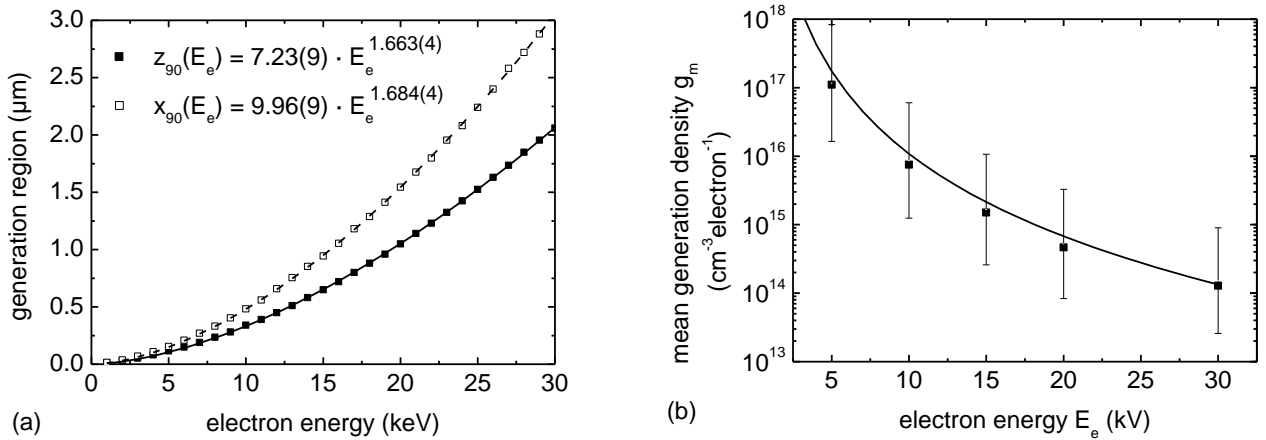
Figure 2.3: (a) Lateral (x_{90}) and vertical (z_{90}) 90%-quantile of the energy deposition as a function of the electron energy E_e approximated by a power law (inset, electron energy in keV, quantiles in nm) determined from Figure 2.2 (note that the values account for both sides in case of the lateral profile). (b) Mean generation density as calculated from Eq. (2.6) ($g_{m,K-O}$, solid line) and from Monte-Carlo simulations ($g_{m,MC}$, squares). The error bars give the width of the distribution w_g.

An approximation of the mean generation density per electron g_m can be obtained by estimating the spatial extent of the excitation region using the Kanaya-Okayama-range R_{K-O} [Kan82]

$$R_{K-O} = \frac{27.6 \cdot A \cdot E_e^{1.67}}{Z^{0.89} \cdot \rho} nm \, , \qquad (2.5)$$

with the density ρ (in $g \; cm^{-3}$), average atomic mass A (in atomic mass units) and average atomic number Z of the sample and the electron energy E_e (in keV). This leads to an mean generation density per electron $g_{m,K-O}$ of [Par07]

$$g_{m,K-O} = \frac{G_o}{\frac{4}{3}\pi\left(\frac{1}{2}R_{K-O}\right)^3} \qquad (2.6)$$

corresponding to a proportionality $g_{m,K-O} \sim E_e^{-4}$. Data obtained from Eq. (2.6) using $A = 80$, $Z = 35$ and $\rho = 5.75 \; g \; cm^{-3}$ are shown in Figure 2.3(b) (solid line). Similar values are found for CuInSe$_2$ in [Sch91].

An alternative approach has been developed within this work evaluating the three dimensional energy loss profiles obtained from Casino-simulations and is described below. To give a rough picture of the energy loss distribution, the slice at $y = y_0$ is displayed in a two dimensional plot in Figure 2.4(a) for $E_e = 10 \; keV$. The color code gives the e-h-pair generation density $g(x,y_0,z)$ per incident electron and per cm^3 averaged over a large number of electrons ($N_e = 10^7$). It demonstrates that $g(x,y,z)$ varies over four orders of magnitude (10^{14} - $10^{18} \; cm^{-3}$ per electron). This means that there is not one fixed value g_m, but a broad distribution of local generation densities $g(x,y,z)$.

The distribution $g(x,y,z)$ obtained from the simulation is composed of a discrete distribution of densities g_i for every volume ΔV_i. Mean values $g_{m,MC}$ are determined by calculating the number of e-h-pairs $g_i\Delta V_i$ created at or below a certain generation density g_k in the whole volume investigated normalized to the overall number of excited e-h-pairs:

$$R(g_k) \equiv \frac{\sum_{i:g_i\in(0,g_k)} g_i\Delta V_i}{\sum_{i:g_i\in(0,\infty)} g_i\Delta V_i} \, . \qquad (2.7)$$

This distribution $R(g_k)$ is displayed in Figure 2.4(b) for a set of different electron energies E_e. For each electron energy, the figure displays a sigmoid curve, which shifts to higher densities with decreasing electron energies. Discrete steps are observed at high generation densities due to the finite segmentation of the simulated volume. The mean generation density $g_{m,MC}$ can be defined by $R(g_{m,MC}) \equiv R(g_{m,0.5}) = 0.5$. The width of the distribution is defined by the ratio
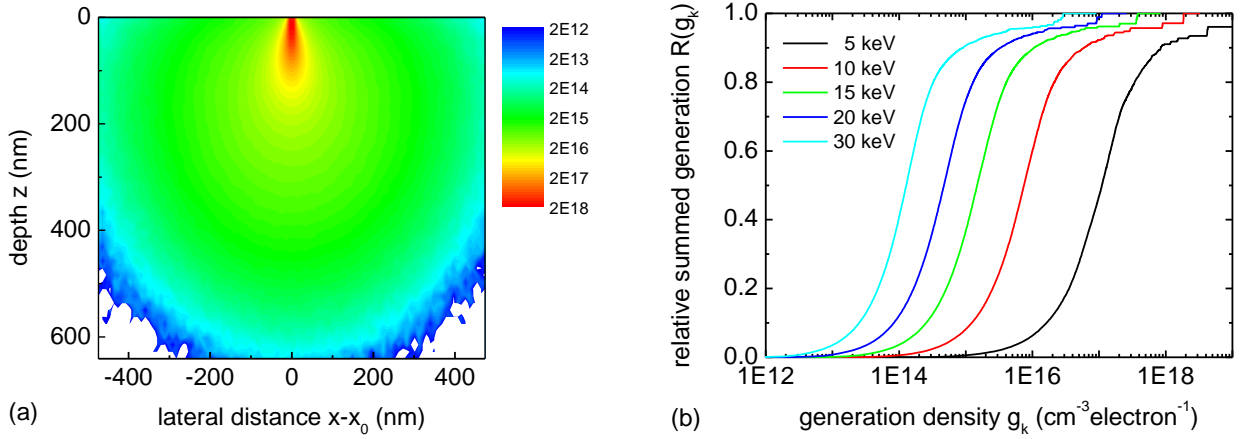
Figure 2.4: (a) Two-dimensional plot of the e-h-pair generation density at $y = y_0$ $g(x,y_0,z)$ and an electron energy of $E_e = 10\,keV$ with the color code giving the generation density g in cm^{-3} $electron^{-1}$. The simulation was performed averaging over a large number of electrons ($N_e = 10^7$). (b) Sum of the generated e-h-pairs $R(g_k)$ as a function of the generation density g_k for a set of electron energies E_e.

$$w_g \equiv \frac{g_{m,0.9}}{g_{m,0.1}} \tag{2.8}$$

and gives an approximation of the variation of g within the excitation region. $g_{m,MC}$ is displayed as a function of E_e in Figure 2.3(b), the error bars correspond to the width of the distribution w_g. As the solid line represents the dependence obtained from Eq. (2.6), a very good agreement is found between the values determined by both methods ($g_m \equiv g_{m,MC} \approx g_{m,K\text{-}O}$). Thus, Eq. (2.6) gives an easy and very good approximation of the mean generation density; the more complex calculation based on Monte-Carlo-simulation yields additional information on shape and width of the distribution. It is found that a very large variation of the generation density (by a factor of 30 - 50) is present when using electron-beam injection methods.

The values for the mean generation density g_m can be used to estimate the injection level and the current-limit for low-injection conditions in electron-beam based methods. Low-injection conditions are given if the injected carrier density is small compared to the background doping level [Ber76], thus, in case of a p-type semiconductor, if

$$\Delta n \ll N_A \tag{2.9}$$

is valid. In this case, basic parameters of the semiconductor such as lifetime or mobility of charge carriers should be independent of the density of excited charge carriers [Ber76]. Combining Eqns. (2.4) and (2.9), the low-injection limit is obtained to

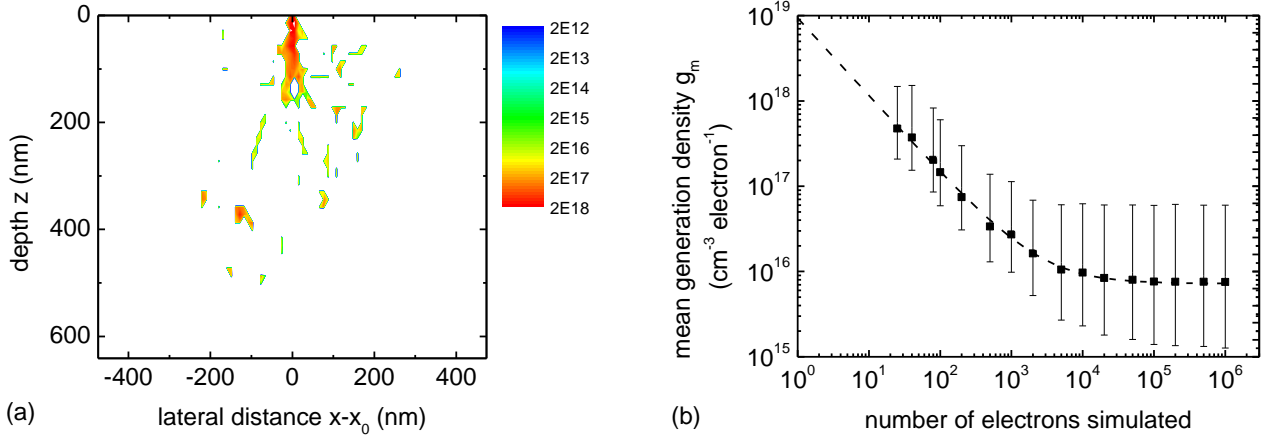$$I_{b,max} = \frac{N_A e}{\bar{g}(E_e)\tau_e}. \tag{2.10}$$

Figure 2.5: (a) Two-dimensional plot of the e-h-pair generation density at *y=0* *g(x,y₀,z)* with the color code giving the generation density *g* in *cm⁻³ electron⁻¹*. The simulation was performed averaging over a small number of electrons (*Nₑ = 25*). (b) Generation density per incident electron and *cm³* as a function of the number of simulated electrons *Nₑ* with the error bars denoting the width of the distribution *wₘ*.

Assuming an effective doping density of $N_A = 10^{16}\ cm^{-3}$ (see [Dir98; Cwi08; Rei10] and Section 4.4.2) and a minority carrier lifetime of about $\tau_e = 10\ ns$ [Ohn98; Pal04] for Cu(In,Ga)Se₂, an upper low-injection current limit of $I_{b,max}$ of about $20\ pA$ is obtained at $E_e = 10\ keV$. In electron beam induced methods such as CL [Rom03b; Rom03b] and electron beam induced current (EBIC) [Rec01; Bro10], higher beam currents are commonly used – thus, it is concluded that high-injection effects cannot be excluded using such beam currents.

There is only one study discussing experimental findings on the low-injection current limit [Sch91]. Here, a reduced current collection is found in junction-EBIC for beam currents above $25\ pA$ at $E_e = 10\ keV$ and $60\ pA$ at $E_e = 17\ keV$. These values fit very well with the data obtained from Eq. (2.10).

The results of the Monte-Carlo simulations in Figure 2.3(b) are obtained for a sufficiently high number of incident electrons, in this case $N_e = 10^6$ electrons were used. Using the parameters $I_b = 250\ pA$ (the standard beam current used in this thesis) and $\tau_e = 10\ ns$, approximately 15 electrons reach the sample during one e-h-pair lifetime ($N_e = 15$). Thus, there is no continuous distribution of the energy as displayed in Figure 2.4, but rather single electron tracks.

Simulations with Casino can be performed only for $N_e \geq 25$; the 2-D plot of $g(x,0,z)$ is displayed for $N_e = 25$ in Figure 2.5(a) with exactly the same scaling as Figure 2.4. As $g(x,y,z)$ equals zero for most of the volumes ΔV_i, most of the energy is deposited in areas with a very high energy density – this means a high concentration of e-h-pairs. In Figure 2.5(b), the mean generation density g_m is displayed as a function of the number of electrons N_e simulated (full squares). Again, the error bars in Figure 2.5(b) give the values of $g_{0.1}$ and $g_{0.9}$, respectively. The data points are approximated with a function of the type $y = a\,x^b + c$; while the generation rate reaches a constant level

($c \approx 7.5 \, 10^{15} \, cm^{-3} \, electron^{-1}$) for a large number of electrons ($N_e \geq 10^5$), it linearly ($b \approx -1$) increases for small numbers below $N_e = 500$:

$$g_m \sim N_e^{-1} \sim I_b^{-1}. \tag{2.11}$$

Introducing Eq. (2.11) in Eq. (2.4), the mean injection density Δn_m is shown to be independent of I_b for currents below 10 nA as displayed in Figure 2.6(a). The error bars denote the width of the distribution $w_{\Delta n}$, which is defined analogously to w_g in Eq. (2.8). The number of electrons N_e is interpreted in terms of the beam current by using Eq. (2.4) and assuming $\tau_e = 10 \, ns$. In the low-current regime, the single electron tracks are independent of each other and only for $N_e \geq 1000$ a significant overlapping leads to a linear increase of the mean injection density ($b \approx 1$). Thus, a minimum mean injection density can be obtained by fitting the data points in Figure 2.6(a) ($\Delta n_{m,min} = c$) and defined using Eq. (2.5) to

$$\Delta n_{m,min} = \Delta n_m(N_e = 1) = g_m(N_e = 1), \tag{2.12}$$

which yields $\Delta n_{m,min} = (1.4 \pm 0.3) \, 10^{19} \, cm^{-3}$ for $E_e = 10 \, keV$. A further decrease of the mean injection density is not possible. Note that this value is independent of the electron lifetime in the sample, but depends on material parameters [see Eq. (2.2) and Eq. (2.5)] and on the electron energy E_e, as shown in Figure 2.6(b).
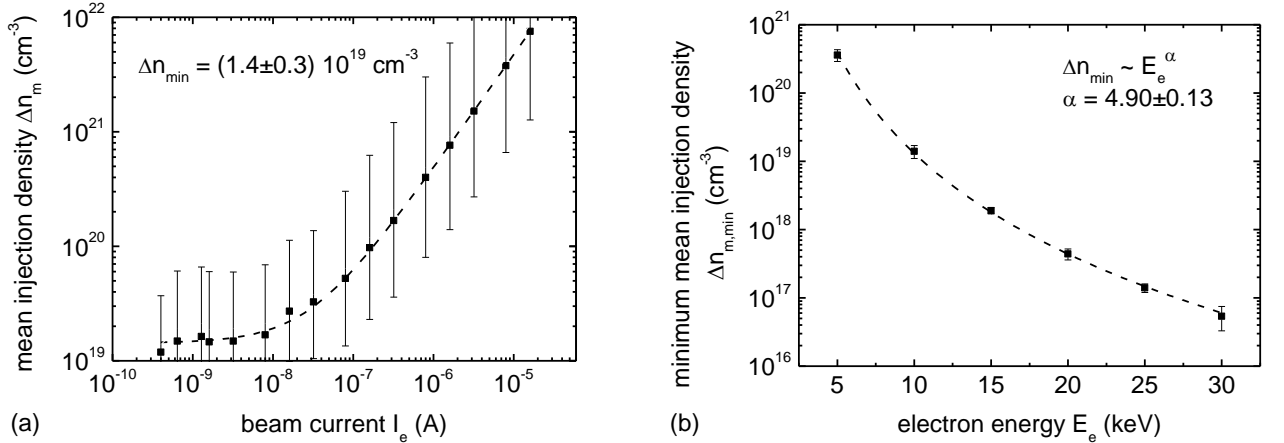
Figure 2.6: (a) Mean injection density Δn_m per cm^3 for an electron energy E_e of 10 keV as a function of beam current assuming a minority carrier lifetime τ_e of 10 ns with the error bars denoting the width of the distribution $w_{\Delta n}$. A constant minimum value $\Delta n_{m,min}$ is reached at low currents. (b) Minimum injection density $\Delta n_{m,min}$ as a function of the electron energy E_e and fitted by a power law.

2.3.2 Motion of charge carriers

Once e-h-pairs are generated, they will recombine with a characteristic lifetime in the semiconductor material. During their lifetime, they can be subject to drift and/or diffusion processes. Both mechanisms lead to the motion of charge carriers from their origin (spot of excitation). Since the

motion has not been considered in Monte-Carlo simulations and calculations in Section 2.3.1, the generation density profiles $g(x,y,z)$ are valid only for the moment of impact. For $t \geq t_0$, e-h-pairs will spread over the sample due to these transport processes. This means that the recombination may occur at a place different from the place of excitation. If charge carrier motion is present, the injection density becomes a function of time after the moment of impact t_0: $\Delta n = \Delta n(t-t_0)$.

Carrier diffusion processes will take place in any semiconducting material. The distance of transport can be described by the diffusion length L_{diff} of electrons and holes, respectively, defined by

$$L_{diff} = \sqrt{\frac{k_B T}{e} \mu_{e/h} \tau_{e/h}} \tag{2.13}$$

[Sze81]. The process is thermally activated and depends on the mobility μ and lifetime τ of the carriers in the sample. It has been shown that the diffusion length can be determined by CL methods [Zar89; Gus98], if the CL intensity emitted at one specified position is detected as a function of the spot of excitation. Since in common CL setups, the detection system usually detects the global intensity emitted from a large region of the sample, it is necessary to specially define the region of interest. This may be done by applying a thin metal mask [Zar89] or by using a well defined interface between two regions with different band-gaps. The latter mechanism has been recently used to determine the diffusion length in (Al,Ga,In)As nanowire heterostructures [Gus10].

Drift mechanisms only occur if an accelerating force is present. This may be the electric field in the SCR of a p-n-junction or an externally applied voltage, but also other forces on charge carriers can be present. If the material properties of the semiconductor vary with the depth z, Fonash [Fon81] finds in a very general one-dimensional approach (see Figure 2.7) the expression

$$j_n = e\mu_e n \frac{dE_{Fn}}{dz} - e\mu_e n S_e \frac{dT_e}{dz} \tag{2.14}$$

for the conduction-band current density. Herein, E_{Fn} stands for the electron quasi-Fermi level, T_e denotes the effective electron temperature and S_e the Seebeck coefficient. The effective electron temperature T_e can often be assumed to be equal to the lattice temperature $T_{lattice}$ and independent of z for a homogeneous bulk sample, but it might differ from the lattice temperature in high electric fields [Str62]. Thus, in the bulk, the effective force giving rise to an electron current in the conduction band is the gradient in the electron quasi-Fermi level.

This gradient can be analyzed according to $E_{Vac} = \chi_e + V_n + E_{Fn}$ (see Figure 2.7) to gain additional information on the origin of the force. Introducing this into Eq. (2.14) yields (for $T_e = $ const.) [Fon81]
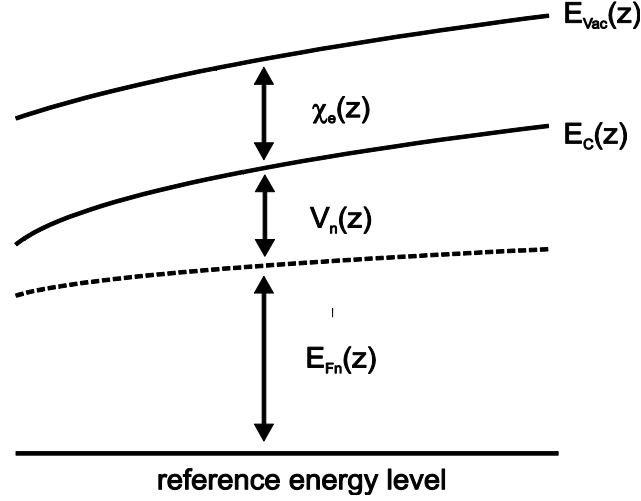
Figure 2.7: General semiconductor conduction band diagram with the vacuum energy level E_{Vac}**, the electron affinity** χ_e**, the electron quasi-Fermi level** E_{Fn} **and the energy** V_n **denoting the energetic distance of** E_{Fn} **and the conduction band** E_C **(according to [Fon81]). All parameters are allowed to vary with depth** z**.**

$$j_n = e\mu_e\left(n\,E - n\frac{d\chi_e}{dz} - kT_e n\frac{d(\ln N_c)}{dz} + kT_e\frac{dn}{dz}\right) \qquad (2.15)$$

for the conduction-band current density. Here, $E(z)$ is the electrostatic field, $\chi_e(z)$ the electron affinity and $N_C(z)$ the density of states in the conduction band. According to (2.15), the electron current density is driven by a total force

$$F_e = -e\left(E - \frac{d\chi_e}{dz} - kT_e\frac{d(\ln N_c)}{dz}\right), \qquad (2.16)$$

which acts on the electrons (drift) and by an electron concentration gradient (diffusion). The Eqns. (2.14) - (2.16) can be equally defined for the hole current in the valence band.

As described in Section 2.1.1, a gradient in the band-gap is present in Cu(In,Ga)Se$_2$ absorber layer for solar cell fabrication, which primarily occurs in the conduction band position: $dE_{gap}/dz \approx d\chi_e/dz$. As Cu(In,Ga)Se$_2$ absorber layers for solar cell application are p-type [Poo06], the minority carriers are the electrons and the current in the conduction band has to be considered. The standard grading in Cu(In,Ga)Se$_2$ solar cells is a so-called double-grading with an increase of the band-gap towards the front- and the back-contact [Ram03a; Bär04; Kau09; Sey11]. While the back-grading leads to improved collection (enhanced short-circuit current), the front-grading is supposed to minimize the recombination in the space charge region − thus, it increases the open-circuit voltage [Dul01]. According to Eq. (2.16), the gradient in the band-gap has physically the same effect on electrons in the conduction band as an electro-static field. The gradient in the band-gap induces a force on electrons in the conduction band, which leads to a drift towards the minimum of the band-

gap. As a first approach, the effective force present in the absorber layer (without p-n-junction) can be described by

$$F_e(z) \approx e\frac{d\chi_e(z)}{dz} = e\frac{dE_{gap}(z)}{dz} .$$
(2.17)

Additional forces can occur due to electrostatic charges on interfaces or the free surface (band-bending) and gradients in the density of states in the conduction band N_C or the electron temperature T_e. The field induced by the band-gap grading is commonly referred to as effective force field [Fon81] or quasi-electric field E_{qe} [Osi85]. The latter term will be used throughout this work.

The drift process can be characterized by the drift length L_{drift} of the electrons in the quasi-electric field E_{qe} within their lifetime τ_e

$$L_{drift} = v_{drift}\tau_e = \mu_e\tau_e E_{qe}$$
(2.18)

according to the Drude theory [Dru00]. Here, v_{drift} gives the drift velocity, which can be estimated to be up to $10^4\ m\,s^{-1}$ at room-temperature (T = 300 K) for an electron mobility of $100\ cm^2\ V^{-1}\,s^{-1}$ [Glo05a] and a maximum field of $1\ V\,\mu m^{-1}$ (as in the samples used, see Section 5.1). For a lifetime of $10\ ns$, a drift length of up to $100\ \mu m$ can be expected from Eq. (2.18), which is very large compared to the thickness of the Cu(In,Ga)Se$_2$ absorber layers.

The influence of charge carrier drift on luminescence in band-gap graded materials has already been discussed in the literature for III-V- and II-VI semiconductors [Kov81b; Car82; Osi82]. Kovalenko et al. [Kov81a] develop analytic methods for the determination of semiconductor properties (drift length, diffusion length, quasi-electric field, thickness of the graded layer, surface recombination) from graded-gap related phenomena, which than are applied to Al$_x$Ga$_{1-x}$As in [Kov81b]. These quantitative models, however, are limited to layers showing a linear variation of the band-gap with depth.

Coming back to the injection level calculations from Section 2.3.1, it can be assumed that the region of recombination may be by far larger than the excitation region itself. This may lead to a strong decrease of Δn_m within the time t-t_o. Thus, if one asks for the effective injection density, the time of interest t-t_o after the impact needs to be specified. For example, the emission energy of donor-acceptor transitions depends on the injection density Δn at the moment of recombination (as discussed in Section 2.3.3). Thus, an exact description of the injection density at the moment of recombination would require to solve the full transport equations in three dimensions including generation, recombination, drift and diffusion terms [Sze81] as described for example in [Lau09]. In a very first approach, the influence of drift and diffusion can be approximated by inserting either

2 L_{diff} or L_{drift} instead of R_{K-O} into Eq. (2.10). (if 2 L_{diff}, $L_{drift} > R_{K-O}$) in order to determine the mean generation density g_m.

2.3.3 Recombination processes in semiconductors

The generation of excess carriers (in this case by the electron beam) leads to a concentration of e-h-pairs above the equilibrium concentration; thus, increased recombination will occur. The energy difference of the initial and the final state can be emitted either radiatively (photons) or non-radiatively (phonons) − only the radiative recombination can be observed by luminescence techniques. In most cases, the non-radiative recombination is simply regarded as a loss mechanism, which reduces the number of photons emitted from the sample and is considered by the radiative recombination efficiency η_{rad}.

Highly excited carriers ("hot carriers") lose their excessive energy by scattering processes with the lattice very quickly until the conduction band minimum (electrons) and the valence band maximum (holes) is reached, respectively. As the carrier lifetime is large compared to this relaxation time (typically picoseconds [Par07]), the recombination can be assumed to take place only from states at the edges of or within the band-gap. In general, the energy of the photon equals the difference in the energies of the initial and the final state of the electron. It may be reduced by the excitation energy of optical phonons (phonon replica). The typical transitions observed in luminescence measurements are displayed in Figure 2.8 and abbreviated according to the common nomenclature. In general, different recombination paths can be identified by the dependence of the peak energy and the peak intensity on the injection density and/or the sample temperature. A detailed discussion of these relations can be found in [Pan75; Sch92; Reg04].
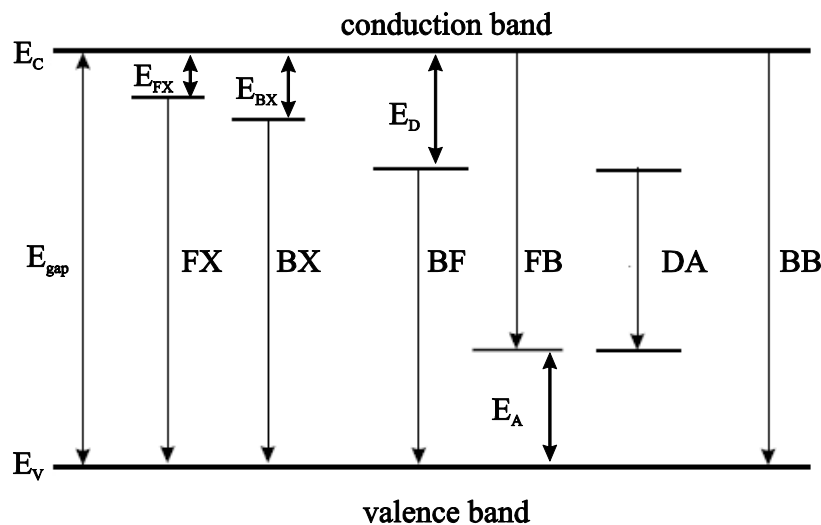
Figure 2.8: Optical transitions occurring in semiconductor materials. The full band-gap energy is detected when recombination occurs directly from the conduction band (E_C) to the valence band (E_V). The energy is lowered by the binding energies E_{FX} and E_{BX} of free and bound excitonic stated (for excitonic transitions) and E_D and E_A of donor and acceptor defect levels (for defect related transitions), respectively.

The highest observable energy ($E_{BB} = E_{gap}$) originates from the transitions directly between the conduction and the valence band (band-to-band transition, BB). The energy of exciton related transitions (free exciton, FE, and bound excitons, BE) is lowered for the exciton binding energies E_{FX} and E_{BX} due to the coulomb interaction between electron and hole. Excitons are mostly observed in low temperature experiments only, but as they are not found in Cu-poor Cu(In,Ga)Se$_2$ (as shown in Section 2.3.4) they are not discussed here in detail.

Additionally, carriers localized at defects can be involved in the recombination processes. Then, the photon energy is reduced for the donor and/or acceptor energies E_D and E_A, respectively. While the bound-to-free (BF) and free-to-bound (FB) transitions involve both localized and free carriers, the donor-acceptor-pair transition (DA) occurs from defect level to defect level. The energy of the DA-transition is given by

$$E_{DA} = E_{gap} - E_D - E_A + \frac{e^2}{\varepsilon_0 \varepsilon \, r}.$$
(2.19)

The last term in Eq. (2.19) accounts for the coulomb interaction of the charged donor-acceptor-pair after the emission. It is determined by the relative permittivity ε of the sample and the distance of the donor-acceptor-pair r taking part in the recombination process. Since the average distance of the donor-acceptor-pair decreases with increasing injection density Δn, a blue-shift of a few meV per decade of increasing excitation power is usually observed [Pan75]. If the thermal energy in the sample approaches the shallower defect energy, the recombination preferably occurs via FB- or BF- rather than via DA-transitions. If the temperature is increased even further, also the deeper defect can be ionized and BB-recombination is observed.

The standard model for the donor-acceptor-pair transition is only valid for low donor and acceptor concentrations $N_{D/A}$, i.e. for $N_{D/A} \ll a_{e,h}^{-3}$ [Shk84] with $a_{e,h}$ being the Bohr-radius of the respective impurity. In case of high defect concentration and also a high compensation ratio (for a p-type semiconductor) $K = N_D/N_A$ an alternative description has been developed by Shklovskii et al. [Shk84]. The model describes the influence of a concentration of ionized defects N_I which is considerably higher than the one of free charge carriers p. This leads to an incomplete screening of localized charges and, thus, to average potential fluctuations with an amplitude γ of

$$\gamma = \frac{e^2}{4\pi\varepsilon_0\varepsilon} \frac{N_I^{2/3}}{p^{1/3}}.$$
(2.20)

This model has been shown to be valid for Cu-poor Cu(In,Ga)Se$_2$ [Dir98; Bau01; Sie04b; Sie06]; the influence of the compensation on the optical transitions is discussed in detail in Section 2.3.4.

2.3.4 Review on luminescence of Cu(In,Ga)Se$_2$

The luminescence of the quaternary system Cu(In,Ga)Se$_2$ and the two corresponding ternary compounds CuInSe$_2$ and CuGaSe$_2$ has been subject to numerous studies. PL-, CL- and EL-investigations lead to a comprehensive picture of the luminescence properties and their dependence on temperature, injection density and stoichiometry. As most work was done using PL spectroscopy, the defect model of Cu(In,Ga)Se$_2$ is described along with these data. Although most of the data were obtained on single-crystalline samples, the results can also be applied to polycrystalline thin-films [Reg05]. A detailed survey of the literature can be found in [Reg04].

The luminescence spectra of the ternaries CuInSe$_2$ and CuGaSe$_2$ are displayed in Figure 2.9 (a) and (b), respectively, as they were measured with PL at low temperatures ($T \leq 10\ K$) [Bau01; Sie04b] for different Cu-contents. For both materials, a strong, but similar influence of the Cu-content on the spectrum is observed, and therefore the following description holds for both systems. In Cu-rich samples and near-stoichiometric samples (if Cu/III is larger than approximately 0.95), several emissions are observed: Excitonic luminescence is measured next to two DA-transitions and their phonon replica. The so-called DA1-emission is found to be 20 - $40\ meV$ higher than the DA2-emission, which relatively increases in intensity with increasing Cu-content. In Cu-poor samples (if Cu/III is smaller than approximately 0.95), only one broad DA-transition can be observed, which exhibits an asymmetric broadening towards lower energies and a continuous red-shift with decreasing Cu-content. This transition can be presumed to be due to the same defects as the DA1-emission in stoichiometric material, because the energy converges towards E_{DA1} for Cu/III approaching 0.95.

Measurements on Cu-rich samples have also been performed for the quaternary system Cu(In$_{1-x}$Ga$_x$)Se$_2$ for different values of x. These data show a continuous shift of the respective emission energies with the band-gap [Yos00; Reg05]. A similar signature is obtained for the whole range of stoichiometry except of a broadening of the peaks for the mixed phases, which is explained by a higher degree of disorder [Reg05]. From the luminescence energies, a defect model has been developed for the whole range of x = 0…1, which is shown in Figure 2.10(a) [Reg05]. In this model, the two DA-transitions are attributed to one shallow donor level ($E_D = 10\ meV$ for CuInSe$_2$) and two deeper acceptor levels ($E_{A1} = 40\ meV$, $E_{A2} = 60\ meV$ for CuInSe$_2$), which exhibit slightly increasing defect energies for higher band-gap materials. The model is in agreement with data obtained from different groups as shown in Figure 2.10(b) [Zot97; Dir98; Yos00; Bau01; Sie04b; Reg05], where the DA1-transition energy E_{DA1} at low temperature (4-10 K) is plotted as a function of the GGI. In addition, the band-gap is shown as a function of GGI (solid line) (featuring a bowing factor of -0.167 eV [Alo02] and band-gaps of $E_{gap,CISe} = 1.045\ eV$ and $E_{gap,CGSe} = 1.720\ eV$ [Reg05]). From

this band-gap, the DA1-transition energy is calculated as a function of GGI using the defect model shown in Figure 2.10(a). A similar relation between E_{DA1} and the GGI is presented in [Rom03b].
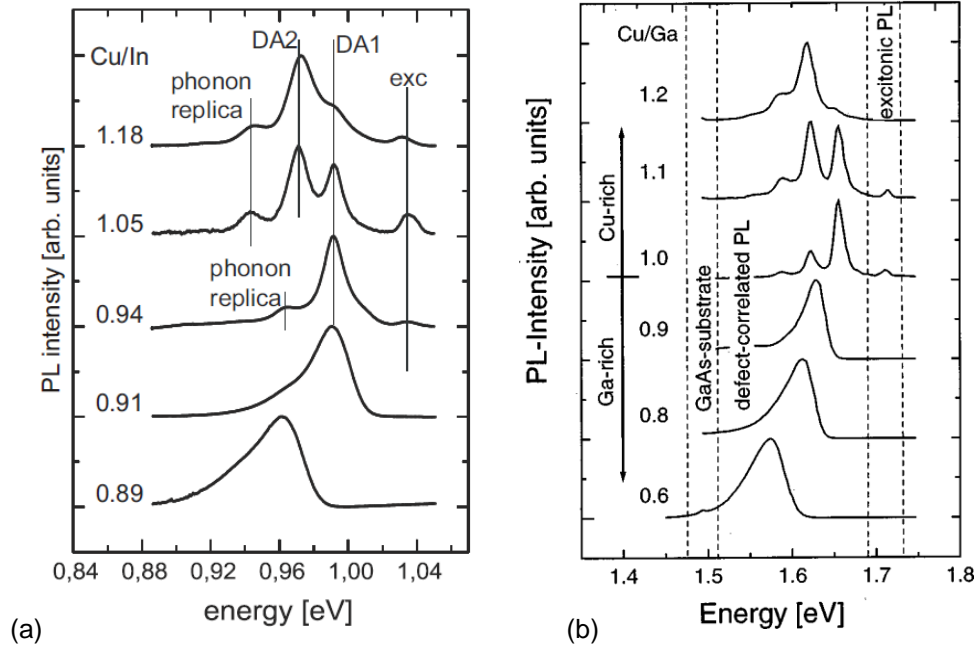

Figure 2.9: **Photoluminescence spectra of CuInSe$_2$ (a) and CuGaSe$_2$ (b) epitaxial layers at a temperature of 10 K for varying Cu/III-ratios taken from [Sie04b] and [Bau01], respectively.**

As discussed above, the defect energies used in the model were obtained from analyzing Cu-rich or near-stoichiometric samples. The DA1-transition of Cu-poor Cu(In,Ga)Se$_2$ is commonly interpreted to be increasingly affected by strong potential fluctuations (see Section 2.3.3) with decreasing Cu-content due to the strong self-compensation of the material [Zot97; Dir98; Bau01; Sie04b]. This type of transition shall hereafter be referred to as quasi-donor-acceptor-pair transitions qDAP as also done in literature [Bau01; Rom03a]. As a result of these fluctuations, the following unusual features can be observed for qDAP-transitions:

- a red-shift of the emission with increasing compensation ratio K [Dir98; Bau01; Sie04b; Sie06] (see Figure 2.9), which can be approximated by $\Delta E = 2\,\gamma_{opt}$ [Bau01; Rom03b; Sie06];
- a particularly strong blue-shift of the emission of more than 10 *meV decade*$^{-1}$ with increasing injection density Δn [Dir98; Bau01; Sie04b];
- for very high injection densities, the injected charge carriers screen the local charges and the emission energy E_{qDAP} reaches a saturation value $E_{qDAP,sat} = E_{DA1}$ [Dir98];
- a broadening of the peak which is especially strong towards low energies (asymmetric) with decreasing Cu-content [Dir98; Bau01; Sie04b; Sie06].

The amplitude of the fluctuations which is active in optical transitions γ_{opt} is smaller than the total amplitude γ because the typical tunneling length occurring in the optical transitions is small when compared to the screening length [Dir98; Sie06]. Since the red-shift of the emission energy is not

due to changes in the band-gap, the correlation of both quantities is not straight forward for Cu-poor Cu(In,Ga)Se$_2$: either the measurement has to be performed at saturation for high injection densities ($E_{qDAP,sat}$) or γ_{opt} must be known. The latter quantity can be obtained from fitting the low energy slope of the peak [Sie06].
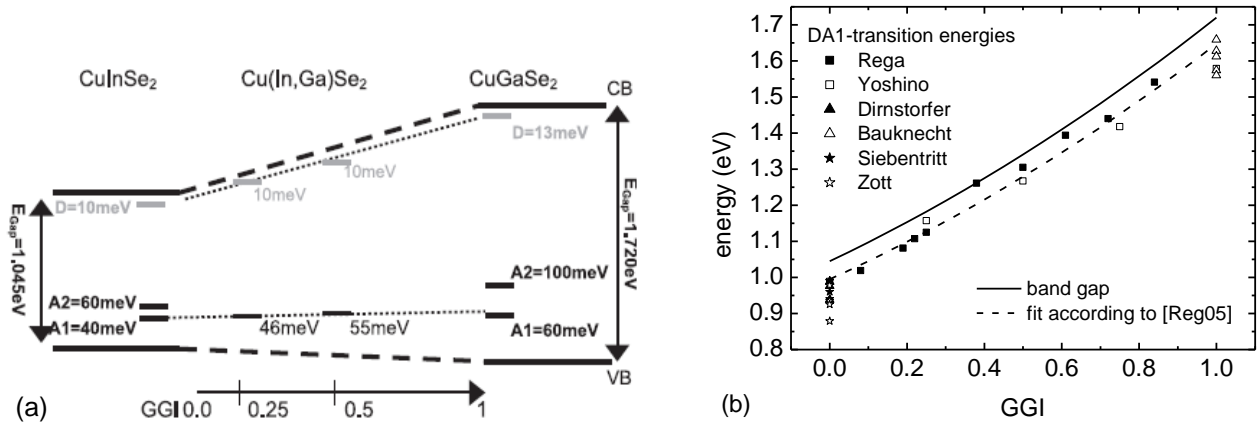

Figure 2.10: (a) Defect model for Cu-rich and stoichiometric Cu(In,Ga)Se$_2$ with varying Ga-content taken from [Reg05]. (b) DA1-transition energy as a function of the Ga-content as measured by different authors. Additionally, the band-gap energy and the DA1-transition energy are plotted according to [Reg05].

In recent years, also CL and EL of Cu(In,Ga)Se$_2$ thin-films have been studied. EL is performed on full devices and therefore the luminescence is observed at or close to real electrical working conditions of the solar cell (forward voltage regime). It is also preferentially used for large scale applications due to the simple experimental setup. CL offers the highest lateral resolution of all luminescence techniques and depth-dependent measurements can be performed by a variation of the electron energy. These two advantages are used to investigate changes in luminescence properties in the sub-μm range, such as the influence of grain boundaries [Rom03a; Ott04; Han06; Het06; Abo09], differences between individual grains [Rom03a; Sie05b; Het06] and surface related phenomena [Str02; Roc03; Rom03b; Reg04].

In most luminescence investigations, samples with a constant stoichiometry [GGI, S/(S+Se)] have been used – or at least the samples were assumed to be homogeneous. Since band-gap graded material is used for solar cell fabrication, the luminescence of this type of samples is of especially high interest. According to my knowledge, there is no study so far, which systematically investigates the luminescence properties of Ga-graded or S-graded Cu(In,Ga)(S,Se)$_2$. But some observations in luminescence spectra have been discussed regarding the variation of the band-gap:

Wagner et al. [Wag98] observed different peaks in PL spectra in Cu(In,Ga)Se$_2$ thin-films grown by RTP-selenization of metallic precursors. These peaks were ascribed to regions with different band-gaps (due to varying Ga-content), which was confirmed by photoluminescence excitation spectroscopy (PLE). Also Rega et al. [Reg05] describe an increase of the Ga-content with increasing

depth in their epitaxial samples. As the generation takes place in the first 100 *nm* only, they discuss the surface stoichiometry measured by energy dispersive X-ray spectroscopy (EDS) to solely determine the detected peak energy. Additional depth resolved CL spectra in [Reg04] show that the local CL peak energy does not correspond to the local Ga-content within these epitaxial films.

An increase of the saturated peak energies $E_{qDAP,sat}$ with the distance from the free surface is observed in [Rom03b]. This does not fit to a double band-gap grading induced by the Ga-profile (corresponding profiles can be found in [Yan02; Ram03a]). Laterally resolved spectra on a sample thinned from the backside for transmission electron microscopy (TEM) reveal an additional peak at 1.15 *eV* to appear in regions with a high density of dislocations, which relatively decreases in intensity with increasing beam-current. The appearance of this peak is interpreted to be due to the existence of a sub-interface, which acts as a barrier for the transport of injected carriers [Rom03b].

Although these observations already point towards an influence of the grading, many recent studies on the luminescence of Cu(In,Ga)(S,Se)$_2$ thin-films do not give any information on the shape of the grading present in the layer [Con09; Ish09; Slo10; Paw11; Zac11]. However, the presence of some kind of Ga-grading must be presumed because the samples were all deposited by the three-stage process. Mostly, the emission energies are interpreted in relation to an average band-gap calculated from the integral Ga-content. This assumption may lead to incorrect interpretations of the luminescence signal. Therefore, the luminescence of Ga-graded Cu(In,Ga)Se$_2$ is systematically investigated in this work.

2.3.5 Detection of the luminescence signal

The CL intensity is detected as a function of position and energy in CL imaging and spectroscopy, respectively. Therefore, it is essential to exclude all effects leading to a spatial or spectral dependence of the CL intensity in the detection process. All steps, which have to be taken from the radiative recombination process (emission of the photon) to the final luminescence signal, are described below with a focus on the spatial and spectral dependence. All these processes can be summarized in the external quantum efficiency of the CL measurement EQE_{CL}. A detailed description can be found in [Yac90].

Re-absorption: After emission, photons may be re-absorbed in the sample on their way out. The re-absorption depends on the energy-dependent absorption coefficient $\alpha(E_v)$. The absorption can directly influence the spectral distribution of photons detected with the system and therefore it must be considered very carefully in spectroscopy. As the absorption coefficient α of a direct semiconductor strongly increases when the energy reaches the band-gap energy, especially near-edge emission such as band-to-band and exciton correlated emissions suffer from re-absorption.

Defect-related emission with energies approximately 50 meV below the band-gap exhibit larger absorption length [e.g. of about 1 μm in Cu(In,Ga)Se$_2$] – thus, absorption may be negligible here. The re-absorption in band-gap graded material is a special case, because the absorption coefficient additionally depends on depth: $\alpha = \alpha(E_\nu, z)$. In the samples investigated in this thesis, the band-gap decreases with increasing depth and so the re-absorption of emissions from deeper regions is reduced when compared to homogeneous material. But if the band-gap increases with depth in the excitation region, re-absorption will strongly reduce the intensity of the high-energy emissions.

In cross-section measurements, the band-gap is assumed to be constant with depth for every single spot. Thus, the re-absorption can be neglected for DA-transitions.

Reflection and total reflection: In addition to absorption, the reflection and the total reflection at the sample surface or another interface causes to a strong reduction of the EQE_{CL}. Photons are emitted isotropically and all those emitted at an angle larger than $\theta_C = \arcsin(n_2/n_1)$ inclined from the vertical axis are totally reflected internally according to Snell's law (n_i denote the refractive indices of the two materials at the interface). For the special case of the interface Cu(In,Ga)Se$_2$/vacuum with $n_1 \approx 3$ and $n_2 = 1$, the EQE_{CL} reduces by about a factor of $f_R = 50$ [Yac90]. But as the refractive index can be assumed to be only weakly dependent on energy around the band-gap energy [Kaw98], the influence on the spectra can be neglected in most cases. Spatial variations of f_R can occur due to surface roughness.

Collection efficiency: Additional corrections have to be applied due to the overall collection efficiency of the collection system. This includes the reflectivity of the mirrors, the transmission of the lenses and the monochromator and the quantum efficiency of the detector. This collection efficiency can be measured with a calibrated light-source and used for the correction of all spectra.

In all measurements, the focal optic of the collection system (mirror or lens) limits the region of investigation to the area of the focal point, which can have a diameter below 100 μm. Any optical maladjustment influences the spatial distribution of the collection efficiency, and thus, the luminescence intensity.
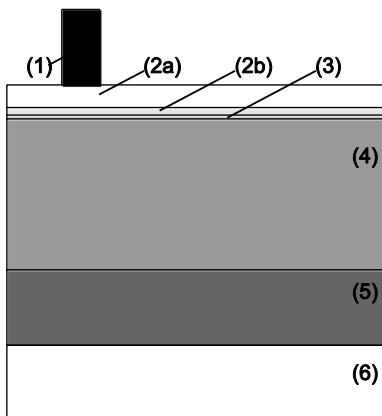
3 Experimental and analytical methods

3.1 Experimental methods

This section gives an overview on all experimental methods applied in this work for solar cell preparation (Sections 3.1.1 + 3.1.4), ion implantation (Section 3.1.2) and annealing (Section 3.1.3)

3.1.1 Absorber deposition

All solar cells used in this work were prepared according to the layer structure shown in Figure 3.1: The Cu(In,Ga)Se$_2$ absorber is deposited by multi-stage co-evaporation (based on the three-stage process) on molybdenum-coated soda-lime glass substrate as described in [Kau09]. The sputtered Mo back-contact as well as the absorber layer were deposited at the "Helmholtz-Zentrum für Materialien und Energie Berlin" (HZB). The absorber deposition process at the HZB is well-established and solar cells made from these absorbers yield international-standard high efficiencies up to 18% [Kau09; Cab10]. The process starts by evaporating a sequence of InSe- and GaSe-precursor layers, which are subsequently transformed into Cu(In,Ga)Se$_2$ in the second phase supplying only Cu and Se. At the end of this phase, the material turns Cu-rich (Cu/III > 1), which has been found to be essential for large grain sizes [Rau99b]. In the third stage, the final Cu-poor stoichiometry is obtained by evaporating In, Ga and Se, only. The whole process is controlled by laser-light scattering (LLS) [Kau09]. The integral stoichiometry is measured by means of X-ray fluorescence spectroscopy (XRF) to Cu/III $\approx 0.8 - 0.9$ and GGI ≈ 0.3.

function	material	thickness (nm)
(1) front grid	Mo/Cu/Mo or Ni/Al	1 or 2 μm
(2) window	(a) ZnO:Al	300 nm
	(b) i-ZnO	≈ 75 nm
(3) buffer	CdS	≈ 50 nm
(4) absorber	Cu(In,Ga)Se$_2$	$1.7 - 2$ μm
(5) back-contact	Mo	1 μm
(6) substrate	soda lime glass	2 mm

Figure 3.1: Typical stack of a Cu(In,Ga)Se$_2$ solar cell; layer properties as used in this study are listed in the table on the right.

In Chapter 6, the absorber deposition at increased substrate temperature is investigated on a glass substrate specially developed by Schott AG Mainz. This substrate features a sodium content comparable to standard glass and an optimum match of the coefficient of thermal expansion (CTE),

but allows to employ substrate temperatures up to 700°C [Win09]. The high-temperature absorbers deposited at a nominal substrate temperature of 610°C are compared with the absorbers from the standard process at 530°C, both types of absorbers being deposited on this new glass substrate. All other parameters such as the elemental fluxes or evaporation times remained nominally unchanged. The integral stoichiometry is not influenced according to XRF.

3.1.2 Ion implantation and SRIM calculations

Ion implantations were performed at the linear ion accelerator ROMEO at the "Institut für Festkörperphysik" (IFK) in Jena. All elements were separated into pure isotopes by mass separation. Acceleration voltages from 20 to 350 kV can be used. The implantation currents were in the order of 1 - 3 μA. Different parameter sets (isotopes, energy, fluence) were used throughout this work as listed in Table 3.1. As a standard, an ion energy of 20 keV is used; deviations from this standard are mentioned in the text. The fluence is adjusted to yield a maximum concentration of 10^{21} cm^{-3} (around 2 at.%) for all implantations. Implanting a 25 x 25 mm^2-sized sample needed about 5 - 30 min for the applied fluences.

The ion ranges listed in Table 3.1 and the profiles shown in Section 4.3 were calculated using the Monte-Carlo code **S**topping and **R**ange of **I**ons in **M**atter (SRIM) [Zie03]. The SRIM calculations were performed for $Cu(In_{0.7}Ga_{0.3})Se_2$ with a density of 5.75 g cm^{-3} and the default binding energies suggested by SRIM (displacement energy 25 eV, lattice binding energy 3 eV, surface binding energy 3.52, 2.49, 2.14 and 2.82 eV for Cu, In, Ga and Se, respectively).

The implantation damage can also be estimated by SRIM calculations, which yields a maximum number of displacements of $N_{disp,max} = \max_z N_{disp}(z)$ between 10 and 50 per incident ion and nanometer for the above isotopes and energies. This corresponds to a number of displacements per atom n_{dpa} [Nas06] of 10 - 60 dpa for the above fluences. A number of 1 dpa means that, on the average, every atom in the respective volume has been displaced once from its original lattice site.

isotope	energy (keV)	range (nm)	fluence (10^{15} cm^{-2})	used in Section
^{114}Cd/^{132}Xe	20	11.3/10.6	1.4	4.4+4.5 (*j-V*, *EQE*, *C-V*, CL)
^{64}Zn	20	13.8	2.0	4.4+4.5 (*j-V*, *EQE*, *C-V*)
^{24}Mg	20	29.3	5.0	4.4+4.5 (*j-V*, *EQE*, *C-V*)
^{114}Cd/^{132}Xe	20	11.3/10.6	4.2	4.4.3 (*EQE*)
^{114}Cd	100	34.8	4.0	4.3 (SIMS)
^{64}Zn	65	34.2	5.0	4.3 (SIMS)
^{24}Mg	24	33.9	6.0	4.3 (SIMS)

Table 3.1: List of parameter sets (isotope, ion energy, fluence) used for ion implantation in this work. The range is given as calculated by SRIM.

3.1.3   Thermal annealing

The thermal annealing of the implantation defects is performed in an RTP furnace, which allows to apply different atmospheres and pressures. Annealing was performed either in ambient air at 1 *bar*, in Ar-gas at slight overpressure (1.2 *bar*) or in a rough vacuum (around 3 *mbar*). Different annealing procedures were applied in this work as listed in Table 3.2: The annealing was performed either after completion of the solar cell (procedure A) or directly after implantation (procedures B and C). Annealing temperatures are range from 50 to 500°C; dwell times of either 30 *min* or 0 *min* were used. Procedures B1 (300°C/30 *min*) and C1 (350°C/0 *min*) have been established as a standard for defect annealing in this work. The heating rate was kept constant at 100 $K\ min^{-1}$, no active cooling was applied. The annealing without dwell time is applied for a reduction of dopant diffusion as discussed in detail in Section 4.3. For the given heating and cooling profiles and assuming an activation energy of 1 *eV* for diffusion (see Section 2.2.3), the diffusion length can be estimated to be 20 times higher when annealing for t_{ann} = 30 *min* compared to the process without dwell time for temperatures ranging from 300 - 500°C. Thus, an annealing time equivalent of $t_{ann,equi}$ = 1.5 *min* is assumed for a process without dwell time.

procedure	process order position	annealing ambient	dwell time	annealing temperature
A	after completion	air or Ar	30 *min*	50 – 300°C
B	after implantation	Ar or vacuum	30 *min*	300 – 500°C
C	after implantation	Ar or vacuum	0 *min*	350 – 500°C
B1	after implantation	vacuum	30 *min*	300°C
C1	after implantation	vacuum	0 *min*	350°C

Table 3.2: List of parameter sets (position in the solar cell fabrication process, annealing ambient, annealing time and temperature) used for thermal annealing of solar cells and absorber layers in this work.

3.1.4   Front-contact deposition

Solar cells are completed using a CdS buffer layer and a ZnO-bi-layer as window structure at the IFK Jena. The buffer is deposited in a chemical bath (CBD). Therefore, the samples are placed in a bath containing cadmium sulfate ($CdSO_4$, 47 *mg*), ammonium hydroxide (NH_4OH, 30%-solution, 11.5 *ml*), thiourea [$SC(NH_2)_2$, 1.465 *g*, filtered solution] and water (H_2O, 164 *ml*) and put in a water bath pre-heated to a temperature of 65°C. The solution and the bath are stirred by a magnetic stirrer for the whole deposition time of 7.5 *min*.

The i-ZnO/ZnO:Al bi-layer is deposited by RF-magnetron sputtering at a base pressure of $2\ 10^{-7}$ *mbar*. The sputtering parameters are shown in Table 3.3. A metal grid is deposited onto the ZnO:Al-layer by DC-sputtering of a triple layer of Mo/Cu/Mo with an overall thickness of 1 *μm* and

a relative shading A_G of 9%. In the case of buffer-less solar cells (Section 4.5), the CdS-deposition is just omitted in the process order.

The solar cell data shown in Chapter 6.4 were measured on solar cells completely processed at the HZB as described in [Kau09]. The buffer/window structure is comparable, but a Ni/Al-front grid with a thickness of about 2 *μm* is used as a front-contact; the grid shading A_G is about 2.2%. A MgF$_2$ anti-reflective (AR) coating of a thickness of 110 *nm* has been used in some cases. These devices always showed higher efficiencies compared to cells completed at the IFK, which is presumed to be due to a higher degree of optimization of the window-structure to the absorbers and/or a degradation of the absorbers during the transport to Jena.

layer	process gas	pressure (10^{-3} *mbar*)	gas flow (*sccm*)	power (*W*)	time (*min*)	thickness (*nm*)
i-ZnO	Ar+O$_2$	2.8	6	150	13	63
ZnO:Al	Ar	2.0	6	200	22	290

Table 3.3: List of the parameter set used for deposition of the ZnO-window double-layer.

3.2 Methods of characterization

All characterization methods used in this work shall be mentioned and shortly described. Details are given only in case of the external quantum efficiency in Section 3.2.2, since non-standard interpretations are applied. Extra details will also be given on the set-up used for cathodoluminescence analysis in Section 3.2.9 as it has been extensively used in this work.

3.2.1 Current density-voltage characteristics – *j-V*

Current density-voltage measurements (***j-V***) under standard AM1.5 illumination are the technique most commonly used in solar cell characterization. A comprehensive overview of the application of the technique on thin-film solar cells is given in [Heg04].

Typical dark and light *j-V*-curves of a solar cell are shown in Figure 3.2(a). The four basic parameters (short-circuit current density j_{sc}, open-circuit voltage V_{oc}, fill factor *FF* and solar cell efficiency η) can easily be determined from the point of zero voltage (j_{sc}), the point of zero net current (V_{oc}) and the maximum power point MPP (*FF* and η). Detailed analysis is performed on the basis of the one-diode model [Sze81]

$$j(V) = j_0 \left\{ exp\left[\frac{q}{n_{id} k_B T}(V - R_s j) \right] - 1 \right\} + \frac{V - R_s j}{R_{sh}} + j_{Ph} . \qquad (3.1)$$

Therein, the *j-V*-characteristics are solely defined by the diode quality (saturation current j_0, diode ideality factor n_{id}), parasitic resistances (series resistance R_s, shunt resistance R_{sh}) and the generated

photocurrent j_{Ph}. The diode ideality factor n_{id} has been introduced to account for the recombination both in the SCR ($n_{id} = 2$) and the neutral region ($n_{id} = 1$) [Sah57]; only values between 1 and 2 can be explained in terms of this model. Evaluation of this implicit equation is performed using a Mathematica code based on graphical methods (Plot B from [Wer88]).

Each sample finalized at IFK Jena has a size of 25 x 25 mm^2 and consists of eight separate solar cells with a size of 5 x 10 mm^2. Samples fully processed at the HZB have a final size of 50 x 50 mm^2 and consist of 15 cells with sizes of 5 x 10 mm^2 and 10 x 10 mm^2. Mean values and standard deviations as shown in Chapter 6 and in the Appendix are calculated by statistical evaluation of all the cells from one sample. The relative error of the measurement is mainly determined by the inaccuracy of the determination of the cell area to about 6%.
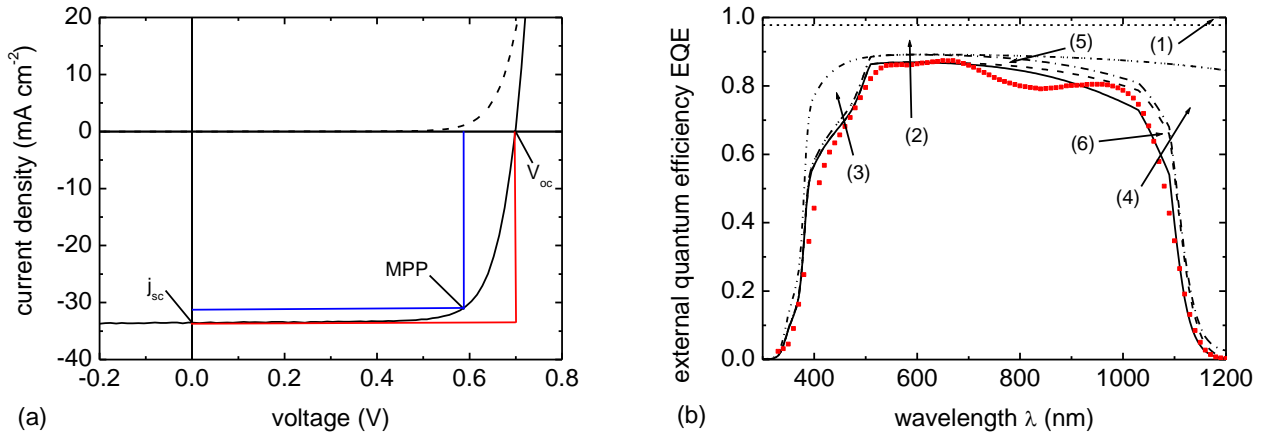

Figure 3.2: (a) Light and dark *j-V*-characteristics of a Cu(In,Ga)Se$_2$ solar cell showing the characteristic points: short-circuit current density *j$_{sc}$*, open-circuit voltage *V*$_{oc}$ and the maximum power point MPP. (b) Typical *EQE* spectrum of a Cu(In,Ga)Se$_2$ cell (red squares) and the current losses divided into the different loss mechanisms.

3.2.2   External quantum efficiency – *EQE*

The **E**xternal **Q**uantum **E**fficiency (*EQE*) of a solar cell is defined as the number of electrons collected from the device divided by the number of incident photons. It is measured as a function of the incident photon wavelength. An *EQE* lower than one indicates losses occurring in the device. A typical *EQE* spectrum (red squares) is displayed in Figure 3.2(b); all black lines are simulations based on optical and electrical experimental data (see below for details). The losses can be resolved into the common optical and electrical loss mechanisms (1 - 6):

(1) wavelength-independent losses due to absorption in the front-grid A_G (shading)

(2) losses due to optical reflection at the whole stack R_{stack} and UV- and (free-carrier) IR-absorption in the ZnO window layers A_{ZnO}

(3) losses due to absorption in the CdS buffer (400 – 550 nm)

(4) losses due to transmission of light through the absorber (thickness d_{abs}) at high wavelengths

(5) wavelength-independent losses due to the recombination at the buffer-absorber interface

(6) losses in the red due to incomplete collection from deeper regions of the cell

An approximation of the losses in short-circuit current density due to these mechanisms is given in [Heg04]. The experimental data additionally show optical interferences in the ZnO window, which were neglected in the simulations. The different losses can be brought together to obtain an analytical expression for *EQE* simulations as discussed in the literature [Liu94; Heg04; Heg07; Häd11]. The *EQE* can be described as a product of the optical-loss term L_{opt} and the internal quantum efficiency *IQE*. If complete collection in the SCR is assumed, the *EQE* is obtained to

$$EQE = L_{opt} \cdot H \cdot \left[1 - \frac{1}{\alpha_{CIGSe} L_{diff} + 1} \exp(-\alpha_{CIGSe} w_{SCR}) \right] \qquad (3.2)$$

[Heg04; Häd11] using the interface recombination factor *H* and the optical-loss term

$$L_{opt} = (1 - A_G) \cdot (1 - R_{stack}) \cdot (1 - A_{ZnO}) \cdot \exp(-\alpha_{CdS} d_{CdS})$$
$$\cdot [1 - \exp(-\alpha_{CIGSe} d_{abs})] . \qquad (3.3)$$

In this work, the optical reflections from the whole stack are approximated by the reflections measured on a ZnO-layer on glass leading to the substitution $T_{ZnO} \approx (1 - R_{stack}) (1 - A_{ZnO})$. These equations have already been used for the simulations in Figure 3.2(b). The ZnO-transmission and the CdS-absorption have been measured by transmission and reflection measurements using an integrating sphere (data shown in the Appendix, Figure A1); the Cu(In,Ga)Se$_2$ absorption coefficient is calculated according to [Nag07]. Furthermore, a grid-shading A_G of 2.2%, an absorber thickness d_{abs} of 2 μm, an interface recombination factor *H* of 0.96, an SCR-width w_{SCR} of 500 *nm* and a diffusion length L_{diff} of 1 *μm* have been assumed in Figure 3.2(b).

If the optical-loss term L_{opt} is presumed to be constant for all processed devices, the *EQE* is solely determined by the SCR-width, the diffusion length and the interface recombination. While the latter leads to a wavelength-independent scaling of the *EQE*, a decrease of the other two leads to lower collection at long wavelengths. Thus, their influence can hardly be separated in the *EQE*. However, the diffusion length can be determined independently if the SCR-width is taken from *C-V*-measurements (see Section 3.2.3). If a strong dependence of the capacitance on illumination conditions is observed in *C-V*-analysis, then, no reliable data can be given for the SCR-width. In this case, the combined collection length $L_{coll} = w_{SCR} + L_{diff}$ is determined from the *EQE* [Kni04].

All *EQE* measurements are performed at zero voltage bias (short-circuit conditions). Ideally, *EQE* measurements should be performed under working condition, which is under AM1.5 bias-

illumination. In our set-up, a halogen lamp is used for bias-illumination and adjusted to 11% AM1.5-equivalent. Some cells involving annealing and/or ion implantation show very strong apparent quantum efficiency (AQE) effects [Eis98; Eng99; Kön02; Glo04] in the CdS- and/or i-ZnO-absorption region. A very short description of the observed effects is given in the Figure A3 to Figure A5 in the Appendix. For these cells, an optical filter was used, which restricts the bias illumination to the wavelengths absorbed in the window- and buffer-layers (blue-light bias, see Figure A2 for filter transmissions).

3.2.3 Capacitance-voltage-profiling – *C-V*

The measurement of the capacitance C of the p-n-junction as a function of the applied voltage bias V yields information on e.g. the SCR-width w_{SCR} and the depth profile of electrically active defects. Other applications and details of the method are described in [Blo92]. In this work, the *C-V*-technique is used for two purposes only:

(1) To determine the room-temperature SCR-width w_{SCR} at short-circuit conditions ($0\ V$). Before measurement, the cell was kept in the dark until the capacitance stabilized (usually a few minutes). These values were then used in the *EQE*-simulations as described in Section 3.2.2.

(2) To determine doping profiles from the *C-V*-characteristics of ion implanted devices and to compare those to the profiles of the corresponding reference samples. The depth scale may be incorrect if a high concentration of traps with high emission rates is present in the layer [Blo92] – therefore, the axis is cautiously labeled as "apparent depth".

3.2.4 Electron microscopy

Electron microscopy is a standard technique for high-resolution imaging. It has been used in two different modes in this work [Scanning Electron Microscopy (SEM) and Transmission Electron Microscopy (TEM)] in order to investigate the grain structure of the absorber. Details about these two methods can be found e.g. in [Gol03] and [Wil09], respectively.

TEM-Cross-section samples are prepared by lamella preparation with a Focused Ion Beam (FIB) FEI-Helios NanoLab 600i. The FIB-lamella preparation is described in detail in [Wan09].

3.2.5 Energy-dispersive X-ray spectroscopy and X-ray fluorescence – EDS/XRF

Both the **E**nergy-**D**ispersive X-ray **S**pectroscopy and the **X-R**ay **F**luorescence are used to non-destructively determine the elemental composition of a specimen. They are based on characteristic X-ray emission, which is excited by either an electron beam (EDS) or high-energy X-rays (XRF).

While EDS was applied for high-resolution composition analysis (band-gap grading of the absorber), XRF was used to measure the integral stoichiometry of the absorbers. Details of these methods can be found in [Gol03] and [Bec06], respectively.

3.2.6 Secondary ion mass spectroscopy – SIMS

Secondary **I**on **M**ass **S**pectroscopy (SIMS) is a destructive technique to measure high-resolution elemental depth profiles. The depth resolution is mainly determined by surface roughness and preferential sputtering effects. In this study, the depth was scaled by sputtering through the whole Cu(In,Ga)Se$_2$ layer which had a well-known thickness. Absolute concentrations were normalized to the maximum concentration obtained from the implantation depth profiles calculated by SRIM. Details of the method are described in [Ben87]. All SIMS measurements shown in this thesis were performed at Schott AG Mainz.

3.2.7 X-ray diffraction – XRD

X-**R**ay **D**iffraction (XRD) is a non-destructive technique to analyze the crystallographic structure of a specimen. The polycrystalline thin-films are analyzed in the Bragg-Brentano configuration. The method is e.g. described in [War90].

3.2.8 Photoluminescence – PL

Details of the luminescence techniques have been described in Section 2.3.3. In **P**hoto**l**uminescence (PL), the generation of carriers occurs by photogeneration with a laser. For all PL measurements discussed in this work, an unfocused beam (makro-PL) of an Ar-laser pumped Ti-sapphire laser is used at constant wave operation with the following standard parameters: a photon energy of $E_v = 1.7 \ eV$, a temperature of $T = 10 \ K$, a beam power of $P = 20 \ mW$ and an illuminated area of about $A_{ill} = 1 \ mm^{2.}$ The luminescence signal is detected using a liquid-nitrogen cooled germanium-diode; all spectra are corrected using a system reference.

3.2.9 Cathodoluminescence – CL

Cathodo**l**uminescence (CL) imaging and spectroscopy uses a well-focused electron beam for carrier generation and is commonly performed in a Secondary Electron Microscope (SEM). All measurements shown in this thesis were measured using the set-up schematically displayed in Figure 3.3. A JEOL SEM 6490 with an LaB$_6$-cathode was used, supplying an electron beam with constant electron energies E_e between 0.1 and 30 keV and beam currents I_b from approximately 1 pA to 100 nA. A Gatan monoCL3-system is attached to this SEM for CL analysis. The sample is placed

on liquid-He cooled cryo-stage, which can be used for temperature-dependent measurements from 6 to 300 K.

The luminescence light is collected by a mirror of paraboloidic shape, which can be inserted into the chamber above the sample. The distance d from the sample surface to the lower edge of the mirror has to be about 0.6 mm in order to reach the focal point of the mirror; thus, it collects the light from almost the entire hemisphere. The electron beam reaches the sample through a hole in the mirror, which has a diameter of 1 mm. The diameter of the focal point is about 30 μm when carefully adjusted; an area of 400 μm^2 is scanned in order to obtain spectra averaged over a larger number of grains.

For CL spectroscopy, a monochromator is used. For the IR-range, two diffraction gratings each with 600 lines/mm are available, which are blazed to a wavelength of 800 nm (NIR-grating) and 1600 nm (IR-grating), respectively. While the former shows a rather constant efficiency over the whole range of interest (700 - 1400 nm, 0.89 - 1.77 eV), the latter can be used for wavelengths ranging from 1000 to 1700 nm (0.73 - 1.24 eV) only. As broad peaks are measured in Cu-poor Cu(In,Ga)Se$_2$, a spectral resolution of 5 nm was used for most spectra. For polychromatic imaging, the mirrors termed A and B in Figure 3.3 can be taken out of the beam path. All spectra and images were detected with an (In,Ga)As-photomultiplier Hamamatsu R5509-73, which was cooled to -80°C (193 K) with liquid nitrogen. For the IR-grating, a system reference has been measured and was used to correct all spectra as described in Section 2.3.5. This system reference is not available for the NIR-grating, but no large influence is expected as the references of both grating and detector are rather constant in the whole region of interest.
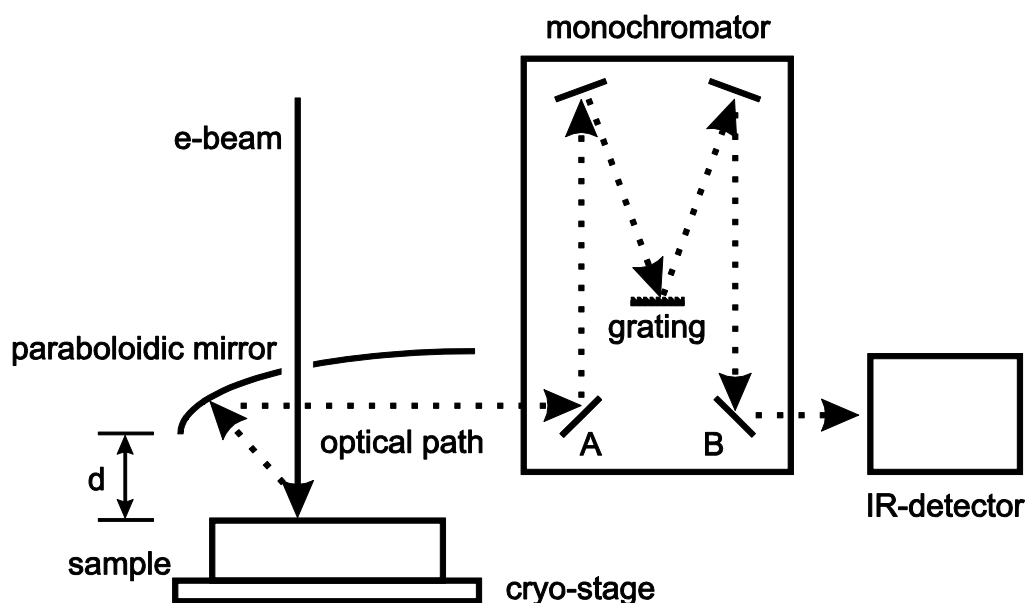

Figure 3.3: Experimental set-up of the Gatan MonoCL3 used for all CL measurements in this work. The optical path is sketched by the dotted line; all parts of the instrument are explained in the text in further detail.

An electron energy of $E_e = 10\,keV$, a beam current of $I_b = 250\,pA$ and a measured sample temperature of $8\,K$ were chosen as standard parameters. The effective sample temperature is presumed to be somewhat higher (10 - 20 K) due to the thermal insulation of the glass substrate and the power input of the incident electron beam. Deviations from these parameters are mentioned in the text.

4   Interface modification by ion implantation

In the following chapter, the influence of low-energy heavy-ion implantation on the absorber material properties and the performance of solar cells made from these absorbers is described. The influence of interface inversion on the device performance is investigated by SCAPS simulations (Section 4.1). For an effective near-interface extrinsic doping, the damage caused by ion implantation needs to be annealed by a thermal treatment. Thus, an annealing procedure is needed that

- does not degrade the solar cell performance (Section 4.2),
- does not induce a significant diffusion of the dopants (Section 4.3) and
- leads to sufficient annealing of the implantation damage (Section 4.4).

Finally, buffer-free Cu(In,Ga)Se$_2$ solar cells are produced and investigated as an alternative to conventional Cu(In,Ga)Se$_2$ solar cells with CdS buffer (Section 4.5). The results described in this chapter have partially been presented at the Spring Conference 2010 of the European Material Research Society (EMRS) in Strasbourg and published in [Haa11b].

4.1   Numerical simulation of interface effects

The influence of the Fermi-level position at the interface on the solar cell performance is demonstrated in this section by numerical simulations with SCAPS 1-D 2.9 (**S**olar Cell **Cap**acitance **S**imulator) [Bur00; Bur08]. Five different structures were simulated for this purpose, which are displayed in Figure 4.1 (A) to (E). All parameters of the window, buffer and absorber layer were adapted from the base case in the dissertation of Markus Gloeckler [Glo05a] (the full parameter set is given in the Appendix Table A1. The defect properties used for structures C, D and E are summarized in Figure 4.1(F). Figure 4.2 (a) and (b) displays the *j-V*-characteristics and *EQE* spectra, respectively, as obtained by the simulation of all five structures.

Structure A represents the standard solar cell set-up with a CdS buffer layer and yields an open-circuit voltage of 640 *mV* and efficiencies above 17%. Comparison of the simulation with experimental results [open black squares in Figure 4.2(a)] shows the performance to be very similar to today's high-efficiency devices. For structure B, the CdS buffer layer is simply deleted from the layer stack in the simulation, which leads to a higher short-circuit current density of the cell due to reduced absorption losses (see also the corresponding *EQE* spectra). In the experiment, solar cells without CdS buffer suffer from severe losses in open-circuit voltage and fill factor [see open green

squares in Figure 4.2(a)], which is clearly not the case in this simulation. This discrepancy can be solved if interface recombination is taken into account, which is believed to be significant in this case, whereas it is commonly assumed to be negligible in the reference case [Glo05a]. The interface recombination is included in the simulation for structure C by introducing an interface containing charged mid-gap defects between the absorber and the window layer. The concentration and the carrier capture cross sections of both donor and acceptors were adjusted in order to model the *j-V*-characteristics of a real buffer-less solar cell.

If an n-type surface layer is introduced in the $Cu(In,Ga)Se_2$ absorber as done in structure (D) (shallow donor concentration $N_D = 10^{18} \, cm^{-3}$, $d_{inv} = 25 \, nm$), the high-quality diode behavior can be recovered including efficiencies close to the reference case. This high-quality performance is obtained despite a high concentration of interface defects and, thus, can be presumed to be rather independent of the window-absorber interface quality.

(F)	interface	inverted layer	inv. layer+ defects
N_D/N_A	$0/0 \, cm^{-3}$	$10^{18}/0 \, cm^{-3}$	$10^{18}/0 \, cm^{-3}$
N_{DG}	$2.5 \, 10^{12} \, cm^{-2}$	$0 \, cm^{-3}$	$10^{18} \, cm^{-3}$
N_{AG}	$2.5 \, 10^{12} \, cm^{-2}$	$0 \, cm^{-3}$	$10^{18} \, cm^{-3}$
$E_{DG,AG}$	mid-gap	-	mid-gap
w_G (eV)	0.1	-	0.1
σ_e (cm²)	$5 \, 10^{-13}/1 \, 10^{-15}$	-	$5 \, 10^{-13}/1 \, 10^{-15}$
σ_h (cm²)	$1 \, 10^{-15}/5 \, 10^{-13}$	-	$1 \, 10^{-15}/5 \, 10^{-13}$
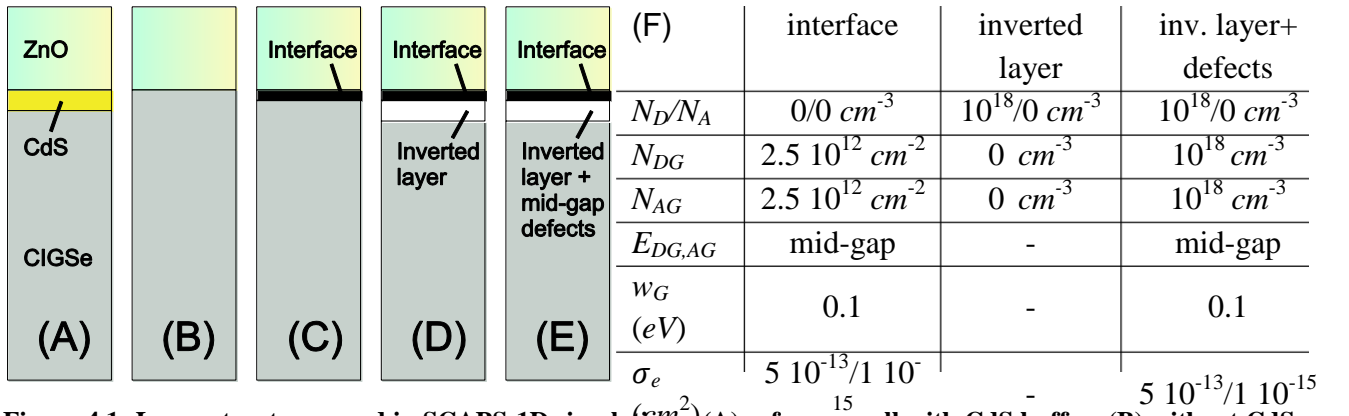
Figure 4.1: Layer structures used in SCAPS-1D simulations: (A) reference cell with CdS buffer; (B) without CdS buffer layer; (C) without CdS buffer and with mid-gap interface defects; (D) without CdS buffer, with interface defects and with an n-type surface layer in the absorber with a thickness of 25 *nm*; (E) without CdS buffer, with interface defects and with an 25 *nm* type-inverted surface layer in the absorber with shallow donors as well as mid-gap donor and acceptor levels. All parameters of the reference structures were adapted from [Glo05a] and are listed in the Appendix in Table A1.
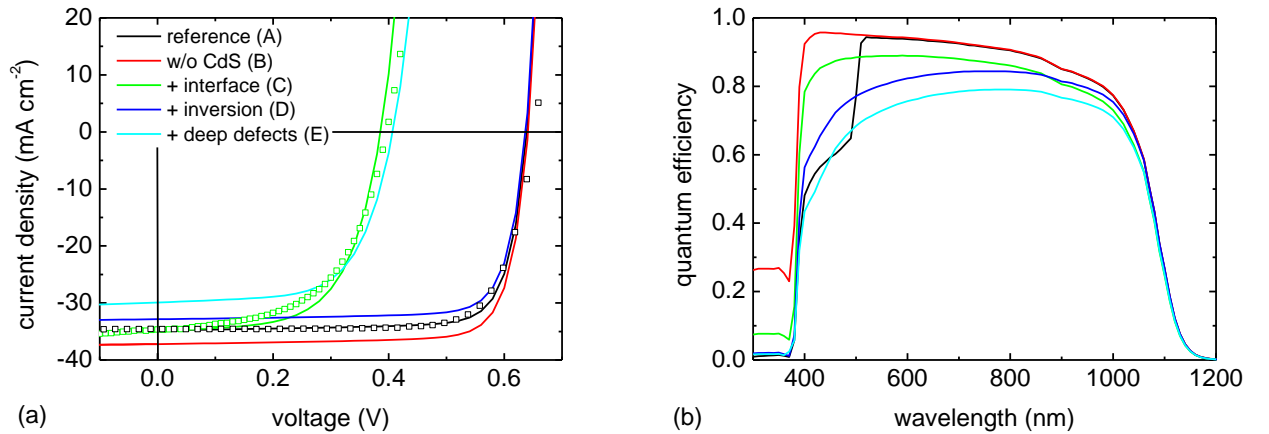

Figure 4.2: *j-V*-characteristics (b) and quantum efficiency (c) obtained from simulation of the layer structures shown in Figure 4.1. Additionally, experimental *j-V*-curves are shown for solar cells made with (black squares) and without (green squares) CdS buffer.

This recovery of the open-circuit voltage can be understood when looking at the band-structure near the interface, which is plotted for all four cases in Figure 4.3 at $0\,V$ bias and under AM1.5 illumination. In Figure 4.3(A), the band-structure is shown for structure A featuring an inverted interface: The electron quasi-Fermi E_{Fn} level is close to the conduction band E_C at the interface. While this inversion is maintained without the CdS layer in the simulation of structure B, the Fermi-level is pinned mid-gap in case C due to the high density of interface defects. When introducing an n-type surface layer (structure D), the p-n-junction is moved away from the hetero-interface (buried junction) and the inverted surface is reestablished. Hence, if the inversion of the surface layer is successful, then the solar cell properties should be more or less the same with and without CdS buffer layer and allow the buffer layer to be totally omitted.

The efficiency of devices with an inverted surface layer can also be shown by simulation to remain above 16% even for a negative conduction band off-set ("cliff") between ZnO and Cu(In,Ga)Se$_2$ up to $\Delta E_C = $ -0.5 eV. This high-level performance is found despite the reduced recombination barrier at the interface as long as it remains inverted (in contradiction to [Kle01]). It is concluded that the inverted surface layer is an essential part of the device functionality and leads to a very stable interface configuration.

In this work, the inversion shall be introduced by ion implantation; hence, a large density of implantation-induced deep defects may be present in the implanted layer, if no appropriate annealing procedure is applied. Therefore, the influence of a high density of charged mid-gap defect levels in the inverted layer on the solar cell performance is studied by simulation of structure E. A strong decrease in V_{oc} is observed due to the presence of the defects [see Figure 4.2(a)], despite of an inverted interface [see Figure 4.3(E)]. It is concluded that an effective annealing procedure is needed in order to minimize the concentration of deep-level defects.
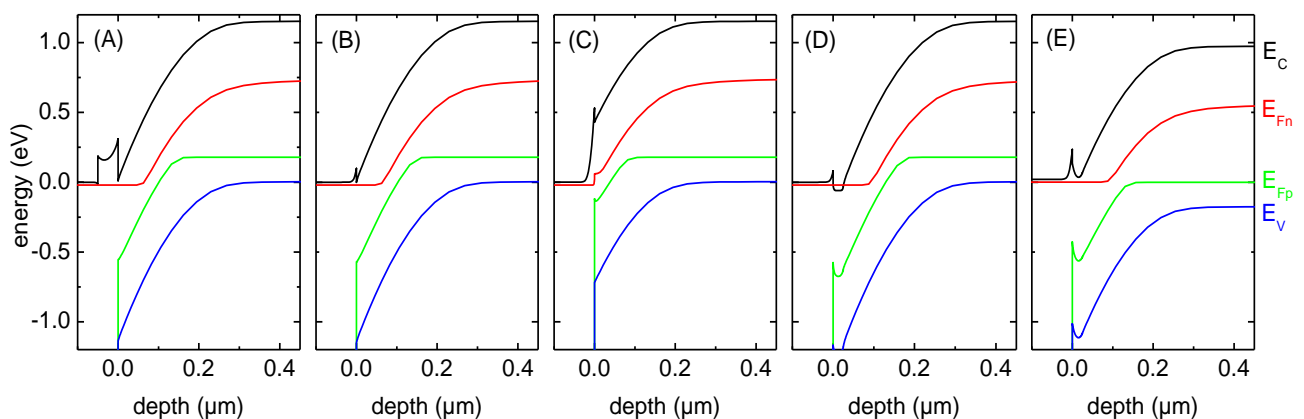

Figure 4.3: Band-diagrams simulated using SCAPS-1D for the five layer stacks displayed in Figure 4.1 showing the conduction (E_C) and valence (E_V) band as well as electron (E_{Fn}) and hole (E_{Fp}) quasi-Fermi levels for standard AM1.5 illumination.

The slight losses in short-circuit current density observed with an n-type surface layer (structure D) are shown to occur in the short wavelength region only in the simulated *EQE* spectra in Figure 4.2(b). A similar shape of *EQE* is found for the defect-rich inverted layer (structure E). These losses are due to the absorption in the type-inverted layer, as discussed in Section 4.4.3, and can be minimized by reducing the n-type layer thickness.

In conclusion, the interface inversion is found to play an essential role in Cu(In,Ga)Se$_2$ solar cell functionality. The introduction of an n-type surface layer may be a possibility to obtain high-efficiency buffer-free solar cells.

4.2 Thermal treatment of Cu(In,Ga)Se$_2$ solar cells without implantation

An annealing procedure is needed in order to minimize the implantation damage as repeatedly pointed out by the simulations in the previous section. If the annealed material is meant to be used for subsequent solar cell production, the preservation of the solar cell performance upon the annealing process must be guaranteed. This is examined in this section by applying different annealing procedures to unimplanted absorbers. The annealing step may be introduced into the solar cell fabrication process either after solar cell completion (Section 4.2.1) or directly after implantation (Section 4.2.2). Repeated annealing after completion offers the advantage of directly investigating the effect of annealing on the solar cell properties on the very same sample.

4.2.1 Annealing after window deposition

The annealing of fully processed solar cells is a well known procedure, which does not necessarily lead to degradation; at times it even leads to an improved performance of the cells [Nou86; Cah89; Rau99a]. It is commonly performed for up to one hour at atmospheric pressure at around 200°C in air. Annealing at higher temperatures is observed to lead to degradation, which has been explained by the diffusion of Zn and/or Cd from the window and/or buffer into the absorber [Kij08]. Similar experiments were carried out in this work in order to determine the maximum temperature applicable using post-window-deposition annealing to the present Cu(In,Ga)Se$_2$ absorbers.

Figure 4.4 displays the *j-V*-characteristics of solar cells made from a reference absorber, which was successively annealed for 30 *min* in air at temperatures ranging from 200 to 300°C (procedure A, see Table 3.2). While the performance is stable after annealing at 200°C, degradation is observed for higher temperatures. As a similar effect is also observed when annealing the samples under Ar-atmosphere, it is concluded to be due to temperature activated processes (such as diffusion) and not to oxygenation effects. These results imply that the annealing after window-deposition is limited to temperatures of about 200°C in agreement with previous results [Nou86; Cah89; Rau99a].
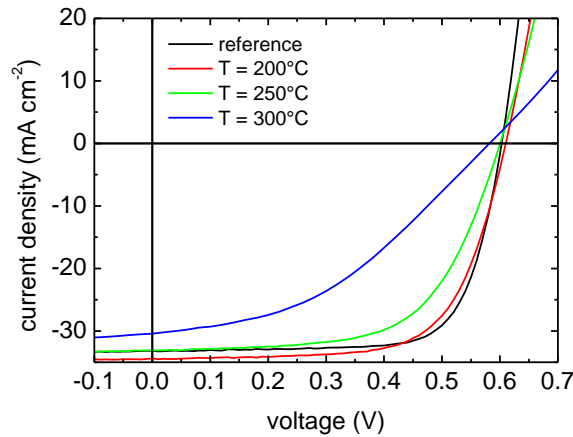
Figure 4.4: *j-V*-**characteristics of the same solar cell with CdS buffer before (reference) and after successive annealing according to procedure A.**

4.2.2 Annealing before window deposition

Alternatively, the annealing process can also be performed directly after implantation to avoid the diffusion of window-layer constituents. In Figure 4.5 (a) and (b), the *j-V*-characteristics of solar cells are displayed, which were made from reference absorbers annealed in Ar-atmosphere at different temperature ranging from 300 to 500°C for 30 *min* (procedure B, see Table 3.2) and without dwell time (0 *min*, procedure C), respectively. For the longer annealing procedure, the performance can be maintained at the temperature of 300°C, but it gets worse at higher values. For the shorter annealing times, the cell stays on the reference level even up to 400°C.

The loss in short-circuit current density occurring at high annealing temperature is furthermore investigated by *EQE* measurements shown in Figure 4.6 (a) and (b) and *C-V*-analysis (not shown). It appears that the carrier collection is successively reduced at longer wavelength with increasing temperature. This is found to be due to reduction of the SCR-width (from 500 to 200 *nm* obtained from *C-V*-analysis) and diffusion length (from 700 to 200 *nm* obtained from *EQE* simulations).
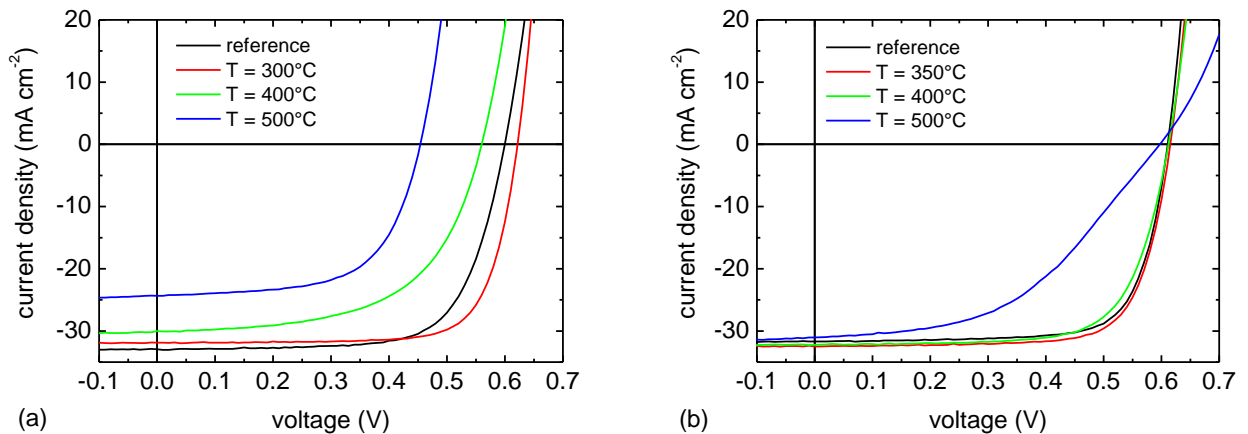
Figure 4.5: *j-V*-**characteristics of solar cells with CdS buffer made from absorber without annealing (reference) and annealed in Ar atmosphere at different temperatures according to procedure B and C in (a) and (b), respectively.**
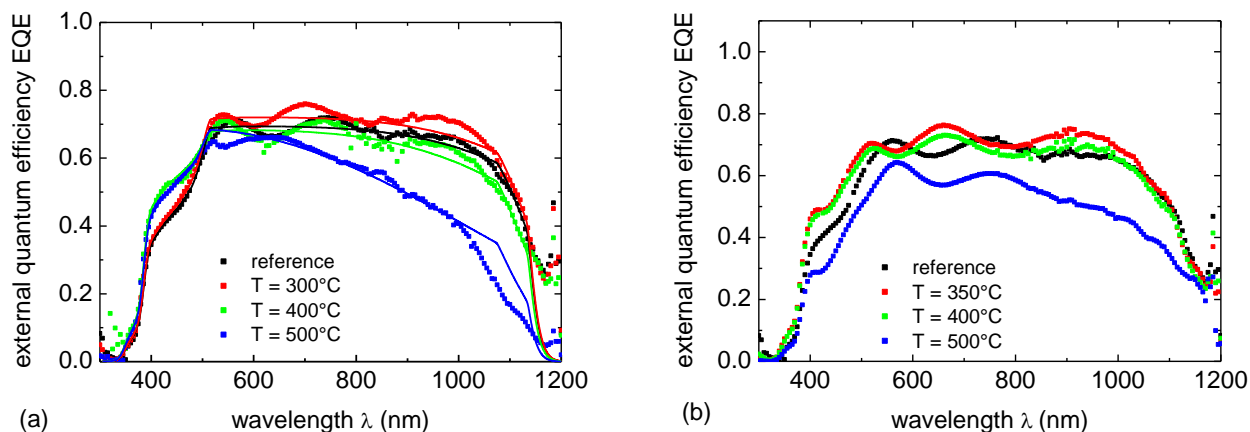
Figure 4.6: *EQE* **spectra of solar cells made with CdS buffer from absorber without annealing (reference) and annealed in Ar atmosphere at different temperatures according to procedure B and C in (a) and (b), respectively. The solid lines in part (a) of this figure represent the result of the *EQE* modeling.**

Comparable experiments have been performed for annealing in low-vacuum ($\approx 3\ mbar$) at these temperatures and dwell times. The vacuum process is found to be more stable and to allow for even higher annealing temperatures (efficiencies above 10% after annealing the absorbers for 30 min at 500°C) – therefore it is chosen as a standard for investigating the defect annealing in Section 4.4.

In summary, the annealing of the absorber is demonstrated to be compatible with the fabrication of high-efficiency solar cells for temperatures up to 400°C when applied before window-deposition. These temperatures are presumed to be suitable for an effective reduction of the damage and the electrical activation of the dopants (see Section 2.2.3).

4.3 Diffusion of the dopants

For an efficient near-surface doping, the dopants need to be kept localized at the surface. The implantation depth can easily be defined by choosing the appropriate ion energy, but the diffusion of the dopants during subsequent annealing may be critical for temperatures above 200°C as discussed in Section 2.2.3. Therefore, the elemental depth profiles of the implanted ions shall be investigated using SIMS. All SIMS measurements have been performed at Schott AG Mainz in collaboration with Dr. W. Mannstadt. The depth resolution of the SIMS measurements was determined to about 11 nm by fitting an error function to the onset of the Cu(In,Ga)Se$_2$ layer elements. The group-II-elements Cd, Zn and Mg were implanted with an energy of 100, 65, and 24 keV, respectively, in order to lead to SRIM-calculated ion ranges [Zie03] of about 35 nm. This range allows the distribution to be well resolved with the given depth resolution of SIMS (no deconvolution necessary), but simultaneously, diffusion lengths of below 50 nm are still detectable. Since the Cd signal is found to be very weak in the SIMS measurement, a thin ZnO layer is sputtered on top of

the absorber after implantation in order to reduce surface related artifacts. The annealing was performed in Ar-atmosphere for 30 *min* at the respective temperatures.
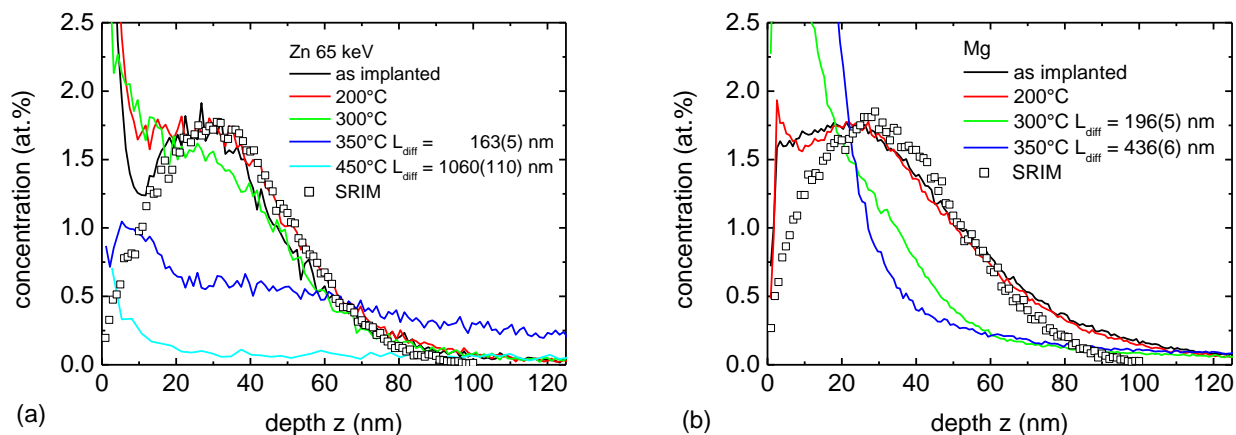

Figure 4.7: Depth profiles of the implanted ions measured with SIMS for Zn- (a) and Mg- (b) implantation and compared with the SRIM-calculated profiles. The SIMS profiles are also shown for implanted absorbers after annealing at different temperatures for 30 *min* in vacuum. The diffusion lengths are determined by an exponential fit to the diffusion profiles at larger depth (not shown).

The SIMS profiles are displayed for Zn and Mg in Figure 4.7 (a) and (b), respectively, as measured after different annealing steps and compared to the corresponding SRIM profiles. For both elements, the calculated profiles can be well confirmed by measuring the sample directly after implantation. For Zn-implantation, the profile does not change up to an annealing temperature of 300°C, which is the case for Mg only until 200°C. For higher temperatures, the diffusion leads to an increase of the signal deeper in the layer. The measured diffusion lengths correspond to diffusion constants of $(1.4\pm0.2)\ 10^{-13}\ cm^2 s^{-1}$ (Zn, 350°C), $(6.2\pm1.8)\ 10^{-12}\ cm^2 s^{-1}$ (Zn, 450°C), $(2.2\pm0.3)\ 10^{-13}\ cm^2 s^{-1}$ (Mg, 300°C) and $(1.1\pm0.1)\ 10^{-12}\ cm^2 s^{-1}$ (Mg, 350°C) [calculated from Eq. (2.1)]. Diffusion towards the layer surface can be neither excluded nor confirmed due to surface effects of the SIMS measurement. The measured diffusion coefficients for Zn and Mg at high annealing temperatures are plotted in Figure 4.8 as a function of the inverse temperature and compared to literature data if available. An extrapolation to the critical diffusion coefficient (see Section 2.2.3) yields a rough approximation of a critical annealing temperature of $T_{crit,Zn} = 275$°C and $T_{crit,Mg} = 224$°C for an annealing time of 30 *min* (B-annealing, $D_{crit} = 10^{-14}\ cm^2\ s^{-1}$). For an effective annealing time of 1.5 *min* (as approximated for C-annealing, see Section 3.1.3), critical temperatures of $T_{crit,Zn} = 338$°C and $T_{crit,Mg} = 298$°C are obtained ($D_{crit} = 2\ 10^{-13}\ cm^2\ s^{-1}$).

Comparable SIMS profiles for Cd implantation are shown in Figure 4.9(a), which clearly suffer from a higher noise level. Again, the profile of the as-implanted sample agrees with the simulated profile and diffusion is not visible up to 300°C. The diffusion obviously increases at 350°C leading to a complete disappearance of the signal – thus, not diffusion coefficients can be determined for Cd. In case of Cd, the chosen energy is clearly different from the one used for solar cell fabrication

in the Sections 4.4 and 4.5 (20 *keV*); therefore, a second temperature series was performed for this lower ion energy and the same maximum Cd concentration and is shown in Figure 4.9(b). The SIMS profiles appears to be considerably broader when compared to the SRIM profile, which can be explained when considering the influence of the limited resolution of the SIMS measurement as also displayed in the figure (dashed line). In addition, the Cd signal is observed to disappear at 300°C already in contrast to the measurement at the higher ion energy. This trend to a higher diffusion at lower ion energies is confirmed by analyzing the profiles at an intermediate energy (50 *keV*), where a slight reduction of the signal is observed at 300°C (data not shown). This difference may be possibly explained by the increased damage introduced at higher ion energies (quasi amorphous material), which may lead to modified transport mechanisms (see Section 2.2.3). The diffusion coefficients obtained for Cd in [Hie11] are rather close to the data shown for Mg in Figure 4.8.
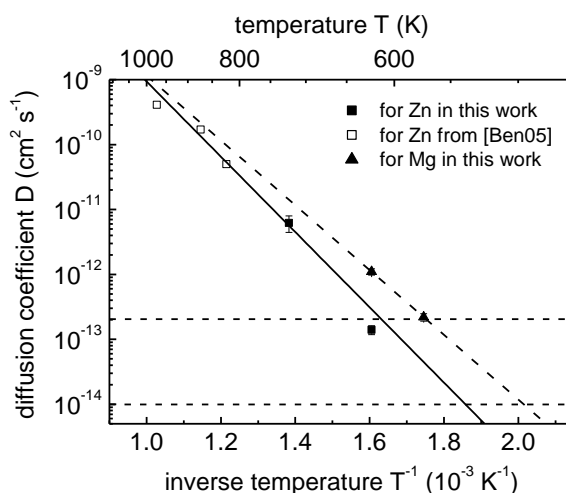
Figure 4.8: Diffusion coefficients of Zn and Mg as obtained from the SIMS profiles in Figure 4.7 and compared to literature data [Ben05]. The measured data are extrapolated to the critical diffusion coefficient D_{crit} (dashed lines) to determine an approximation of a temperature limit for thermal annealing.

The effect of surface sputtering during ion implantation has so far not been considered in this discussion, although it may be substantial. Sputtering leads to a reduction of the effective ion concentration due to removal of implanted atoms from the surface as well as to an effective shift of the profile towards the surface. The SRIM calculations yield sputtering rate of 9.1, 7.0 and 3.3 atoms per ion for the Cd-, Zn- and Mg-implantation, respectively, which corresponds to a relative loss of dopant atoms of a few percent and a shift of the maximum concentration between 1 and 4 *nm* at the given fluence. Experimental evidence for this phenomenon cannot be found in our experiments due to the limited depth resolution of the SIMS measurement.

In summary, the diffusion of Cd and Mg seems to become significant already below 300°C and Zn diffusion increases at 350°C. Thus, it may be a critical issue to avoid dopant diffusion ($L_{diff} < 50$ *nm*) during the annealing of the implantation damage in this temperature ranges.
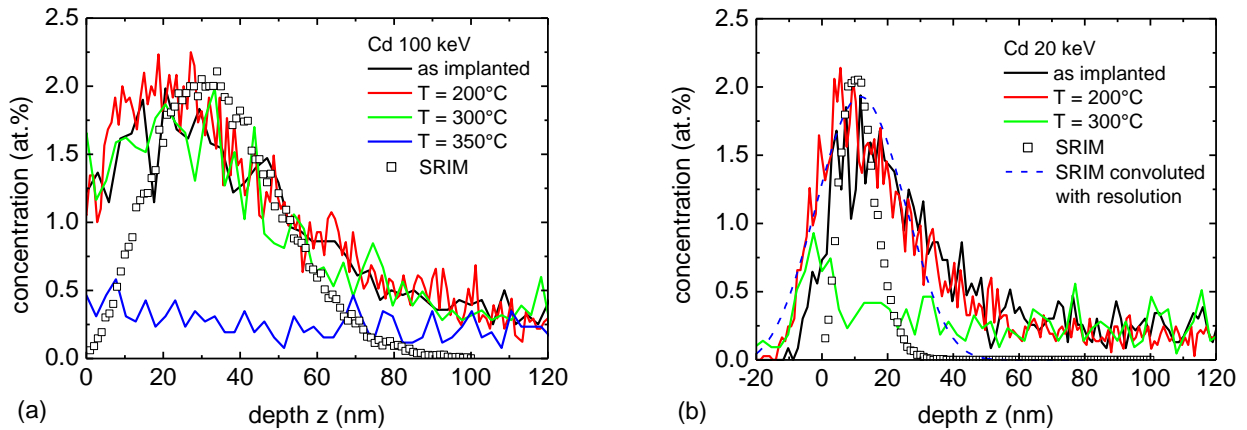
Figure 4.9: Cd depth profiles of the implanted ions measured with SIMS for 100 *keV* (a) and 20 *keV* (b) Cd implantation and compared with the SRIM-calculated profiles. The SIMS profiles are also shown for implanted absorbers after annealing at different temperatures for 30 *min* in vacuum. In part (b) of the figure, the SRIM-profile is also shown after convolution with the SIMS-resolution of 11 *nm* (dashed line).

4.4   Annealing of implantation damage

The annealing procedures described in Section 4.2 shall be applied to study the annealing of the implantation damage by measuring the *j-V*-characteristics (Section 4.4.1) of cells made from implanted absorbers. The recovery of the optical and electrical properties (CL and *C-V*, Section 4.4.2) and the charge carrier collection (*EQE*, Section 4.4.3) is investigated in more detail. For all measurements in this section, cells were prepared with a standard CdS buffer, because the data obtained from implanted samples shall be compared to a well-known reference.

4.4.1   Solar cell performance – *j-V*

The *j-V*-characteristics are plotted in Figure 4.10(a) for solar cells made from Cd implanted absorbers before and after annealing the whole stack (procedure A) and compared to their reference. The implanted sample shows a strong degradation in V_{oc} as well as in j_{sc} when compared to the reference, which can only partly be recovered by the annealing step at 200°C.

The implantation Xe ions is presumed to induce amount and distribution of defects similar to Cd implantation (due to the comparable ion mass), but extrinsic doping effects can be excluded. Therefore, reference implantations were performed with 20 *keV* Xe ions in order to separate the influence of implantation defects (presumably deep defect levels) and Cd doping (shallow levels),. No significant differences between Cd and Xe implantation are detectable in the *j-V* measurements as shown in Figure 4.10(b). This suggests the observed effects to be mainly due to the implantation defects; therefore, higher annealing temperatures are presumed to be necessary.

However, annealing the sample at 250°C after window-deposition unfortunately leads to significant losses in fill-factor as can be seen in Figure 4.10(a). This effect was already observed for the

reference sample (Figure 4.4). Note that the *j-V*-characteristics of cells made from implanted absorbers without any thermal treatment show a high homogeneity over one sample (eight cells), but a low reproducibility between different runs. This can be seen when comparing the curves of the unannealed samples in Figure 4.10 and Figure 4.11.
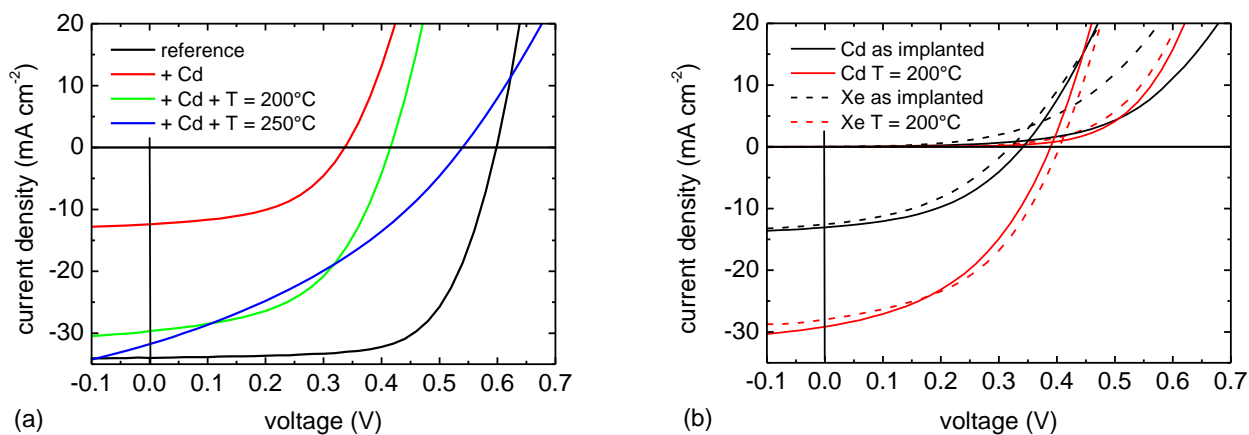

Figure 4.10: (a) *j-V*-characteristics of the same solar cell with CdS buffer made from absorber without implantation (reference) and after Cd-implantation. Repeated annealing is performed according to procedure (A) at increasing temperature. (b) Comparison of the *j-V*-characteristics of solar cells made from Cd- and Xe-implanted absorbers before and after annealing at 200°C.
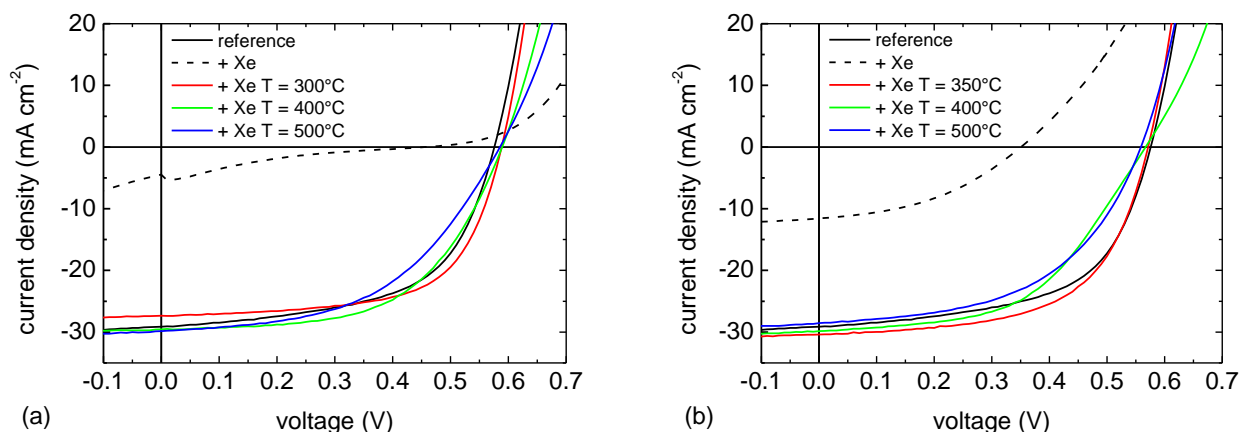
Figure 4.11: *j-V*-characteristics of solar cells with CdS buffer made from Xe-implanted absorbers after annealing in Ar atmosphere at different temperatures according to procedure B and C in (a) and (b), respectively. The curves of the corresponding reference cells are plotted for comparison.

Additional annealing experiments were performed after Xe-implantation using the thermal treatment directly after the implantation step. The *j-V*-characteristics are displayed for different temperatures ranging from 300 to 500°C for procedures B (dwell time of 30 *min*) and C (no dwell time) in Figure 4.11 (a) and (b), respectively. The solar cell efficiency of the corresponding reference cell is very low in this run (around 10%), but it can be found that the reference level can be reached for both annealing times already at the lowest temperatures (300°C/350°C). Therefore, it is concluded that these temperatures are sufficient for the full annealing of the implantation damage – at least, the solar cell performance is not anymore influenced by the damage. Hence, the two processes at the

lowest temperatures are chosen as a standard annealing processes for solar cell fabrication after ion implantation in order to minimize dopant diffusion (see Section 4.3) and material degradation (see Section 4.2.2). The processes are named by B1 and C1 (see Table 3.2) hereafter.

The annealing experiments were repeated for the implantation of the group-II-elements Cd, Zn and Mg in order to compare the results to the Xe-implantation. All implantations were performed at an ion energy of 20 keV, which leads to different implantation depth for each implanted element, and the fluence was adjusted to lead to a constant maximum concentration of 10^{21} cm^{-3} (see Table 3.1). The annealing was performed in vacuum at 300°C/30 min (B1) and 350°C/0 min (C1) for the j-V-curves shown in Figure 4.12 (a) and (b), respectively. The average cell parameters are listed in Table A2 in the Appendix. For both annealing procedures, considerable differences are observed between the three elements.

For Cd implantation, both annealing procedures lead to performances comparable to the reference level with a small but significant loss in short-circuit current density after B1-annealing. After Zn-implantation, the reference level is reached only for the longer annealing time, whereas it cannot be reached in both cases after Mg implantation. This element-specific behavior may originate from the implanted ions being electrically active in the absorber or by differences in diffusion behavior or damage creation and recovery.

It can be concluded at this stage that the recovery of a high-quality solar cell performance after near-surface ion implantation is generally possible, but also element specific behavior is observed
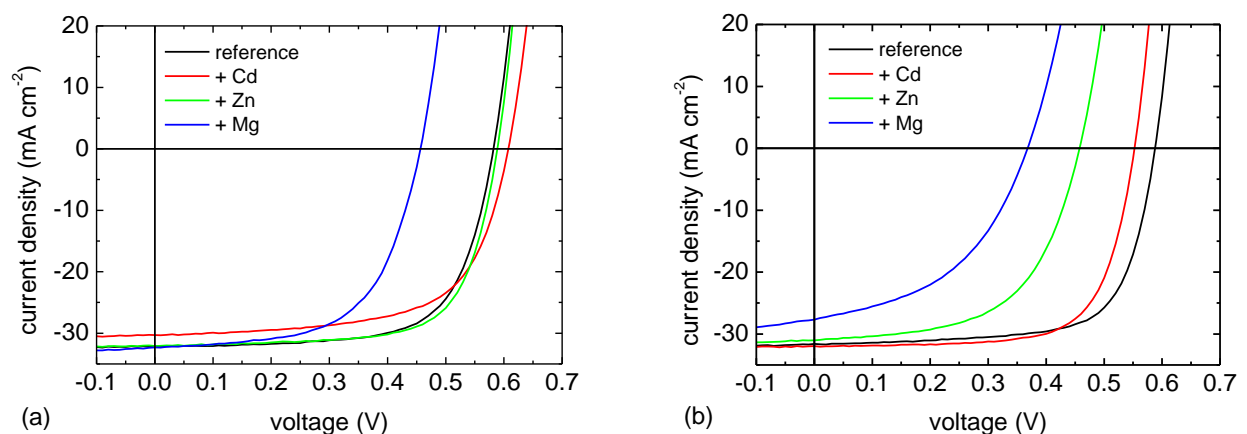

Figure 4.12: j-V-characteristics of solar cells with CdS buffer made from Cd-, Zn- and Mg-implanted absorbers after annealing according to procedure B1 and C1 in (a) and (b), respectively. The curves of the corresponding reference cells are plotted for comparison.

4.4.2 Optical and electrical properties – CL and C-V

Before studying the influence of ion implantation on the CL properties of the Cu(In,Ga)Se$_2$ absorbers, the effect of the thermal annealing on luminescence properties is discussed. Measurements were performed in plan-view geometry (labeled as "front" in Section 5.1) under the

standard conditions defined in Section 3.2.9 for absorbers annealed for 30 *min* in Ar-atmosphere for different annealing temperatures. The spectra are displayed in Figure 4.13(a). A slight red-shift of the maximum of 10 - 20 *meV* occurs upon annealing for all temperatures as also found in [Yu76a; Dir99], which therein has been explained by increased compensation. It is accompanied by a decrease of the CL intensity by up to one order of magnitude. Figure 4.13(b) shows the CL spectra in logarithmic plot after implantation of 20 *keV* Cd-ions with a fluence of $1.4\ 10^{15}\ cm^{-2}$ and subsequent annealing. The peak energy is found to be considerably higher due to a higher minimum band-gap in this sample as will be explained with Chapter 5.
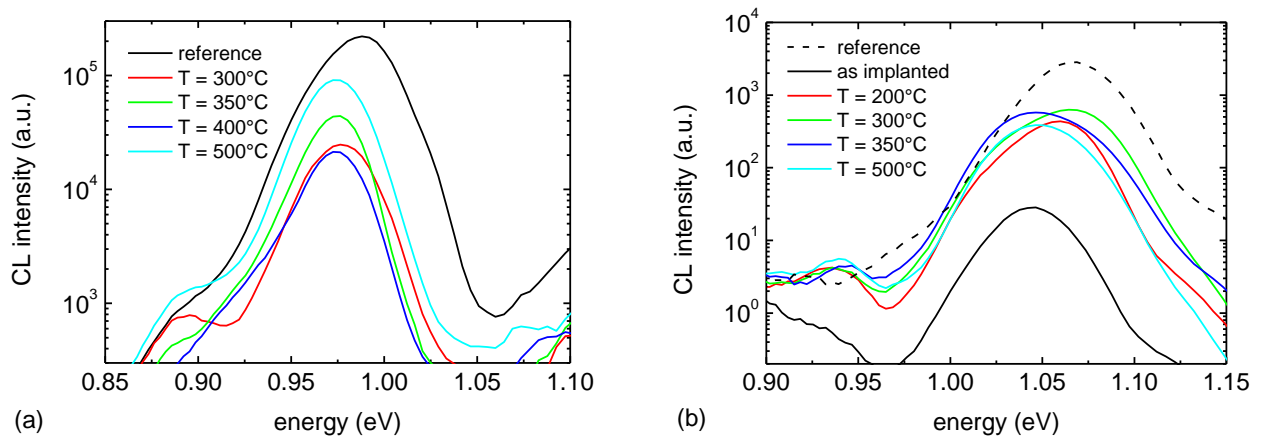
Figure 4.13: (a) CL spectra of absorbers after annealing in Ar-atmosphere at different temperatures according to procedure B and compared to the unannealed reference. (b) CL spectra of Cd-implanted absorbers after annealing in Ar-atmosphere at different temperatures according to procedure B and compared to the unannealed and the unimplanted reference.

Directly after implantation, the CL intensity is strongly reduced by a factor of 100, which is concluded to be due to an increase of the non-radiative recombination rates in the damaged region. After annealing at 200°C, the intensity increases again to a tenth of the reference intensity, which is the same level that is reached after annealing the reference sample without implantation. The intensity remains unchanged for higher temperatures; a red-shift is observed similar to the results shown in Figure 4.13(a). It is not possible to measure distinct doping levels in agreement with others [Mig75; Yu76a] – an effect that can be attributed to the broad peak structure and the effective smearing of the transition energies in the potential fluctuations.

Another standard technique to analyze the electrical activation of the dopants is the measurement of the capacitance-voltage characteristics (*C-V*). It is not the aim of this section to understand the details of the *C-V*-curves but to examine, if the annealing leads to a recovery of the *C-V*-curve of the implanted cells. The standard 20 *keV* Cd-implantation with a fluence of $1.4\ 10^{15}\ cm^{-2}$ were applied. The *C-V*-curves and the corresponding doping profiles of cells made from both reference and implanted absorbers before and after B1- and C1-annealing are shown in Figure 4.14 (a) and (b).
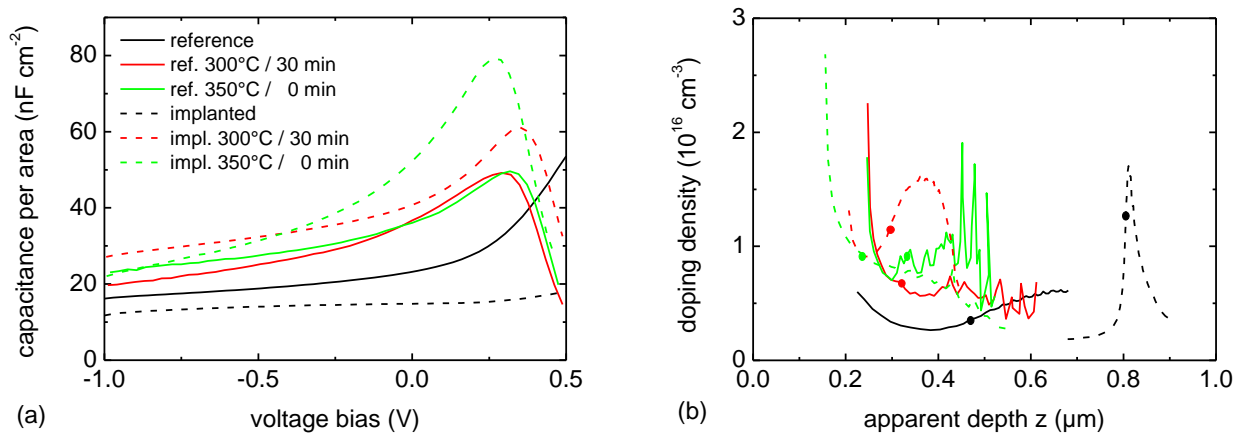
Figure 4.14: (a) *C-V*-characteristics of solar cells with CdS buffer made from unimplanted (reference) and Cd-implanted absorbers before annealing and after annealing according to procedure B1 and C1. **(b)** Doping profiles calculated from the *C-V*-curves shown in part (a) of this figure; the full circles mark the 0 *V*-position.

The black solid line in Figure 4.14(a) represents the capacitance of a reference sample with a standard CdS-buffer, which is continuously increasing with applied voltage bias. The calculated doping profile is displayed in Figure 4.14(b), exhibiting a well-known increase of the doping density under forward as well as reverse bias [Hea04; Rep06; Eis10]. The doping density is measured to approximately $5 \cdot 10^{15}\,cm^{-3}$ with a SCR-width w_{SCR} of around $500\,nm$ at zero bias (marked in the curves by a full spot). A very different behavior can be found directly after ion implantation (black dashed line): The capacitance and the SCR-width w_{SCR} are found to be almost independent of the applied voltage, but the capacitance is smaller than the geometrical capacitance for a fully depleted absorber layer.

The *C-V*-curves of annealed absorbers all show a voltage dependence of the capacitance, but the capacitance is higher compared to the unannealed reference in Figure 4.14(a). The higher capacitance leads to a decreased SCR-width w_{SCR} of around $300\,nm$ and a higher doping level of around $10^{16}\,cm^{-3}$. The decrease of the capacitance in forward voltage is shifted to lower voltages (below 0.5 *V*). No significant differences are detectable anymore between cells from implanted and unimplanted absorbers after annealing.

In conclusion, the irradiation with Cd ions is shown to lead to a reduced radiative recombination efficiency and a voltage-independent capacitance. Both effects can be fully recovered by an optimized annealing procedure directly after implantation. An influence of extrinsic doping is not observed.

4.4.3   Charge carrier collection – *EQE*

The *EQE* spectra are displayed in Figure 4.15(a) for the same cells as the *j-V*-characteristics in Figure 4.10(a). The reference cell shows the normal *EQE* behavior as it is known for Cu(In,Ga)Se$_2$ devices with a CdS buffer layer and does not change significantly upon annealing.

Before annealing, the Cd-implanted device shows a strongly reduced response in the short wavelength region (poor blue-response), whereas the *EQE* at longer wavelengths almost reaches the reference level. This poor blue-response becomes less pronounced upon annealing and is hardly visible after annealing at 250°C. This pronounced poor blue-response was reproducible at slightly higher fluence of 4.2 10^{15} cm^{-2} only, whereas it only occasionally occurred at the standard fluence of 1.4 10^{15} cm^{-2}.
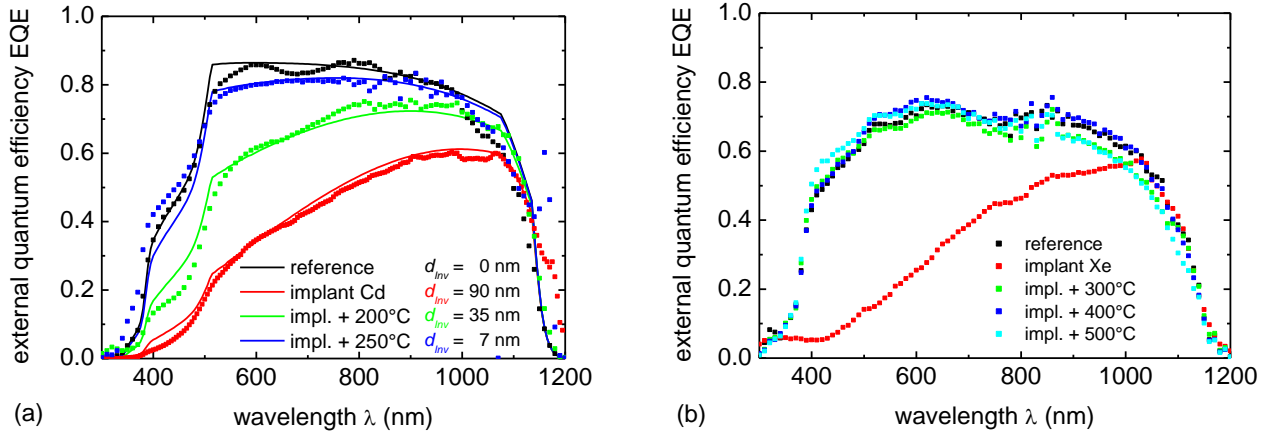
Figure 4.15: (a) *EQE* spectra of the same solar cell with CdS buffer made from Cd-implanted absorbers after successive annealing according to procedure A as compared to the *EQE* of the corresponding reference. (b) *EQE* spectra of the same solar cell with CdS buffer made from Xe-implanted absorbers after annealing according to procedure B as compared to the *EQE* of the corresponding reference.

The shape of the reference *EQE* can be modeled according to Eq. (3.2); optical data are used as described in Section 3.2.2 and an SCR-width of $w_{SCR} = 500$ *nm* is assumed in accordance with the *C-V*-measurements. The interface recombination factor *H* and the diffusion length L_{diff} are adjusted to the *EQE* of the reference cell which yields $H = 1$ and $L_{diff} = 800$ *nm*.

In order to describe the *EQE* of the implanted cells, Eq. (3.2) needs to be expanded by an additional absorption term $(1 - A_{Inv})$ considering for optical absorption in a surface layer in the Cu(In,Ga)Se$_2$ absorber with a thickness d_{Inv}

$$EQE = L_{opt}\,(1 - A_{Inv})\,H\left[1 - \frac{1}{\alpha_{CIGSe}\,L_{diff} + 1}\,exp(-\alpha_{CIGSe}\,w_{SCR})\right] \quad (4.1)$$

with

$$1 - A_{Inv} = exp(-\alpha_{CIGSe}\,d_{inv})\,. \quad (4.2)$$

It is found that the *EQE* of the implanted absorbers can be very well described using this approach by only adjusting the layer thicknesses d_{inv} to 90, 35 and 7 *nm* for the different annealing procedures, respectively. All other data are maintained the same as for the reference cell. This way, the thickness of the inversion layer d_{inv} can be determined. The resolution of the method depends on the quality

and reproducibility of the *EQE* measurement and the amplitude of the interferences from the ZnO layer, but also for excellent data it will not be better than 10 *nm* – therefore, the inverted layer is interpreted to be fully recovered after annealing at 250°C.

It is concluded from this modeling that the surface layer of the absorber has been modified by implantation such that it does not contribute to the current collection, but at the same time allows for collection of minority carriers generated deeper in the cell (no other changes in current collection). This behavior can be explained assuming this layer to be n-type: Minority carriers (holes) generated in an n-type surface layer will recombine (comparable to carriers generated in the CdS buffer) as they are minority carriers at the interface and, thus, subject to increased recombination [Kle01]. The recombination of electrons from p-type regions is not hampered as the surface layer is n-type and, thus, the electrons are majority carriers at the interface. This interpretation is supported by the *EQE* simulations with SCAPS-1D shown in Figure 4.2(b), where the same shape of the *EQE* is obtained for the configuration D with an n-type surface layer. Adjusting the n-type layer thicknesses to the values obtained in Figure 4.15(a), also good quantitative agreement is found in the simulation (not shown).

A similar shape of the *EQE* has been already described in the literature at buried interfaces [Yu76a; Mat87; Sug00; Gri07], but the modeling applied in this work additionally allows to determine the inversion layer thickness. Summing up, a type inversion of the surface layer is presumed to be induced by Cd implantation, which can be recovered by the thermal treatment.

A comparable shape of the *EQE* is observed directly after Xe implantation; an example is shown in Figure 4.15(b). This is in agreement with the similar *j-V*-characteristics [Figure 4.10(b)] and suggests the inversion to be caused by (deep) defects induced by the implantation damage (which may be preferably n-type) and not by (shallow) states from Cd doping. This high concentration of deep defects has been shown by SCAPS simulations in Section 4.1 (structure E) to lead to strongly degraded *j-V*-characteristics even if the inversion of the surface layer was successful and, thus, may possibly explain the poor *j-V*-results observed in Figure 4.10 and Figure 4.11. The blue-response after Xe-implantation is found to be fully recovered when annealing directly after implantation (procedure B), as shown in Figure 4.15(b) [same cells as in Figure 4.11(a)].

Note that the thickness of the inverted layer after implantation of 90 *nm* is by far larger than the implanted depth. As no significant diffusion of Cd ions has been detected by SIMS measurements, the increased thickness is presumed to be due to a migration of implantation induced defects (e.g. interstitials [Nas06]). This migration may be supported by the electric field in the SCR.

The *EQE* spectra have also been measured for the solar cells made from absorbers implanted with Cd, Zn and Mg and are displayed as annealed according to procedure B1 and C1 in Figure 4.16 (a)

and (b), respectively. The slight losses in short-circuit current density observed for Cd after B1-annealing and Zn and Mg after the C1-procedure (see Figure 4.12) can be confirmed by the *EQE* measurements. While the *EQE* of the Zn- and Mg-implanted samples in Figure 4.16(b) show a significant, but wavelength-independent reduced collection (interpreted to be due to increased interface recombination), the Cd implanted sample exhibit a slightly reduced collection at longer wavelengths indicating a reduced collection length [Figure 4.16(a)]. The shape of the spectra does not exhibit a poor blue-response comparable to what has been described above. Thus, the thickness of the n-type surface layer d_{inv} has to be smaller than 20 *nm* if it is present at all.
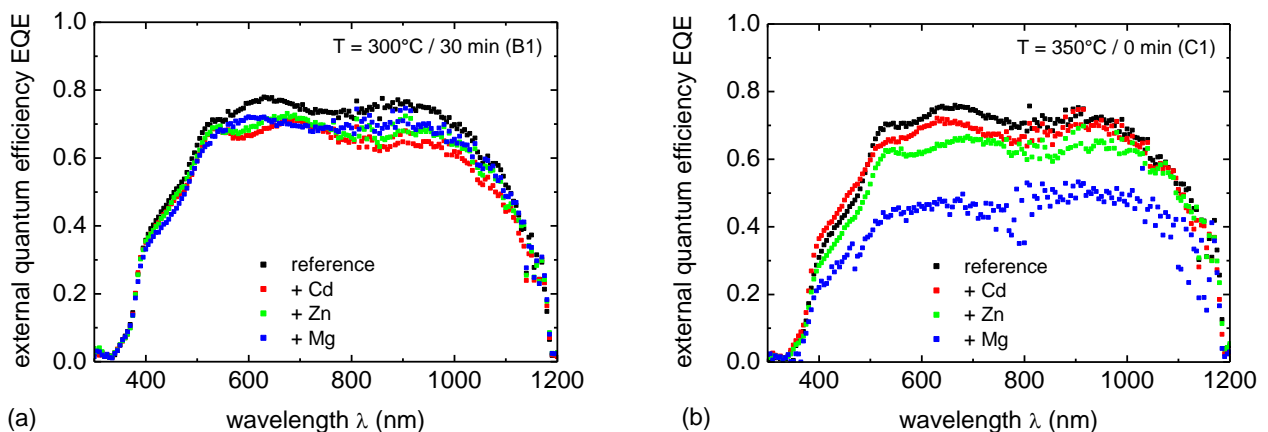
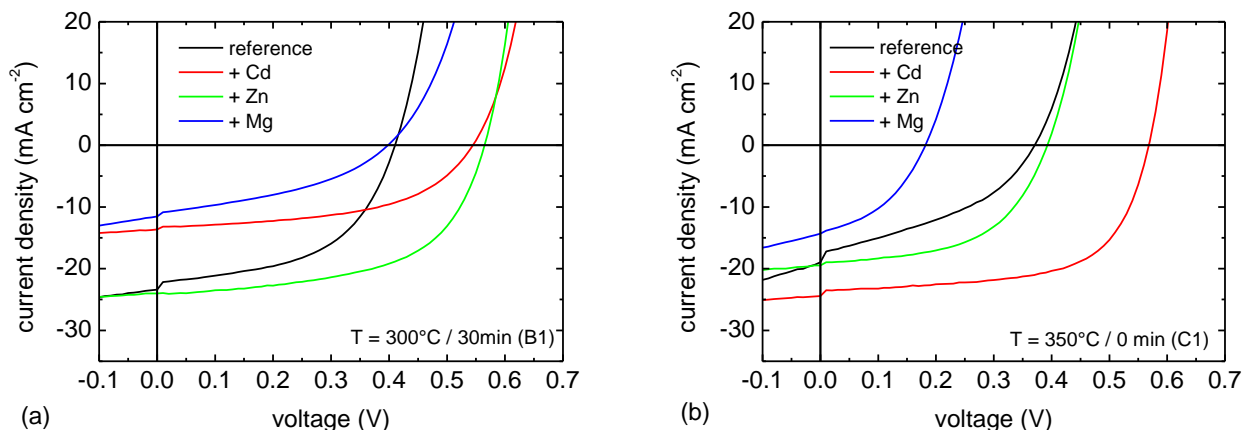**Figure 4.16:** *EQE* **spectra of solar cells with CdS buffer made from Cd-, Zn- and Mg-implanted absorbers after annealing according to procedure B1 and C1 in (a) and (b), respectively. The curves of the corresponding reference cells are plotted for comparison.**

In summary, the *EQE* analysis and modeling exhibits characteristic changes directly after heavy-ion implantation, which can be explained by the existence of an n-type surface layer, but are reversible upon annealing and not specific for the implanted element. Thus, the inversion is presumed to be induced by (deep-level) implantation defects, which may explain the poor *j-V* results. No surface inversion is detectable after B1- or C1-annealing; hence, the inverted layer must be thinner than 20 *nm* if present.

4.5   Buffer-free solar cells by ion implantation

In the Sections 4.2, 4.3 and 4.4, the annealing procedures B1 and C1 have been shown to be suitable candidates for a successful type-inversion of the surface layer of the Cu(In,Ga)Se$_2$ absorber. Hence, the influence of the group-II-element implantation on solar cells without CdS buffer layer is investigated below.

The *j-V*-characteristics of solar cells made from group-II-element implanted absorbers after B1- and C1-annealing are shown in Figure 4.17 (a) and (b), respectively. The average cell parameters are listed in Table A3 in the Appendix. In some curves, a step occurs in the measurement at around 0 *V*,

which is reproducible, but not understood so far. The reference cell shows short-circuit current densities around $20\ mA\ cm^{-2}$, open-circuit voltages around $400\ mV$ and fill factors around 0.4 – altogether leading to an efficiency of only 2 - 4% compared to about 12 - 13% for the cells with CdS buffer from the same run (see Figure 4.12). Analyzing the curves on the basis of the one-diode model, the decrease in FF and V_{oc} is shown to be mainly due to a higher saturation current density of 1 to 5 $10^{-2}\ mA\ cm^{-2}$ and diode ideality factors of 2.5 indicating a very low diode quality.

Figure 4.17: *j-V*-characteristics of solar cells without CdS buffer made from Cd-, Zn- and Mg-implanted absorbers after annealing according to procedure B1 and C1 in (a) and (b), respectively. The curves of the corresponding reference cells are plotted for comparison.

While no improvement occurs for all samples that did not show full recovery in Figure 4.12 (Mg for B1-, Mg and Zn for C1-annealing), both Cd-implanted samples and the B1-annealed Zn-implanted sample show strongly enhanced open-circuit voltages of 500-600 mV. This V_{oc} is almost comparable to the one of cells with CdS buffer and can be reached due to saturation current densities below $10^{-4}\ mA\ cm^{-2}$ and diode ideality factors below or around 2 (best values of $j_0 = 3\ 10^{-6}\ mA\ cm^{-2}$ at $n_{id} = 1.69$ have been reached). This strongly improved diode characteristics show that a good-quality p-n-junction has been fabricated by the use of the implantation technique. However, the efficiency is lowered by low short-circuit current densities (10 - 25 $mA\ cm^{-2}$) and fill factors around 0.5 (mainly due to a shunt resistance of only around 100 $\Omega\ cm^2$).

Measuring the *C-V*-characteristics (shown in Figure 4.18), a voltage-dependent capacitance is observed with similar shape as for cells made with the standard CdS buffer, but rather large capacitances up to 200 $nF\ cm^{-2}$. While the reference cell exhibits doping densities in the normal range (10^{15}-$10^{16}\ cm^{-3}$), the implanted samples show significantly larger densities up to 5 $10^{17}\ cm^{-2}$. Due to the low parallel resistance, the real capacitance may be even larger than these measured values [Blo92]. The capacitance is always determined from charge fluctuations at both sides of the p-n-junction in *C-V*-analysis. As not even the exact position of the p-n-junction is known in this case, it is not clear, which doping density is calculated for ion implanted absorbers.
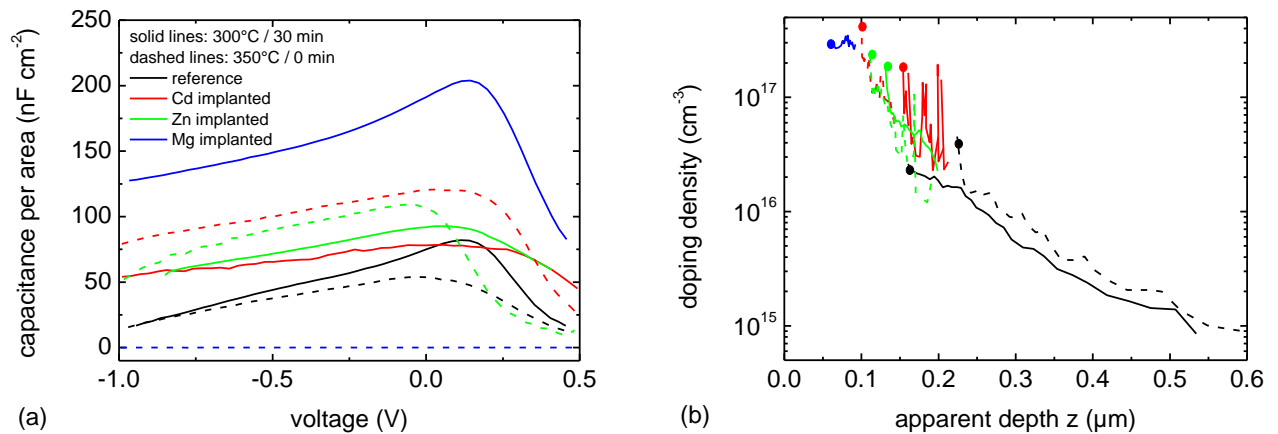
Figure 4.18: (a) *C-V*-characteristics of solar cells without CdS buffer made from Cd-, Zn- and Mg-implanted absorbers after annealing according to procedure B1 and C1 and compared to the corresponding reference. **(b)** Doping profiles calculated from the *C-V*-curves shown in part (a) of this figure; the full circles mark the 0 *V*-position.
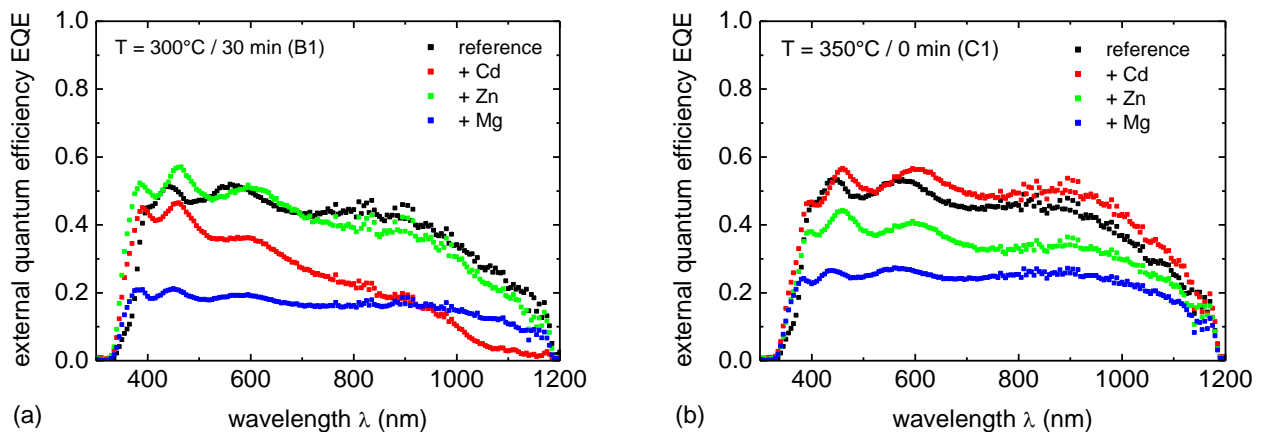

Figure 4.19: *EQE* spectra of solar cells without CdS buffer made from Cd-, Zn- and Mg-implanted absorbers after annealing according to procedure B1 and C1 in (a) and (b), respectively. The curves of the corresponding reference cells are plotted for comparison.

As the main loss occurs due to low j_{sc}, the *EQE* of the cells is measured and depicted in Figure 4.19 (a) and (b) for both annealing procedures. All cells, including the reference, show very low maximum *EQE* of below 0.6, which is explained in the model by enhanced interface recombination. In analogy to the *EQE* findings on the comparable cells with CdS in Figure 4.16, both Mg-implanted and the C1-annealed Zn-implanted sample show even higher interface recombination, whereas the low short-circuit current density of the B1-annealed Cd-implanted sample is found to be due to a strongly decreased collection length of only 120 *nm* (a collection length of about 500 *nm* is obtained for the other devices). This decrease may be caused by a stronger diffusion of the implanted Cd ions during the longer annealing procedure (B1), which is avoided by the shorter process time (C1). In contrast, the Zn-implanted absorbers seem to need a longer annealing procedure as found in the *EQE* and *j-V*-measurements of cells both with and without CdS. Therefore, different annealing conditions are presumed to be needed for Cd- and Zn-implantation.

The high interface recombination found in the *EQE* analysis may be due to the surface damage induced by the sputtering process during ZnO-deposition [Shi08], which is avoided by protecting the surface with the CBD-grown CdS layer in the standard configuration [Rau99b] (see Section 2.2.1). This sputtering damage has been successfully reduced by post-deposition annealing [Shi08]. In this work, a thermal treatment for 30 *min* at 150°C in air is found to be an optimum annealing procedure. The *j-V*-characteristics of the same samples as in Figure 4.17 are shown in Figure 4.20 (a) and (b) for B1- and C1-annealing, respectively, as measured before and after the post-annealing step. The average cell parameters after post-annealing can be found in Table A4 in the Appendix. A recovery of the short-circuit current density is observed for all cells. As this recovery is partly accompanied by an increase of the saturation current density, reduced open-circuit voltages are observed in some cells, which leads to decreased efficiencies for higher annealing temperatures.

The best buffer-free solar cells made on the basis of this implantation technique are displayed in Figure 4.21 and compared to the best reference with CdS buffer from the same absorber deposition process. The solar cell parameters are shown in Table 4.1 for all these five devices. Zn- and Cd-implantation can be seen to lead to strongly enhanced open-circuit voltages when compared to the reference without CdS. The V_{oc} is found to be very close to the one of the reference sample with CdS buffer, which can be explained by a clearly improved diode behavior (j_0, n_{id}). A highest efficiency of 10.2% is measured for a Cd-implanted device after C1-annealing and post-window-deposition annealing. When comparing the performance to the one of a reference cell with CdS buffer layer, losses are due to reduced current collection (j_{sc}) and a lower fill factor, which is mainly caused by a very low shunt-resistance R_{sh}.
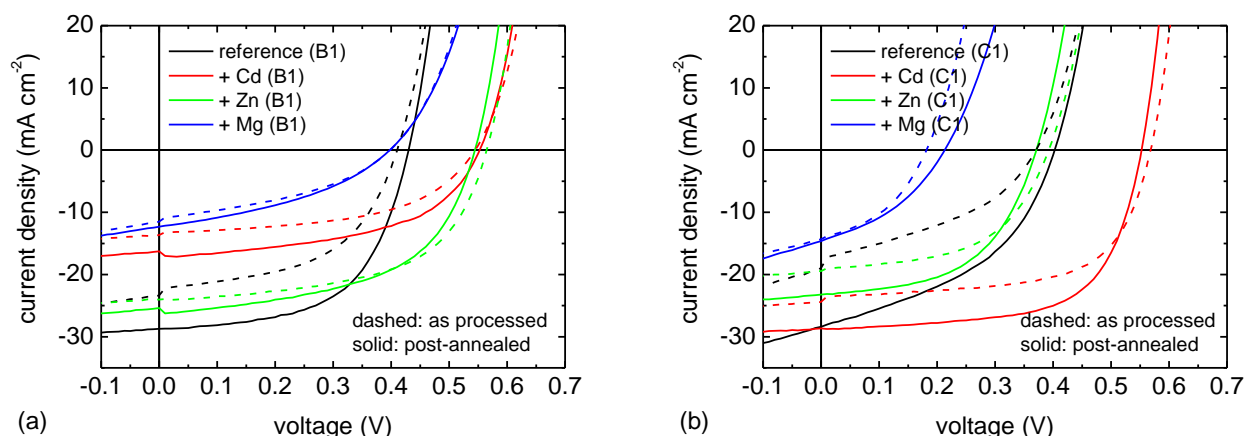

Figure 4.20: (a) *j-V*-characteristics of selected solar cells without CdS buffer made from Cd- and Zn-implanted absorbers before and after post-window-deposition annealing and compared to the corresponding reference.

Summary

The role of near-surface ion implantation in Cu(In,Ga)Se$_2$ absorber layers for solar cell fabrication has been examined. An n-type surface layer is shown by SCAPS simulations to be very beneficial for solar cells suffering from high interface recombination.

In the experiments, an annealing procedure was found that avoids degradation of the solar cell properties made from annealed absorbers, minimizes the diffusion of the implanted ions and recovers the solar cell degradation induced by implantation damage, as consistently found by different methods. The annealing process needs to be adapted to each dopant element; diffusion may be a critical issue in some cases.

Although an effective n-type doping by the dopants has not been measured directly by any of the applied methods, buffer-free solar cells made from implanted absorbers showed strongly improved diode characteristics (saturation current density, diode ideality factor) comparable to the one of reference cells with CdS buffer as shown in Figure 4.21. A maximum efficiency of (10.2±0.6)% [(11.2±0.7)% active area] is obtained for a buffer-free solar cell made from a Cu(In,Ga)Se$_2$ absorber after 20 *keV* Cd-implantation and subsequent thermal treatment.
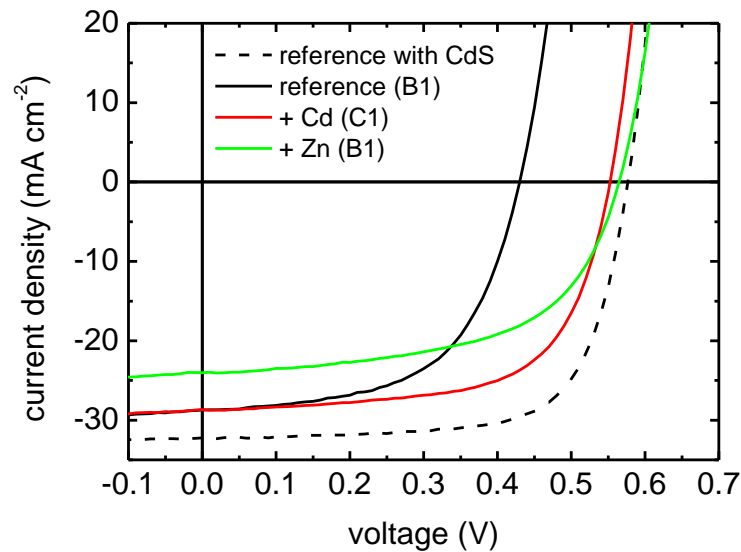
Figure 4.21: Comparison of the *j-V*-characteristics of the best buffer-free solar cells to a typical reference cell with CdS buffer.

	j_{sc} (mA cm^{-2})	V_{oc} (mV)	FF (%)	η (%)	R_{sh} (kΩ cm^2)	R_s (Ω cm^2)	n_{id}	j_0 (mA cm^{-2})
reference w/ CdS	32.2	577	0.701	13.03	0.696	0.173	1.80	1.26 10^{-4}
ref. w/o CdS (B1)	28.8	430	0.576	7.13	0.199	0.179	2.37	2.37 10^{-2}
+ Cd (C1)	28.8	553	0.642	10.20	0.231	0.087	1.94	4.30 10^{-4}
+ Zn (B1)	24.0	565	0.574	7.78	0.175	0.116	2.09	5.26 10^{-4}

Table 4.1: Solar cell parameters of the best buffer-free solar cells compared to the best reference cell with CdS buffer from the same absorber deposition process.

5 Luminescence of Ga-graded Cu(In,Ga)Se$_2$ thin-films

In this chapter, cathodoluminescence (CL) is used to study the transport and recombination properties of Ga-graded Cu(In,Ga)Se$_2$ thin-films with a lateral resolution in the order of 100 nm. The influence of the grading is investigated by monochromatic CL cross-section imaging and a model is developed to describe the charge carrier transport in the quasi-electric field (Sections 5.1 and 5.2). This model is used to explain both CL and PL data obtained in standard plan-view configuration (Sections 5.3 and 5.4). Numerical simulations with SCAPS-1D and analytical calculations are developed to describe the influence of charge carrier motion (Section 5.5). Also, the influence on lateral CL imaging is discussed (Section 5.6). The results described in this chapter have partially been presented at the Frühjahrstagung of the Deutsche Physikalische Gesellschaft (DPG) 2011 in Dresden and have been submitted for publication.

5.1 Ga-grading measurement and standard CL measurements

As discussed in Section 2.3.2, a band-gap double-grading is used in high-efficiency Cu(In,Ga)Se$_2$ solar cells. Absorbers deposited by multi-stage co-evaporation at the HZB also show such a grading [Kau09; Cab10]. The Ga-profile has been measured for the samples used for the CL analysis by SIMS and EDS as shown in Figure 5.1(a). EDS analysis has been performed in two different ways: First, with an SEM using a mechanically polished cross-section sample and an electron energy of 10 keV and secondly, with a TEM using a FIB-prepared lamella and an electron energy of 300 keV. All data have been scaled to agree with the integral GGI of 0.3 measured by means of XRF. The noise of the curves represents the error of the measurements, which is lowest for the SIMS data.

All three methods lead to very similar results: a GGI of 0.3 - 0.4 is found near the front-contact, a minimum of around 0.1 is reached in $z \approx 0.7\ \mu m$ and an increase to 0.5 - 0.6 is observed towards the back. The methods considerably differ in lateral resolution: While the SIMS data average over an area of 50 x 50 μm^2, the lateral resolution of EDS is well below 1 μm in both cases. Thus, the local Ga-grading in single grains is confirmed to be practically equal to the one observed when averaging over a larger area. Recent TEM-EDS mappings also indicate that the local Ga-grading is not at all influenced by the grain structure [Die11]. Measuring the grading with SIMS at different spots (not shown) also confirm a very high lateral homogeneity of the grading on the mm-scale. The SIMS data are used as a reference for the CL investigations in this chapter, because it exhibits the lowest signal noise. Nonetheless, considerable deviations from this profile on the local level cannot be excluded.
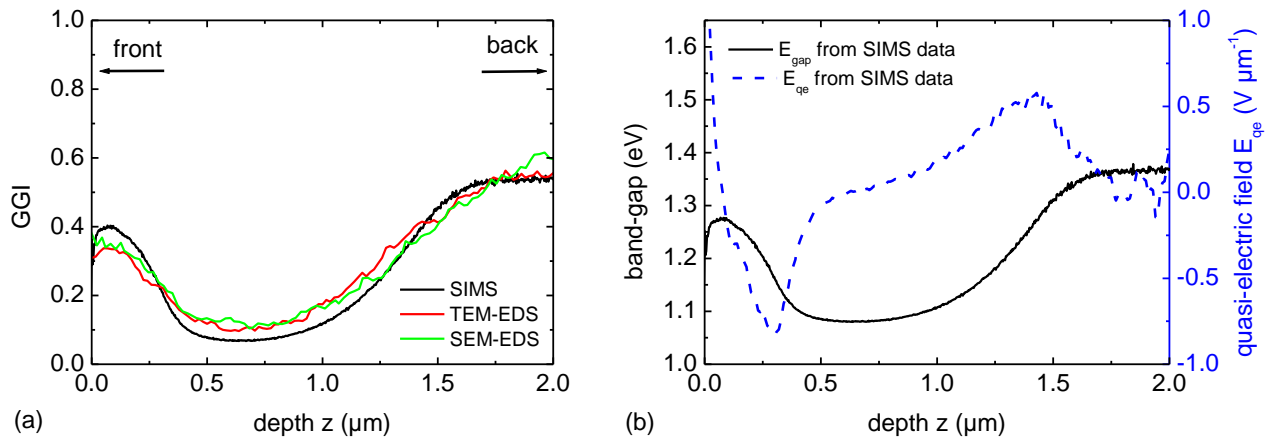
Figure 5.1: (a) Ga-grading as measured with SIMS and EDS, the latter both in SEM and in TEM mode. (b) Band-gap E_{gap} and quasi-electric field E_{qe} as calculated from the SIMS-measured Ga-grading plotted in part (a) of this figure according to Figure 2.10(b) and Eq. (2.17).

The SIMS-measured Ga-profiles are employed to calculate a low temperature $(10\,K)$ band-gap profile according to Figure 2.10(b) and displayed in Figure 5.1(b). The band-gap is seen to vary between 1.1 and $1.35\,eV$ within the sample, which should be clearly detectable by luminescence methods. The quasi-electric field E_{qe} is also calculated from the band-gap grading according to Eq. (2.17) and shown in Figure 5.1(b) (right axis) featuring a maximum field of around $0.5\,V\,\mu m^{-1}$.

For a detailed analysis of the luminescence properties, different CL measurement configurations are applied to the same samples:

(1) Exciting the Cu(In,Ga)Se$_2$ layer from the front (from $z = 0\,\mu m$ in Figure 5.1) as deposited on the Mo back-contact, later referred to as "front". This is the configuration used most frequently in luminescence studies.

(2) Exciting the Cu(In,Ga)Se$_2$ layer from the back (from $z = 2\,\mu m$ in Figure 5.1) after a lift-off from the Mo back-contact, referred to as "back". For the lift-off, the samples were glued upside-down onto a substrate using epoxy-glue; the Cu(In,Ga)Se$_2$ layer remains on the substrate when the glass is pulled off . The configurations (1) and (2) are also referred to as "plan-view".

(3) Exciting a cross-section sample from the side, so the depth of excitation can be varied, referred to as "cross-section". The cross-section samples are prepared by breaking complete solar cells. The edge is mechanically polished using diamond-lapping foil in order to reduce the influence of morphology.

Cathodoluminescence spectra are detected in front and back geometry using the standard parameters as defined in Section 3.2.9 and displayed in Figure 5.2(a) on a logarithmic scale. More than just one emission is observed in the spectra in contrast to what is observed in homogeneous Cu-poor Cu(In,Ga)Se$_2$. All peaks exhibit a broad ($\sigma = 20 - 40\,meV$) and slightly asymmetric shape. All peaks

show a strong blue-shift with rising excitation power (see Section 5.3.3) and can therefore be assumed to be due to qDAP-transitions (see Section 2.3.4). The front side spectrum is dominated by an emission at $E_1 = 0.97\ eV$, which energetically roughly corresponds to the DA1-transition of pure CuInSe$_2$ [GGI = 0.0, Figure 2.10(b)]. Two weaker peaks can be observed at around $E_2 = 1.13\ eV$ and at 0.85 eV. While the latter is believed to be due to deep levels (DL) in the band-gap [Zot97; Str02; Roc03], the E_2-emission can be assigned to the DA1-transition of Cu(In,Ga)Se$_2$ with a GGI of around 0.3, in line with Figure 2.10(b). Excitation from the back of the layer yields a prominent peak at $E_3 = 1.30\ eV$, corresponding to a GGI of roughly 0.55, while a weaker emission is detected at around 1.0 eV.

All features of the plan-view spectra are equally observed, if a spectrum is acquired averaging over the whole depth of the sample in cross-section configuration, as shown in Figure 5.2(b). However, the peaks are broader here, but still the spectrum can be very well fitted using four Gaussian lines centered at energies close to E_{DL}, E_1, E_2 and E_3.
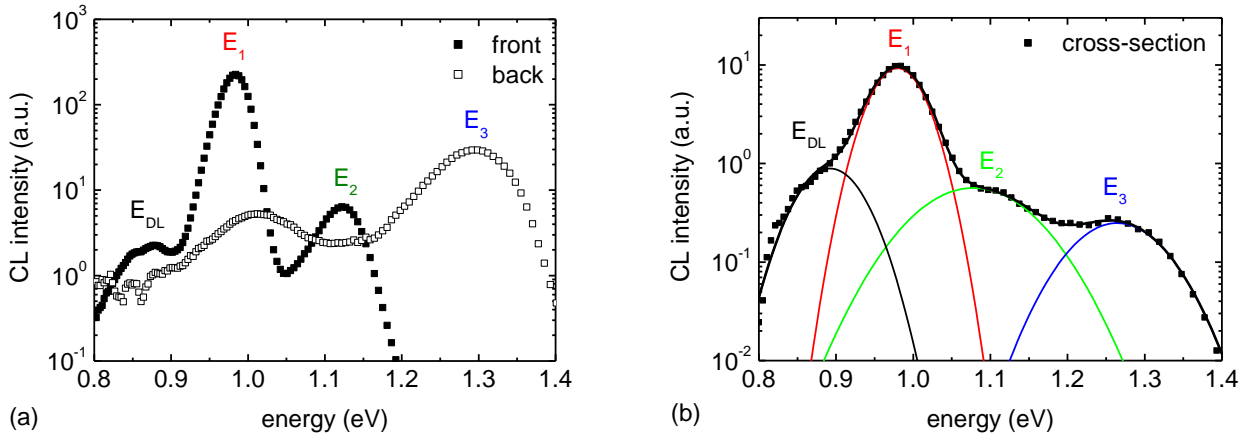
Figure 5.2: Cathodoluminescence spectra as measured in front, back (a) and cross-section configuration (b). The emissions are interpreted to be due to deep-level-transitions (DL) and the qDAP-transition in regions with different Ga-content (E_1, E_2 and E_3).

5.2 Cathodoluminescence in cross-section configuration

The most direct access to the grading can be gained in cross-section configuration. The measurements were performed at a slightly increased beam current of $I_b = 500\ pA$ for a higher signal level. Two complementary modes can be chosen to investigate the spatial distribution of the CL signals: Either the whole spectrum is detected for every spot of excitation (referred to as "point spectra") or an image of the whole area is acquired at a distinct photon energy ("monochromatic imaging"). In any case, one must be aware that the CL intensity is always detected as a function of the spot of excitation, which may not be equal to be position of recombination.

In this work, monochromatic imaging in cross-section configuration is used as a method of choice.

5.2.1 Monochromatic imaging and profiling

A secondary electron (SE) image of a polished cross-section sample is shown exemplarily in Figure 5.3(a). Due to the high beam current, the contrast and resolution of the SE image is rather poor, but still the Cu(In,Ga)Se$_2$ layer and parts of the grain structure are well resolved. Therefore, it is possible to vertically align the CL images along with the corresponding SE image, which was detected simultaneously in order to eliminate a possible drift of the image. The window layers as well as the Mo-layer have detached from the absorber layer during sample preparation as confirmed by EDS-measurements.
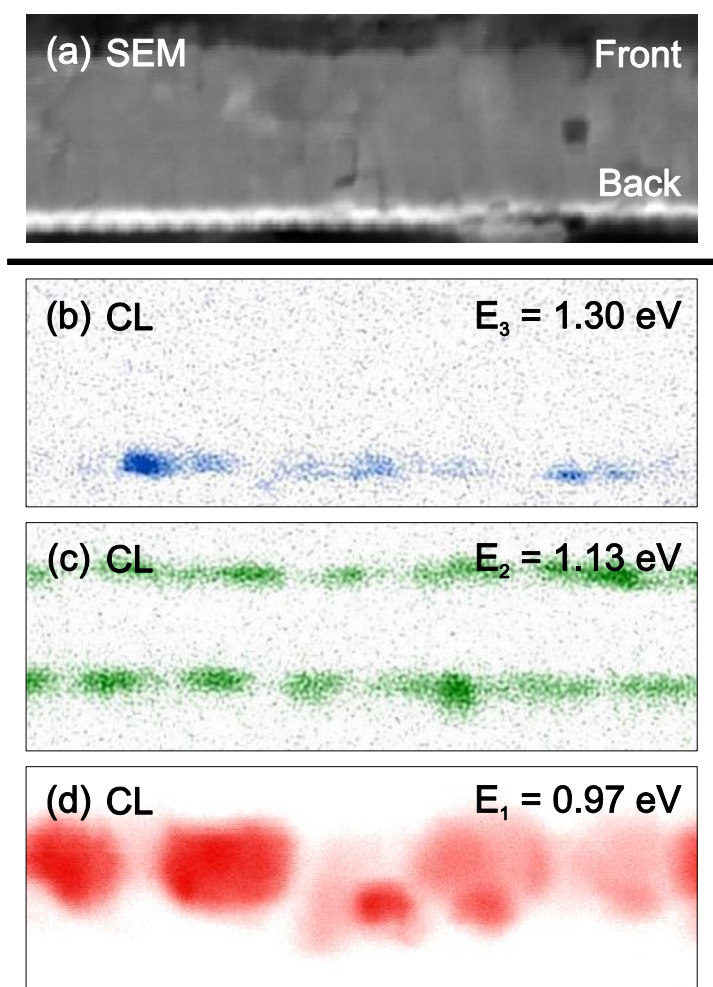
Figure 5.3: Cross-section images of a standard Cu(In,Ga)Se$_2$ solar cell in secondary electron (a) and monochromatic cathodoluminescence modes (b) - (d). The CL images were detected at energies ranging from 0.8 to 1.4 *eV*, the images at the energies E_1, E_2 and E_3 are exemplarily shown.

Monochromatic CL images were detected simultaneously at detection energies E_{detect} ranging from 0.8 to 1.4 *eV*. Exemplarily, the three images at the peak energies E_1, E_2 and E_3 from Figure 5.2 are displayed in Figure 5.3 (b) - (d). In Figure 5.3(b), the E_3-emission appears to be localized at the interface to the back-contact; hence, luminescence at this energy is observed only when the excitation takes place in the back-contact region. At a detection energy of 1.13 *eV* [Figure 5.3(c)],

signals at both the front and at a region close to the back-contact are detected, while strong luminescence is observed at a broad middle region of the absorber for detection at 0.97 eV [Figure 5.3(d)]. Along with these images, the three emission lines in Figure 5.2 can be assigned to the minimum band-gap (E_1), the front (E_2) and the back (E_3) region of the layer.

These findings suggest that monochromatic CL imaging is able to map the band-gap grading in Cu(In,Ga)Se$_2$ thin-films. It can be concluded that it is not justifiable to relate the luminescence peak energies obtained from Ga-graded thin-films to the band-gap calculated from the integral Ga-content as repeatedly done in recent literature [Ish09; Slo10; Paw11; Zac11]. Luminescence peak energies are always determined by the local band-gap at the position of recombination and not by a value calculated from an average stoichiometry. In this work, the dominant emission energy in standard front configuration in Figure 5.2 is shown to correspond to the minimum Ga-content.

In all CL images in Figure 5.3, also the grain structure is well resolved in the luminescent layer. The CL intensity at the grain boundaries is decreased and a large variation in intensity can also be measured between different grains. In order to evaluate the influence of the grading (along the vertical axis), monochromatic CL line scans can be used, which, in this case, shall average over a sufficiently large number of grains. This can most easily be obtained by a projection of the image data on the vertical z axis (summing up all columns). Thus, the CL intensity at a fixed detection energy E_{detect} is extracted as a function of the depth of excitation z_0 from the monochromatic images shown in Figure 5.3 and displayed in Figure 5.4 in logarithmic scale. The profiles at the energies E_3 and E_2 show a one- and two-peak structure, respectively, representing the luminescent layers in the corresponding images; the E_1-emission is rather broadly distributed over the complete layer. The depth z_{max} of the local intensity maxima in Figure 5.4 is determined for each detection energy E_{detect} and marked by vertical black lines. Values of 690 nm (E_1), 60 nm and 1560 nm (E_2) and 1980 nm (E_3) are obtained for the energies E_1, E_2 and E_3, respectively.

Figure 5.4 demonstrates that the E_1-emission is dominant for excitation anywhere in the whole solar cell structure, although it exclusively originates from recombination at the band-gap minimum at around $z \approx 0.7$ μm only. Hence, a significant drift of excited carriers towards the minimum of the band-gap must be present. This drift is presumed to be due to the quasi-electric field E_{qe} induced by the band-gap grading. This provides direct evidence of significant charge-carrier motion in the Cu(In,Ga)Se$_2$ absorber being present even at this low temperatures. The spot of excitation may be different from the position of recombination in our samples. They are separated by the directed motion of charge carriers after excitation. Directed motion (drift) is induced by a gradient in the respective quasi-Fermi level as described in Section 2.3.2, which can be either due to the electric field E of the p-n-junction (depth dependence of the vacuum level) or to the quasi-electric field E_{qe}

in band-gap graded materials (depth dependence of the respective charge carrier affinity). These two possible explanations cannot be distinguished according to Eq. (2.16), but as the drift occurs towards the band-gap minimum, the participation of the quasi-electric field must be presumed.
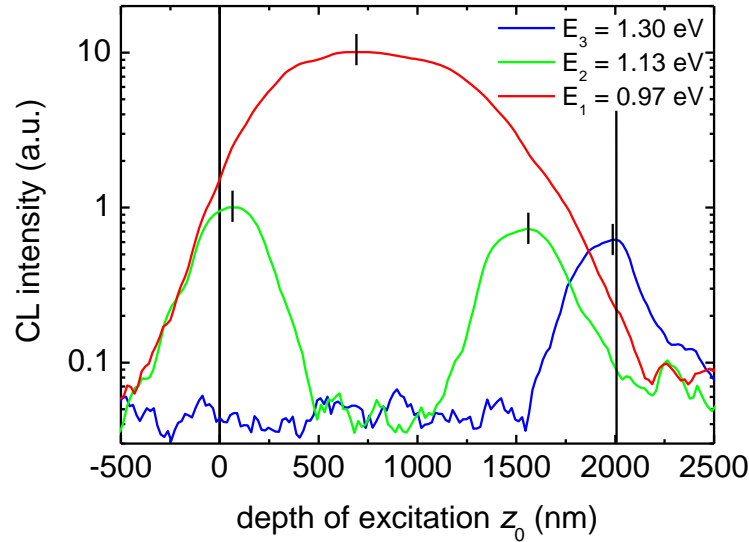

Figure 5.4: Cathodoluminescence depth profiles across the cross-section sample obtained from monochromatic images shown in Figure 5.3. The luminescence intensity is plotted in logarithmic scale as a function of the depth of excitation for the selected emission energies E_1, E_2 and E_3. The depths of maximum intensity z_{max} are marked by vertical black lines.

A short note shall be given here on the choice of monochromatic CL imaging, which was discussed in the beginning of Section 5.2: The presence of the drift implies that the measurement of point spectra will always feature this dominant peak at the same energy E_1 (see Figure 5.4) although the GGI at different points of excitation may vary over a broad range. Hence, it is impossible to determine local properties such as the band-gap by only detecting the luminescence spectra after local excitation, because the signal coming from that very spot will not correspond to the local material properties. Even the grain-like structure observed in Figure 5.3(d) may not correspond to the real grain structure due to charge-carrier drift. These statements are meant to point out the principle difficulties when interpreting the CL signal obtained from samples with significant charge carrier drift or diffusion.

5.2.2 Modeling of charge carrier transport

All observations from Section 5.2.1 shall be summarized in a model. This model shall provide a basis for the interpretation of the monochromatic CL profiles from samples with significant charge carrier motion as the one shown in Figure 5.4. In general, transport processes of charge carriers in a polycrystalline sample consist of the transport over grain boundaries and inside the grains. The following model totally ignores the question, which part of the transport process may limit the carrier mobility. Furthermore, the influence of the electric field at the sample front and back surface

due to Fermi-level pinning induced by charged surface defect states [Rei02; Sad03] will not be considered.

The band diagram of a double-graded absorber is schematically displayed in Figure 5.5(a), featuring a minimum in the band-gap $E_{gap,min}$ and an increase towards both interfaces. Due to the presence of the grading, excited charge carriers will be subject to drift in the quasi-electric field towards $E_{gap,min}$. In the experiment (see Figure 5.4), the CL intensity of the qDAP-transition is detected at a single energy E_{detect} ($E_{detect} = E_{qDAP}$) corresponding to a band-gap energy E_{gap} [see Figure 2.10(b)], which is reached in the layer at a well-defined depth z', as a function of the depth of excitation z_0. If $E_{gap}(z_0)$ is smaller than $E_{gap}(z')$, no luminescence will be detected at E_{detect}, because excited carriers will drift towards the band-gap minimum $E_{gap,min}$ and not pass by the depth z'. But if $E_{gap}(z_0)$ is larger than $E_{gap}(z')$, excited carriers will pass by z', accordingly, luminescence will be detected at E_{detect}. But as a certain number of electrons have recombined already before reaching z', the luminescence intensity I_{CL} is reduced when compared to the maximum intensity of the luminescence, which is reached when the excitation takes place at z' ($z' = z_0$):

$$I_{CL}(z') = \max_{z_0} I_{CL}(z_0) \,. \tag{5.1}$$

The dependence of the intensity on the depth of excitation z_0 can be described by a collection function featuring an exponential decrease of the CL intensity with z_0, as it is shown in Figure 5.5(b) (dashed line). The decrease is characterized by the electron drift length L_{drift} in the quasi-electric field defined by Eq. (2.18)

$$I_{CL}(z_0) = \begin{cases} 0, & z_0 < z' \\ I_{CL,max}\, exp\left[-\left(\dfrac{z_0 - z'}{L_{drift}}\right)\right], & z_0 \geq z' \end{cases} \tag{5.2}$$

Thus, the dependence of the CL intensity at E_{detect} on the depth of excitation z_0 exhibits a peak maximum for $z_0 = z'$. This statement is trivial for homogeneous (non-graded) semiconductors, but also valid when directed charge carriers motion is present as shown above. It is stated here that the validity of Eq. (5.1) does not require the constancy of the drift length over the depth of the sample, but of course a depth dependence of the drift length $L_{drift}(z)$ would lead to deviations from the exponential decrease in Eq. (5.2).

The collection function in Eq. (5.2) is only valid for point-like excitation and is actually superimposed by the (lateral) excitation profile at $E_e = 10\ keV$ [see Figure 2.2(a)] in the case of our measurement. Convoluting the excitation profile and the collection function, an effective intensity profile $I_{CL,eff}(z_0)$ is obtained, which exhibits a broader peak, as exemplarily shown in Figure 5.5(b)

(solid line). Furthermore, a shift of $\Delta z_{max} = z_{max} - z'$ occurs away from the band-gap minimum resulting from the asymmetric shape of the collection function.
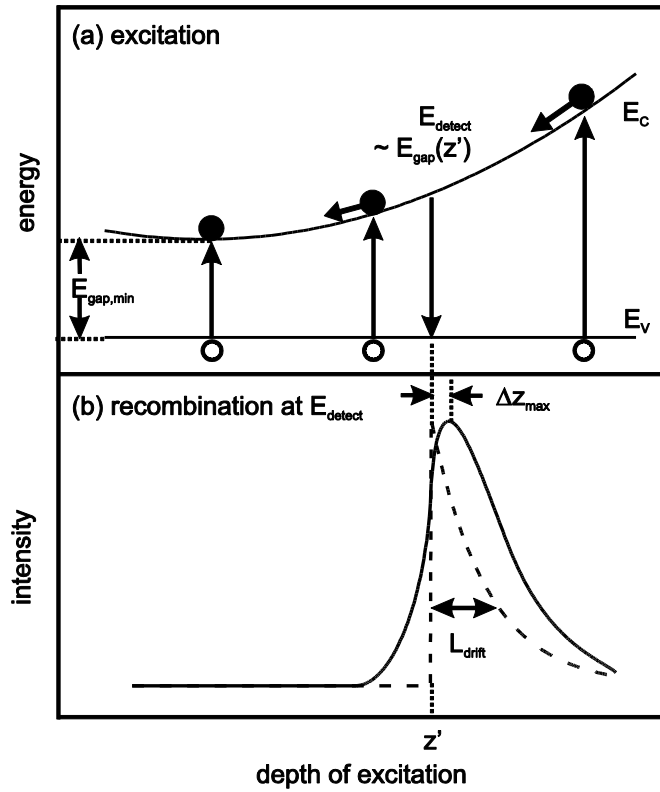

Figure 5.5: Illustration of drift and recombination processes in band-gap graded material. (a) Band-diagram of the Cu(In,Ga)Se$_2$ layer with a minimum at $E_{gap,min}$. Three excitation processes and the corresponding drift direction of the excited electrons are exemplarily shown. Recombination is observed at a distinct energy E_{detect} corresponding to the band-gap at z'. (b) Modeling the CL intensity observed after point-like excitation (collection function, dashed line) and taking into account the excitation profile at 10 keV (effective intensity profile, solid line) as a function of the depth of excitation z_0. The drift length L_{drift} determines the width of the profile, the shift Δz_{max} occurs due to convolution of the excitation profile and the collection function.

Although the CL intensity profile at a fixed energy is given by a convolution of the excitation function and the collection function, the drift length L_{drift} can still be determined by fitting the slope of the CL intensity profiles towards increasing band-gaps. This is demonstrated in Figure 5.6(a). Here, the excitation profile and effective intensity profiles are displayed for $E_e = 10 \, keV$ and different drift lengths ranging from 100 nm to 5 μm. In the whole parameter range, the drift length can be very well determined by fitting the slope towards higher band-gaps. The slope towards the band-gap minimum is solely determined by the excitation profile of the electron beam, which also sets a lower resolution limit for drift length determination (ca. 100 nm at 10 keV). Additional inaccuracies occur if the excitation takes place close to the end of the layer.

In Figure 5.6(b), the same three profiles are shown as in Figure 5.4. Indeed, all (seven) slopes exhibit an exponential decrease and can be fitted using Eq. (5.2). For all (three) slopes towards $E_{gap,min}$, a characteristic length of 90±10 nm is obtained, which is determined only by the excitation

profile as discussed above. The drift length is determined to 130±20 *nm* towards the window layers and 220±30 *nm* in the absorber towards the back-contact. These values must be regarded as average values, since variations in L_{drift} are assumed to be present both vertically and laterally in the sample. Additionally, a shift of the peak maximum Δz_{max} is observed in Figure 5.6(a), which gradually increases with increasing drift length. While the shift can be shown to be well approximated by $\Delta z_{max} \approx L_{drift}/3$ for drift lengths up to 500 *nm*, it saturates at a maximum of 350 - 400 *nm* for higher drift lengths (for $E_e = 10\ keV$). Due to this shift Δz_{max}, Eq. (5.1) is only approximately valid – but in our case, the shift ($L_{drift} \approx 220\ nm$, thus $\Delta z_{max} \approx 70\ nm$) is found to be small when compared to the dimensions of the Ga-profile.

For the validity of Eq. (5.1) it has to be furthermore assumed that the minority carrier lifetime $\tau(z')$ at every depth z' is independent of the excitation conditions. The dependence of the lifetime τ on the injection density Δn is a common phenomenon in semiconductors [Sze81]. For example, the limited availability of recombination centers can lead to a saturation of recombination rates and therefore an increase of the effective lifetime with increasing injection, while for very high densities, the lifetime decreases due to Auger-recombination [Fon81; Lau09]. As both recombination and transport processes lead to a decrease of the injection density with time after excitation, the injection density at a defined depth z' will decrease when scanning the spot of excitation z_0 towards larger band-gaps (see Figure 5.5). This means that the lifetime $\tau(z')$ may depend on the spot of excitation z_0. While a decrease of the lifetime with increasing injection density would not influence the depth of maximum recombination [Eq. (5.1) remains approximately valid], an increase would lead to a shift of z_{max} towards higher band-gaps comparable to the shift Δz_{max} due to the extension of the excitation volume.
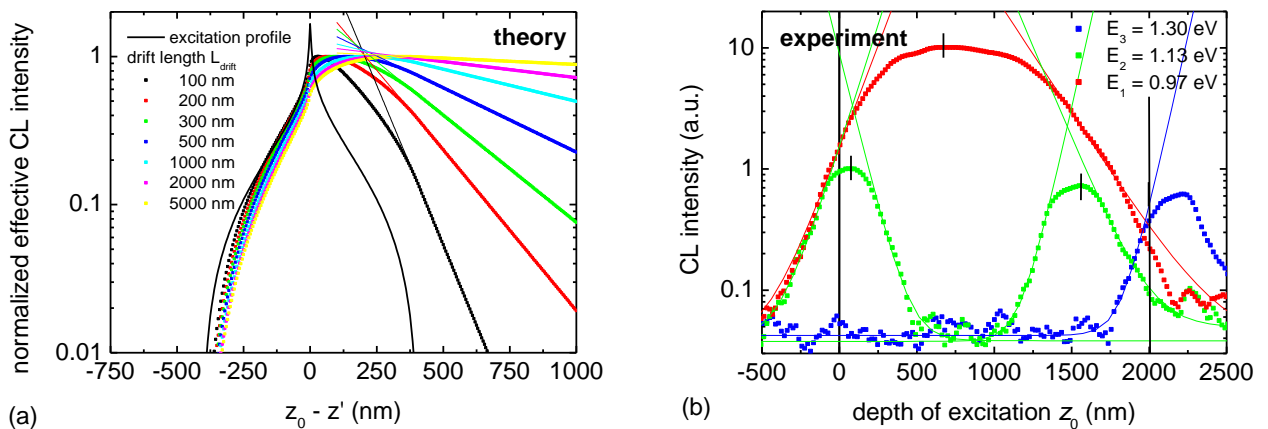

(a) (b)

Figure 5.6: (a) Theoretical effective intensity profiles with respect to the excitation profile at $E_e = 10\ keV$ for different drift length L_{drift} (squares); the pure excitation profile (equivalent to $L_{drift} = 0\ nm$) is shown for comparison (black line). The effective profiles are fitted according to Eq. (5.2) at the side of increasing band-gaps to re-extract the drift length; the profile is independent of the drift length towards the band-gap minimum. (b) Determination of the drift lengths by fitting the CL depth profiles from Figure 5.4 according to Eq. (5.2).

The diffusion of carriers has also been neglected in this model. This can be justified if the diffusion length is found to be small compared to the drift length [combining Eqns. (2.13) and (2.18)]:

$$L_{diff} = \sqrt{\frac{k_B T}{q} \mu_e \tau_e} = \sqrt{\frac{k_B T}{q} \frac{L_D}{E_{qe}}}. \tag{5.3}$$

Using the drift length L_{drift} of 220 *nm* and a quasi-electric field of $E_{qe} = 5 \ 10^5 \ V \ m^{-1}$ [see Figure 5.1(b)] the diffusion length L_{diff} is determined to be around 20 *nm*. Thus, diffusion can be neglected in the model. From the drift length, the effective electron mobility μ_e is estimated to 0.5 *cm^2 V^{-1} s^{-1}* using Eq. (2.18) and assuming a lifetime of 10 *ns*.

5.2.3   Influence of the measurement conditions on the drift length

The charge carrier transport must be assumed to be influenced by the measurement conditions. In order to get an estimate of this influence, the measured drift length L_{drift} is determined as a function of the electron energy E_e, the sample temperature T and the beam current I_b. The measurements were performed at a different position of the sample – a higher drift length of about 400 *nm* is found here under standard conditions. Moreover, the analyzed lateral area is increased by a factor of four compared to Figure 5.3, which allows to average over a larger number of grains and, thus, leads to improved statistics.

The measured drift length is shown as function of the electron energy in Figure 5.7(a) as measured at a temperature of about 10 K and a constant beam power of 3 μW. The measured drift length is seen to clearly increase with the electron energy, which is presumed to be caused by the limited lateral resolution at high energies. The lateral resolution is found in Figure 2.3 to be proportional to $E_e^{1.684}$ – thus, in a first approach, the measured drift length can be modeled as the sum of the unaffected drift length $L_{drift, \ 0 \ keV}$ and the apparent increase due to the size of the excitation volume:

$$L_{drift}(E_e[keV]) = L_{drift, \ 0 \ keV} + A \cdot (E_e[keV])^{1.684}. \tag{5.4}$$

A fit according to Eq. (5.4) shows very good agreement with the data points up to 25 *keV* and an unaffected drift length of about 450 *nm* at this beam power and sample temperature. For the electron energy of 30 *keV*, the large excitation volume led to very unstable measurement conditions due to severe charging effects in the epoxy glue.

The drift length L_{drift} is proportional to the $\mu\tau$-product according Eq. (2.18) – therefore, the temperature dependence of the drift length can be ascribed to the temperature dependence of the carrier mobility and lifetime. The hole mobility is commonly presumed to be dominated by hopping

conduction in Cu-poor Cu(In,Ga)Se$_2$ at these low temperatures, which leads to a strong increase of the mobility with increasing temperature [Sch00a; Sie03; Sie05a; Rei10]. The electron drift mobility μ_e is difficult to access by experimental methods and is often assumed to be comparable or somewhat higher compared to the hole drift mobility due to the smaller effective mass of electrons compared to holes [Glo05a; Met09]. The electron lifetime τ_e in polycrystalline Cu(In,Ga)Se$_2$ solar cell absorbers is commonly measured by time-resolved photoluminescence (TRPL) [Pue96; Ohn98; Pal04; Shi06; Shi07; Met09], which measures the decay time of the PL signal. Puech et al. [Pue96] carefully analyze the influence of carrier trapping by defects and the injection density on the PL decay curves and obtain a low-injection-regime free-electron lifetime $\tau_{e,free}$ of around 1 ns for Cu-poor CuInSe$_2$ and Cu(In,Ga)Se$_2$ at 10 K, which is comparable to values found at room-temperature where band-to-band transitions prevail (1 – 100 ns, [Ohn98; Pal04; Shi06; Shi07; Met09]). Much longer lifetime $\tau_{e,trap}$ are observed for the DA-luminescence due to carrier trapping – but this is not relevant for the carrier transport processes investigated here. Altogether, an increase of the drift length with temperature can be expected.

The temperature dependence of the measured drift length is plotted in Figure 5.7(b) ($E_e = 10\ keV$, $I_b = 750\ pA$). While the measured drift length is fairly independent of the temperature up to 120 K, it shows a significant increase to about 800 nm above this temperature. The invariance of the drift length at low temperature is inconsistent with any temperature activated process such as hopping conduction. Hence, it is assumed that the low-temperature transport properties determined by this CL technique are more or less unaffected by thermal processes. The temperature range of the increase in the measured drift length (120 - 150 K) coincides with the change from free-to-bound to band-to-band transitions in luminescence measurements [Kir07] as well as the disappearance of hopping conduction [Sie05a; Rei10].
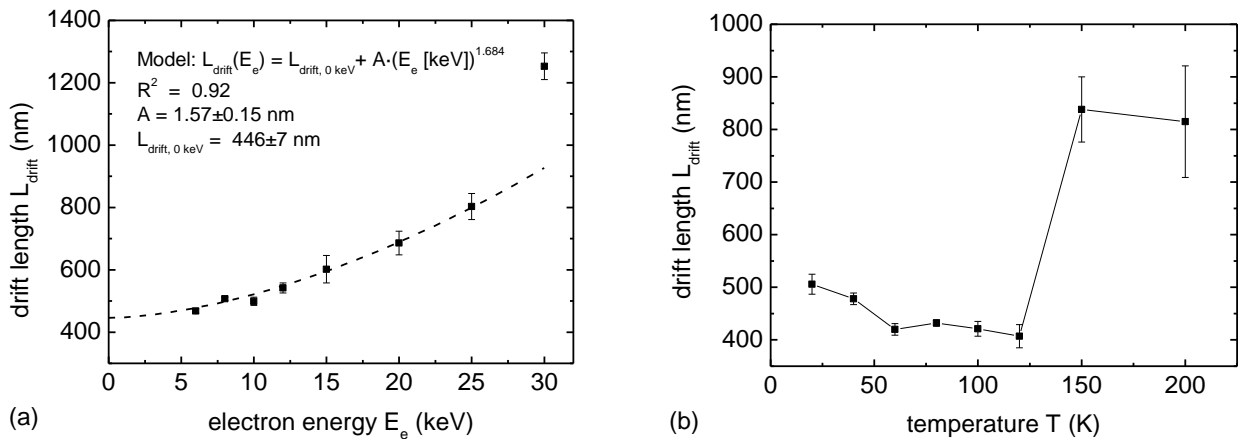
Figure 5.7: (a) Dependence of the measured drift length on the electron energy at $T = 10\ K$ a beam power of $3\ \mu W$. The data are fitted according to Eq. (5.4) (fitting parameter inset). (b) Temperature dependence of the measured drift length at $E_e = 10\ keV$ and $I_b = 750\ pA$.
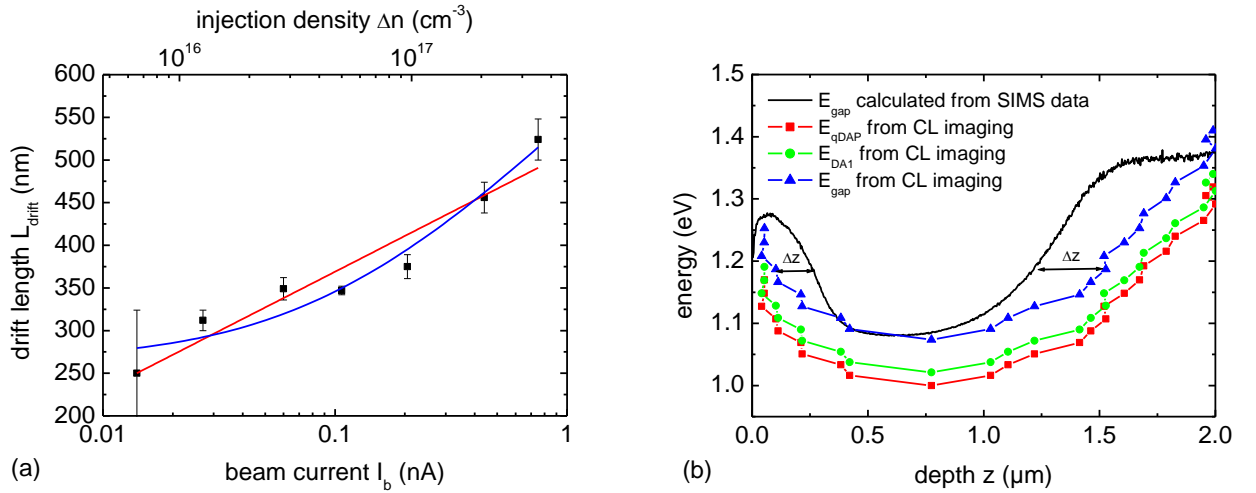
Figure 5.8: (a) Current dependence of the measured drift length at $E_e = 10\ keV$ and $T = 10\ K$. The data are fitted with a logarithmical law with (blue line) and without (red line) saturation at low beam currents. (b) Band-gap grading calculated from the SIMS measurement (solid black line) and compared with band-gap grading data obtained from CL monochromatic imaging evaluation (blue triangles). Additionally, the profile of the qDAP-transition energy is displayed as directly obtained from the profiles shown in Figure 5.4; the DA1-transition energy profile differs from the latter by the shift ΔE.

If the transport properties are hardly affected by temperature, they may be mainly determined by the injection conditions. Current-dependent CL measurements ($T = 8\ K$, $E_e = 10\ keV$) are shown in Figure 5.8(a) [injection density calculated according to Eq. (2.6)] confirm an increase of the drift length with beam current – a logarithmic increase of more than 200 nm per decade is found for high currents.

The data cannot clearly show if there is a saturation of the drift length at low beam currents or not – both interpretations seem possible as shown by the two fits in the figure (blue line: saturation at 270 nm, red-line: without saturation). However, the measured drift lengths must be presumed to be strongly affected by the injection conditions. This may be due to an increased free electron lifetime $\tau_{e,free}$ (due to a decrease of available trap states) or the electron drift mobility μ_e (due to a decrease of the amplitude of potential fluctuations active in optical transitions γ_{opt}, see Section 5.3.3). Charge carrier mobilities and/or lifetimes are concluded to be clearly enhanced at high carrier concentration. This may explain why the effective electron mobility μ_e of 0.5 $cm^2\ V^{-1}\ s^{-1}$ observed here is by far larger than low-temperature hole mobilities obtained from electrical measurements [Sie03; Sie05a; Rei10].

5.2.4   Measurement of the band-gap grading

In Section 5.2.2, the dependence of the CL intensity at E_{detect} on the depth of excitation z_0 is found to have a maximum close to $z_0 \approx z'$: the difference $\Delta z_{max} = z_{max} - z'$ is shown to be rather small ($< 100\ nm$). This means that the local maxima of the monochromatic line scans z_{max} in Figure 5.4 can be interpreted as the depth z', from which the qDAP-emission at the detection energy E_{detect}

originates. Thus, the model described in Section 5.2.2 enables us to correlate the observed position of maximum CL intensity to a well-defined position of recombination. Assuming that all detected emissions are due to qDAP-transitions ($E_{detect} = E_{qDAP}$), the depth dependence of the qDAP-emission energy is obtained, if the detection energy E_{detect} is plotted as a function of z_{max} spot by spot. These values are displayed in Figure 5.8(b) as red squares.

In order to calculate the band-gap profile $E_{gap}(z)$ from $E_{qDAP}(z)$, two additional correction terms have to be considered: the red-shift in Cu-poor Cu(In,Ga)Se$_2$ and the defect level energies E_D and E_A of the contributing defects. As described in Section 2.3.4, the shift of E_{qDAP} to lower energies of Cu-poor Cu(In,Ga)Se$_2$ material, can be compensated at high injection level. A saturation of the blue-shift is obtained at an energy $\Delta E = 21 \pm 3 \, meV$ above the one measured at $0.5 \, nA$ for the peak energies E_1 in plan-view configuration, as will be shown in Section 5.3.3. The respective donor and acceptor energies of the DA1-transition are taken from the defect model of Rega et al. [Reg05] [see Figure 2.10(a)]. The saturated DA1-energy profile and the band-gap profile are calculated and displayed in Figure 5.8(b) as green circles and blue triangles, respectively. Thus, the band-gap profile of a polycrystalline Cu(In,Ga)Se$_2$ thin-film exhibiting significant charge carrier drift in the quasi-electric field is shown to be accessible by means of monochromatic CL imaging. For a sample with negligible charge carrier motion, the band-gap profile can also be derived from local luminescence analysis (point spectra).

Comparing the CL measured profile with the band-gap profile calculated from SIMS using the data shown in Figure 2.10(b) [Alo02; Reg05], a good agreement can be found between both methods for the general shape of the curve. The band-gap reaches its minimum of around $1.1 \, eV$ at a depth of around $700 - 800 \, nm$ and increases up to 1.25 and $1.40 \, eV$ towards the front- and back-contact, respectively. Between both curves, an off-set Δz of approximately 150 and $300 \, nm$ is present towards the front- and back-contact, respectively. In general, such an off-set is in agreement with the shift of the peak maximum Δz_{max} due to the excitation profile or due to an increase of the lifetime τ with increasing injection density Δn as described in Section 5.2.2. Remember that the difference may also be caused by the very different physical principles of both methods: While SIMS only detects the distribution of the atoms averaged over a larger lateral area, CL is sensitive to the local electrical properties and may be influenced by localized charges and defect levels e.g. at the surface.

5.3   Cathodoluminescence in plan-view configuration

The standard configuration for most luminescence investigations is the plan-view geometry. In this section, detailed investigations are presented in both front and back geometry, also considering the influence of the electron energy E_e (voltage dependence), the sample temperature T and the beam

current I_b on the spectra. The charge carrier drift model from Section 5.2 is employed to interpret the data.

5.3.1 Voltage-dependent cathodoluminescence

The variation of the electron energy (or electron acceleration voltage, therefore commonly referred to as voltage-dependent CL [Par07]) leads to changes in energy depth profile $\varepsilon(z)$ and also in the injection density Δn (see Section 2.3.1). With increasing electron energy E_e, the energy is deposited deeper into the layer, leading to changes in the ratio of near-surface- (E_2 and E_3 for front and back, respectively) and band-gap-minimum- (E_1) recombination. This can be demonstrated by calculating a hypothetical CL spectrum by assuming a Gaussian peak shape of the DA1-emission with a standard deviation of $\sigma = 20\ meV$ and using the energy depth profile $\varepsilon(z)$ [taken from Figure 2.2(a)] as a weighting function:

$$CL(E) \sim \int_{0\ \mu m}^{2\ \mu m} \varepsilon(z)\ exp\left[-\frac{1}{2}\left(\frac{E - E_{DA1}(z)}{\sigma}\right)^2\right] dz\,. \tag{5.5}$$

The depth profile of the DA1-transition energy $E_{DA1}(z)$ is calculated from the SIMS data shown in Figure 5.1(b) and adjusted to front and back geometry, respectively. Eq. (5.5) is used to calculate hypothetical voltage-dependent CL spectra in front and back configuration as shown in Figure 5.9 (a) and (b), respectively. When exciting from the front, only one peak at 1.2 eV (associated with the E_2-emission in Section 5.2) is observed for low voltages; an additional peak at around 1.0 eV (E_1) appears for voltages above 8 kV. The intensity ratio IR_{front} of the two emissions defined by $IR_{front} \equiv I_{CL}(E_1)/\ I_{CL}(E_2)$ increases from close to zero at 2 kV to three at 30 kV. A third emission at 1.3 eV (E_3) becomes visible for voltages above 20 kV. Excitation from the back yields an emission at 1.3 eV (E_3), which increases in absolute intensity up to 12 kV. Again, the E_1-emission appears for higher voltages leading to a maximum intensity ratio $IR_{back} \equiv I_{CL}(E_1)/\ I_{CL}(E_3)$ close to two. A small signal also appears at around 1.2 eV for the highest voltages.

This approach totally neglects the influence of charge carrier transport (see Section 2.3.2) and re-absorption of photons in the layer (see Section 2.3.5) and assumes a constant radiative recombination efficiency η_{rad} throughout the layer, but it can give an impression of what is expected from voltage-dependent CL spectroscopy on these Ga-graded Cu(In,Ga)Se$_2$ thin-films. The experimental voltage-dependent CL spectra are displayed in Figure 5.10 (a) and (b) as measured at constant beam currents I_b of 250 pA in front and back geometry, respectively, to compare it to the hypothetical spectra.
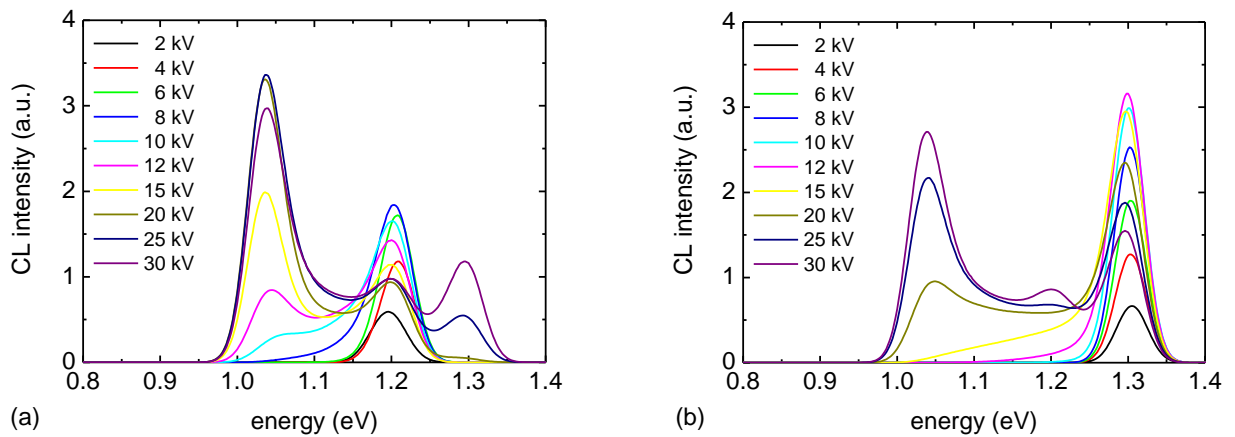
Figure 5.9: Hypothetical CL spectra as obtained from Eq. (5.5) for different electron energies ranging from 2 to 30 *keV* in both front (a) and back (b) configuration.

When measuring the front spectra, the overall CL intensity is observed to strongly decrease for low voltages; therefore the detection parameters (amplification of the photomultiplier) could not be held constant − hence, they are displayed as normalized to the maximum E_1 at around $1.0\,eV$. For all applied voltages, the dominant luminescence signal originates from the band-gap minimum region, although no excitation takes place in this area for voltages below $10\,kV$, as can be seen in Figure 5.9(a). This again is a proof of charge carrier drift towards the band-gap minimum being present in these samples. But it is also observed that the relative intensity of both the E_2- and the *DL*-emission increases with decreasing voltage. This increase of intensity for near-surface excitation suggests the *DL*-emission to be due to recombination via surface defects as also discussed in [Str02; Roc03]. The ratio IR_{front} is very small when compared with the calculations in Figure 5.9(a) − this can also be interpreted to be due to charge carrier motion towards the band-gap minimum leading to preferential recombination at the lowest energy E_1. A peak at $1.3\,eV$ (E_3) cannot be detected (not shown), which can easily be explained by re-absorption.
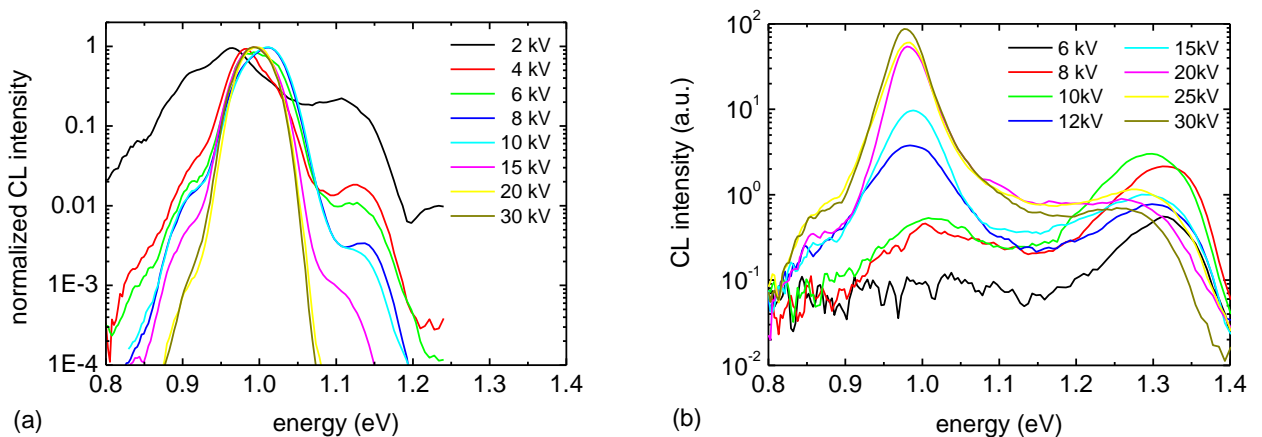
Figure 5.10: (a) Voltage-dependent CL spectra in front configuration normalized to the E_1-emission. (b) Voltage-dependent CL spectra in back configuration as measured.
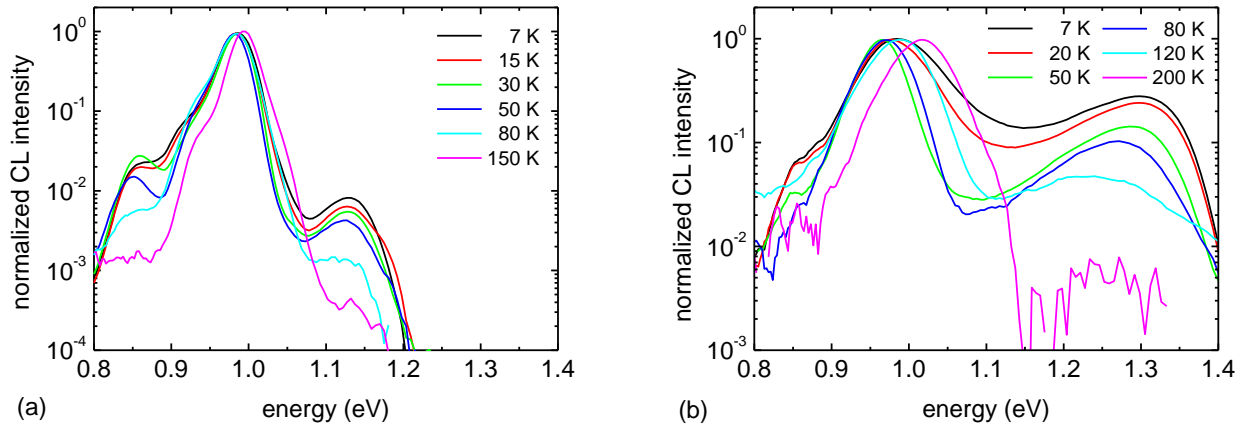
Figure 5.11: Temperature-dependent CL spectra normalized to the E_1-emission in front (a) and back (b) configuration. The spectra from the back are measured for an electron energy of $E_e = 15\,keV$.

The voltage-dependent measurements from the back are performed at constant detection parameters and so can be compared in absolute intensity. The E_1-emission is expected from Figure 5.9(b) to appear for voltages above $12\,kV$ only, but is also found for lower voltages in the experiment due to charge carrier drift. For low voltages, the E_3-emission at $1.3\,eV$ is dominant and increases up to a voltage of $10\,kV$. This behavior is comparable to what was calculated using Eq. (5.5). But also in back geometry, the absolute intensity ratio IR_{back} is by a about factor of 100 higher compared to the calculation, which can be explained by charge carrier drift in the quasi-electric field E_{qe}. No peak is detected at around $1.2\,eV$ (E_2) due to re-absorption.

5.3.2   Temperature-dependent cathodoluminescence

Temperature-dependent luminescence analysis is commonly used to identify the type of transition or the defect level energies [Bau01; Sie04b]. Normally, an overall decrease of peak intensities is observed with increasing temperature T due to an increase in non-radiative recombination [Pan75]. Furthermore, carriers at states with low binding energies (shallow defects, excitons) will dissociate with increasing thermal energy, leading to an additional decrease of transitions involving these states. As the defect energies of the DA1-transition in Cu(In,Ga)Se$_2$ are only weakly dependent on the GGI (see Section 2.3.4), no strong changes in the intensity ratios IR_{front} and IR_{back} can be expected from this point of view.

The temperature-dependent measurements in front (a) and back (b) geometry are displayed in Figure 5.11 in logarithmic scale and normalized to the E_1-emission. Deviating from the standard conditions defined in Section 3.2.9, an electron energy of $15\,keV$ has been used in back geometry. In both cases, a decrease of the relative intensity of the near-surface emissions (E_2-emission for front and E_3-emission for back geometry) is observed. This can be explained by an stronger charge carrier drift towards $E_{gap,min}$ corresponding to an increase drift length L_{drift} already at temperatures of $50\,K$,

which is clearly lower than the transition temperature obtained from cross-section measurements (120 - 150 K). For temperatures above 100 K, an increase of the emission energy E_1 is observed due to the change of the defect-related transition (DA or FB) to a band-to-band transition [Kir07].

5.3.3 Current-dependent cathodoluminescence

Current-dependent measurements from the front are shown in Figure 5.12(a) on a logarithmic scale. Both the E_1 and the E_2-emission show a strong blue-shift with beam current of 10 - 15 meV per decade as expected for a qDAP-transition (see Section 2.3.4) and in accordance with the literature [Dir98; Bau01; Sie04b]. As the local injection density has been found to vary by a factor of around 50 within the excitation volume at constant beam current I_b [see Figure 2.3(b)], this implies an excitation-induced peak width of approximately 20 meV in CL analysis. Comparing this value to the peak width observed in experiment (see Section 5.1), this effect might contribute significantly to the broadening of the peak of the detected qDAP-emissions.

The current dependence of the CL intensity is shown in Figure 5.12(b) for both emissions, which is commonly described by a power law $I_{CL} \sim P^k \sim I_b^k$ with an power exponent k. While the E_2-emission shows a slightly sub-linear behavior typical for defect-related transitions, the E_1-emission exhibit a factor of $k \approx 1.5$, which normally appears for excitonic emissions only [Sch92]. This super-linear increase leads to a decrease of the peak intensity ratio IR_{front} with beam current, which can be explained by an increase of the drift length L_{drift} with the injection density in agreement with the results from Section 5.2.3. The increase of the intensity ratio IR_{front} is in agreement with the power dependence of the relative intensity of the two peaks in regions with a high number of dislocations observed in [Rom03b] (see Section 2.3.4).
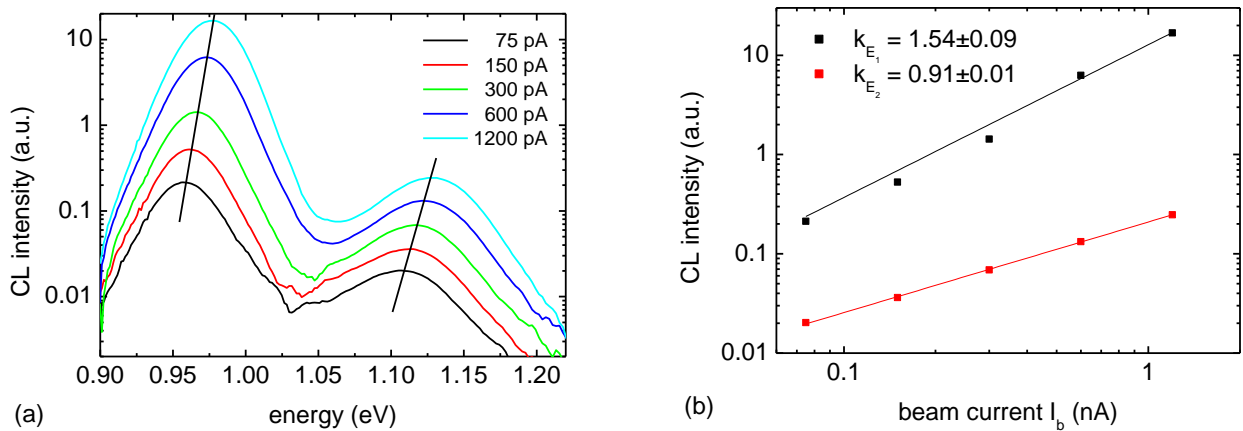
Figure 5.12: (a) Current-dependent CL spectra in front configuration. (b) CL intensity of the E_1 and E_2 as a function of beam current as measured from the spectra in part (a) of this figure with the corresponding k-factors obtained from a power law.
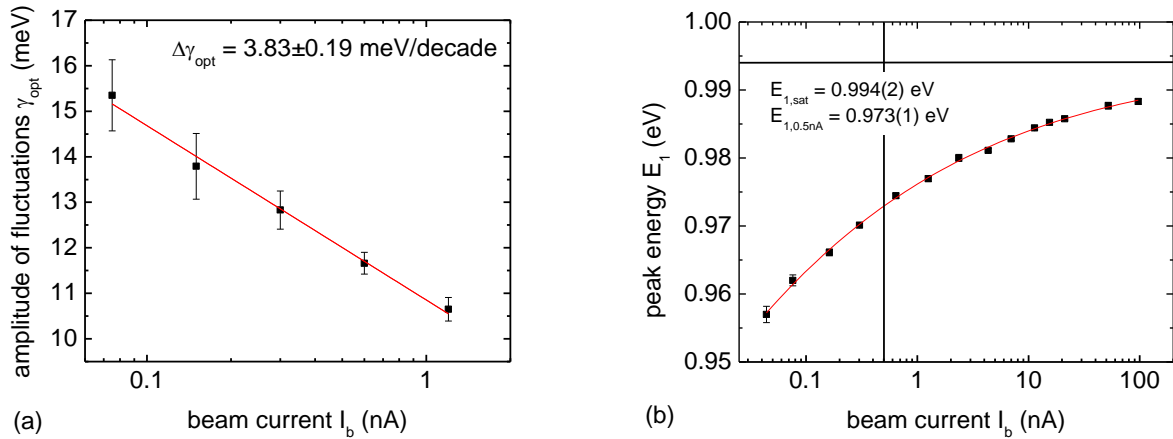
Figure 5.13: (a) Current dependence of the average amplitude of the potential fluctuations γ_{opt} obtained from the fitting the low-energy slope of the E_1-emission in the spectra in Figure 5.12(a), exhibiting a decrease of $\Delta\gamma_{opt} \approx 4\ meV/decade$. (b) Current dependence of the peak energy of the E_1-emission saturating at 0.994±0.002 eV at high beam currents.

For small amplitudes of the fluctuations ($\gamma_{opt} < 40\ meV$), the low-energy slope of the emission peak exhibit an exponential shape and allows to determine γ_{opt} according to $I(E) \sim exp\ [\ (E\text{-}E_0)\ /\ \gamma_{opt}\ ]$ [Sie06]. This fitting has been performed for the E_1-emission of the data from Figure 5.12(a); the results are shown in Figure 5.13(a). An amplitude of the fluctuations in the order of $10 - 20\ meV$ is measured (in agreement with others [Dir98; Sie06]), which decreases about $4\ meV$ per decade with increasing beam current. This is consistent with a successive screening of the localized charges by free carriers and corresponds to a red-shift of the peak of approximately $8\ meV$ per decade according to $\Delta E = 2\gamma_{opt}$ [Sie06], which is slightly smaller than the directly measured red-shift of the peak.

When the peak position of the E_1-emission is determined for a wider range of beam currents, the energy is observed to saturate for high beam currents as shown in Figure 5.13(b). A saturation value of $0.994\pm0.002\ eV$ is obtained by a fitting procedure, which is interpreted as the unperturbed E_{DA1}-energy. This corresponds to a red-shift of $\Delta E(I_b) = E_{1,sat} - E_{1,I_b}$ with $\Delta E(0.5\ nA) = 21\pm3\ meV$ as already used in Section 5.2.4.

5.4 Photoluminescence of Ga-graded Cu(In,Ga)Se$_2$

All effects described in the previous sections were obtained by CL analysis of Ga-graded Cu(In,Ga)Se$_2$ thin-films and shall now be compared to PL measurements with an unfocused laser beam (macro-PL). Principal differences between these methods regarding the excitation mechanism are discussed, before presenting and comparing selected results. All PL measurements were performed at the Technische Universität Ilmenau, Germany, in collaboration with the group of Profs. G. Gobsch and R. Goldhahn.

5.4.1   Differences in the excitation mechanisms of PL and CL

Several differences in the excitation mechanism between CL and PL shall be shortly discussed here:

(1) In PL, only one e-h-pair can be created by the absorption of one incident photon – in contrast to about 1000 e-h-pairs excited per incident electron in CL.

(2) The overall number N_{ph} of incident photons per lifetime τ_e can be calculated to be around $N_{ph} = 10^9$ for the standard parameters (see Section 3.2.8) compared to $N_e = 15$ in CL.

(3) The excitation occurs laterally homogeneous over an area, which is large compared to the sample thickness and transport distances when measured in macro-PL mode. Thus, the signal gives a good estimate for average values. However, laterally resolved measurements, for example in cross-section configuration, are not possible.

(4) The excitation depth profile follows the Beer-Lambert law for absorption with the absorption coefficient $\alpha(E_v)$. In band-gap graded material, the absorption coefficient additionally varies with sample depth z.

The generation rate per volume (hereafter: generation rate density) has been calculated for the measured grading [see Figure 5.1(b)] in front and back configuration by implementing the profile into SCAPS-1D 2.9 [Bur08] (see Section 5.5.1). The generation-rate density and the injection density are displayed in Figure 5.14(a) as a function of depth for both configurations as calculated using the standard parameters (see Section 3.2.8) and a lifetime of $\tau_e = 10\ ns$. A photon energy of $E_v = 1.7\ eV$ was chosen to obtain an absorption depth of about 300 nm in both geometries, which roughly corresponds to the excitation depth in CL at 10 keV.

In order to compare the injection densities of PL and CL measurements, the normalized summed injection $R(\Delta n)$ is calculated as a function of the injection density Δn as described by Eq. (2.7) and plotted for both configurations in Figure 5.14(b). Mean values of $\Delta n_m = 1.8\ 10^{15}\ cm^{-3}$ and $1.3\ 10^{15}\ cm^{-3}$ are obtained in front and back geometry, respectively. For homogeneous absorber material, the mean injection density can also be calculated analytically to

$$\Delta n_m = \frac{\alpha(E_v)\ P\ \tau}{2\ A_{ill}\ E_v} \tag{5.6}$$

(with the laser power P per area A_{ill}). The width of the distribution of the injection density $w_{\Delta n}$ (see Section 2.3.1) is around 5 as can be seen in Figure 5.14(b); thus, it is a factor of ten lower compared to typical CL conditions.
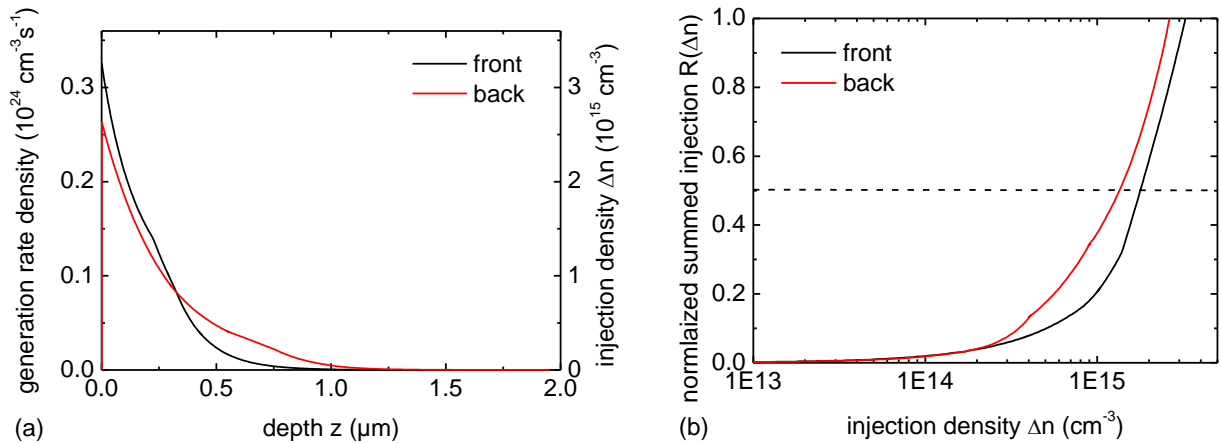
Figure 5.14: (a) Generation-rate density as a function of depth for a photon energy of $E_\nu = 1.7\ eV$ and a power density of the exciting laser of $20\ mW\,mm^{-2}$ in both front and back configuration; the corresponding injection density axis is displayed on the right for a minority carrier lifetime of $10\ ns$. (b) The normalized summed injection as a function of the injection density calculated according to Eq. (2.7) for both configurations.

5.4.2 Comparing PL and CL spectra of Ga-graded Cu(In,Ga)Se$_2$

The standard front and back side spectra are displayed in Figure 5.15(a). As shown for CL in Figure 5.2(a), more than just one emission is found in both configurations, with the maximum and minimum energies in each case being related to the near-surface and the minimum band-gap energies, respectively. For convenience, the three peaks were named with the same symbols E_1, E_2 and E_3 used in Figure 5.2(a). Altogether, the spectra look similar to those obtained by CL; some differences appear (peak intensity ratio, reduced peak width, additional shoulder at around $1.02\ eV$, no deep-level emission), which may be related to the principle differences in excitation, but also due to differences in the experimental set-ups in Jena and Ilmenau. The experimental spectra can be compared to hypothetical spectra in Figure 5.15(b) calculated on the basis of Eq. (5.5) and excitation depth profiles from Figure 5.14(a) as also done for CL in Section 5.3.1. It is observed, in agreement with the CL data, that the peak ratios IR_{front} and IR_{back} are strongly enhanced in the experiment.
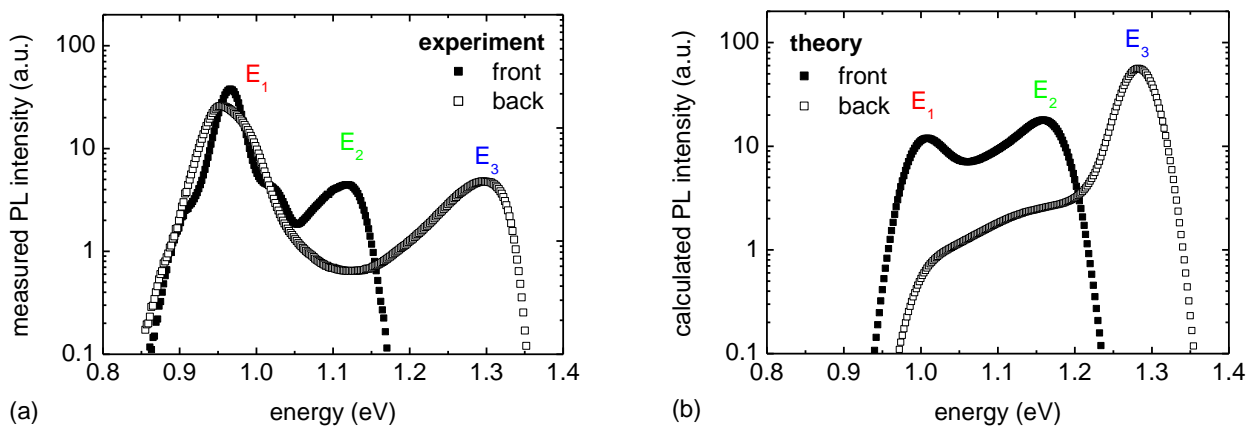
Figure 5.15: (a) PL spectra measured under the standard conditions in both front and back configuration showing the three emissions labeled E_1, E_2 and E_3 in CL analysis. (b) Hypothetical PL spectra calculated from the generation-rate depth profiles in Figure 5.14(a) using Eq.(5.5).
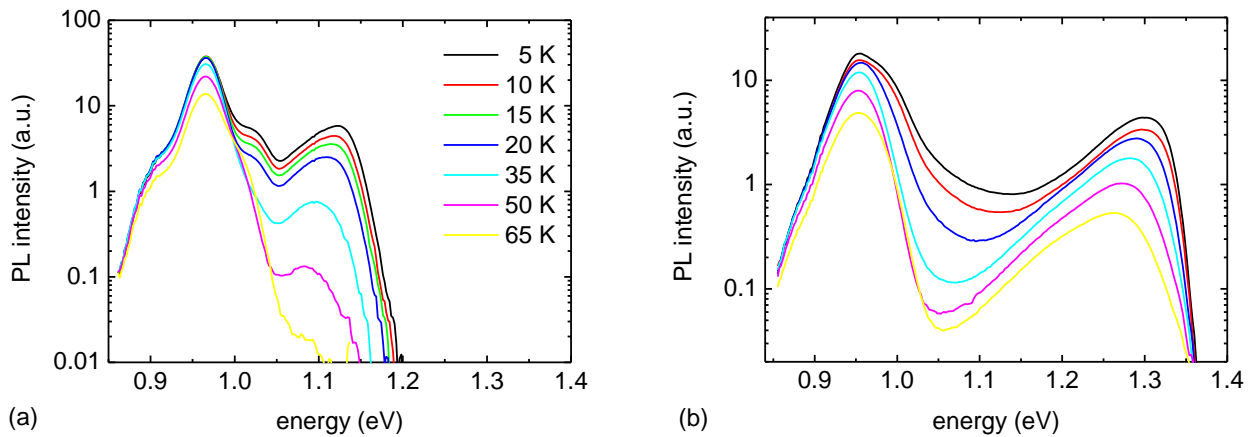
Figure 5.16: Temperature-dependent PL-spectra in both front and back configuration for temperatures ranging from 5 to 65 K. The legend applies to both parts of the figure.
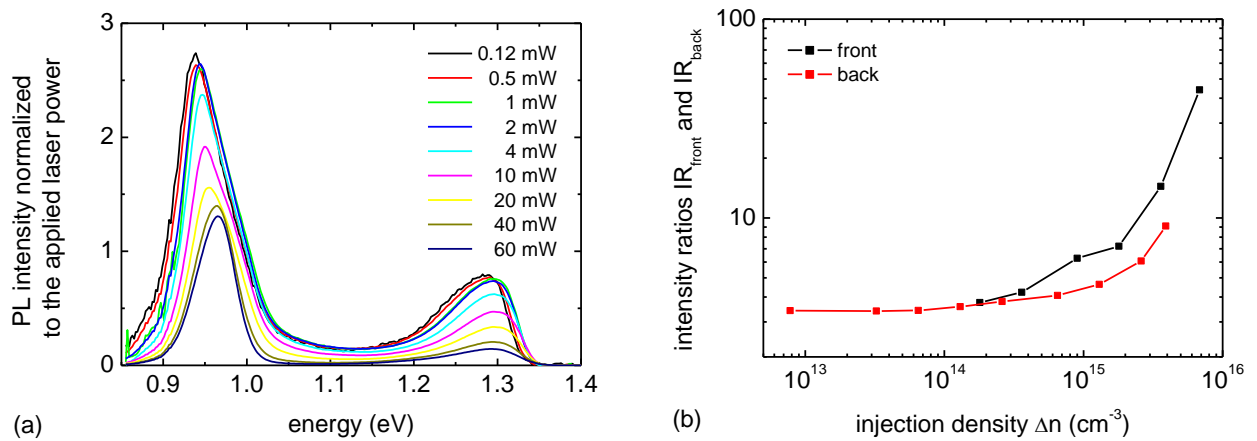
Figure 5.17: (a) Power-dependent PL-spectra in back configuration normalized to the applied excitation power. (b) Intensity ratio IR_{front} and IR_{back} as a function of the injection density Δn.

Temperature-dependent PL measurements are shown in Figure 5.16(a) for front geometry and temperatures from 5 to 65 K. The intensity ratio IR_{front} strongly decreases at higher temperatures until the emission at E_2 is below the detection limit at 65 K. This qualitatively agrees with the observations from CL measurement. A decrease of IR_{back} with temperature is also observed in PL measurements in back geometry in Figure 5.16(b), but it is much less pronounced.

Power-dependent PL data in back geometry are shown in Figure 5.17(a) and normalized to the applied excitation power. These normalized PL spectra are constant for low excitation power, but the intensity of both peaks decrease if the power is above 1 mW. This decrease of the normalized CL spectra is equivalent to a power exponent of $k < 1$ in this region. Furthermore, the intensity ratio IR_{back} changes with excitation power. In Figure 5.17(b), the intensity ratios IR_{front} and IR_{back} are plotted as a function of the injection density Δn. Both ratios strongly increase for high power, but are found to saturate for injection densities below 10^{14} cm^{-3}. If the intensity ratio and the normalized PL intensity are constant, the transport and recombination properties (mobility, lifetime, radiative recombination efficiency) can be concluded to be independent of the excitation conditions – they are

not influenced by the measurement itself. Hence, low-injection conditions are presumed to be fulfilled in this region − in turn, it is concluded that high-injection conditions are present for higher excitation power and definitely also for the CL analysis. The low-injection limit of 10^{14} cm^{-3} can be carefully taken as an approximation of the effective doping density at 10 K according to Eq. (2.9), but the injection density must be remembered to be influenced by the lifetime assumed in the calculation. Furthermore it may be reduced due to charge carrier transport as discussed in Section 2.3.2.

The amplitude of the optical fluctuations γ_{opt} is measured as described in Section 5.3.3 for each power and plotted (together with the CL data) as a function of the injection density Δn in Figure 5.18. The decrease of the amplitude γ_{opt} with injection is in very good agreement between both methods.
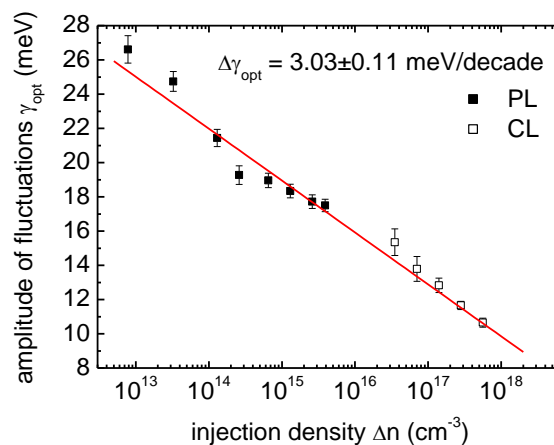
Figure 5.18: Average amplitude of potential fluctuations γ_{opt} determined by both PL and CL measurements as a function of the injection density Δn.

5.5 Simulation of charge carrier transport in the quasi-electric field

Several observations in plan-view CL and PL in Sections 5.3 and 5.4 have been qualitatively explained with the charge carrier drift in the quasi-electric field. A more quantitative description of the drift processes is performed in this section by numerical as well as analytical simulations based on the transport equations described in Section 2.3.2. Again, the SIMS-measured profile is used as a reference and implemented into the simulations.

5.5.1 Numerical simulations with SCAPS-1D

The latest versions of SCAPS-1D (from SCAPS-1D 2.8 and after) [Bur00; Bur08] offer the possibility to introduce a grading within the layers, which allows to reproduce the experimental band-gap grading in the simulation. The layer structure used for this purpose is displayed in Figure 5.19: The Cu(In,Ga)Se$_2$-layer is split up in six parts, each of it exhibiting parabolic grading shape,

and an additional thin "vacuum-layer" (with minimum mobilities and density of states in both bands) is introduced to prevent the current flow towards the left contact. The configuration corresponds to exciting the backside free surface in CL analysis. Flat band conditions are chosen for both contacts. All material parameters of the Cu(In,Ga)Se$_2$-layers are adopted from the baseline case described in the PhD-thesis of Markus Gloeckler [Glo05a] (the full parameter set is given in the Appendix Table A1) – with the following exceptions: the layer thickness is reduced to the experimental value of 2 μm, the band-gap and the electron affinity are chosen to fit the SIMS-measured band-gap grading [see Figure 5.1(b)] and the donor-defect density is reduced to 2 10^{13} cm^{-3} in order to obtain an electron lifetime τ_e of 10 ns as assumed in all previous calculations. The band-structure obtained is shown in Figure 5.20(a) (conduction and valence band) and compared to the SIMS-measured band-gap profile (dotted line); an excellent agreement can be found.

Additionally, Figure 5.20(a) displays the quasi-Fermi levels E_{Fn} and E_{Fp} for excitation with an electron beam of an electron energy of $E_e = 10$ keV at room-temperature. The generation depth profile $g(z) \sim \varepsilon(z)$ [see Figure 2.2(b)] is introduced into the simulation from an external file; as the simulation is one-dimensional, the lateral distributions, thus, the injection profile and density, cannot be properly represented. The excitation intensity is adjusted to maintain low-injection conditions. The electron quasi-Fermi level is found to follow the shape of the conduction band in the excitation region; thus, Eq. (2.17) is confirmed to be valid in low-injection conditions. The generation- and recombination-rate densities for the given situation are displayed in Figure 5.20(b). While the generation takes place solely in the first 500 nm near the back-contact, the recombination occurs mainly in the region of the minimum band-gap at 1 - 1.5 μm below the surface. Thus, the charge carrier drift towards the band-gap minimum can also be described by SCAPS-simulations.

layer name	thickness (nm)	GGI from…to…
left contact	-	-
vacuum	1	-
Cu(In,Ga)Se$_2$ 1	300	0.54
Cu(In,Ga)Se$_2$ 2	260	0.54 – 0.45
Cu(In,Ga)Se$_2$ 3	570	0.45 – 0.095
Cu(In,Ga)Se$_2$ 4	420	0.095 – 0.08
Cu(In,Ga)Se$_2$ 5	150	0.08 – 0.175
Cu(In,Ga)Se$_2$ 6	300	0.175 – 0.39
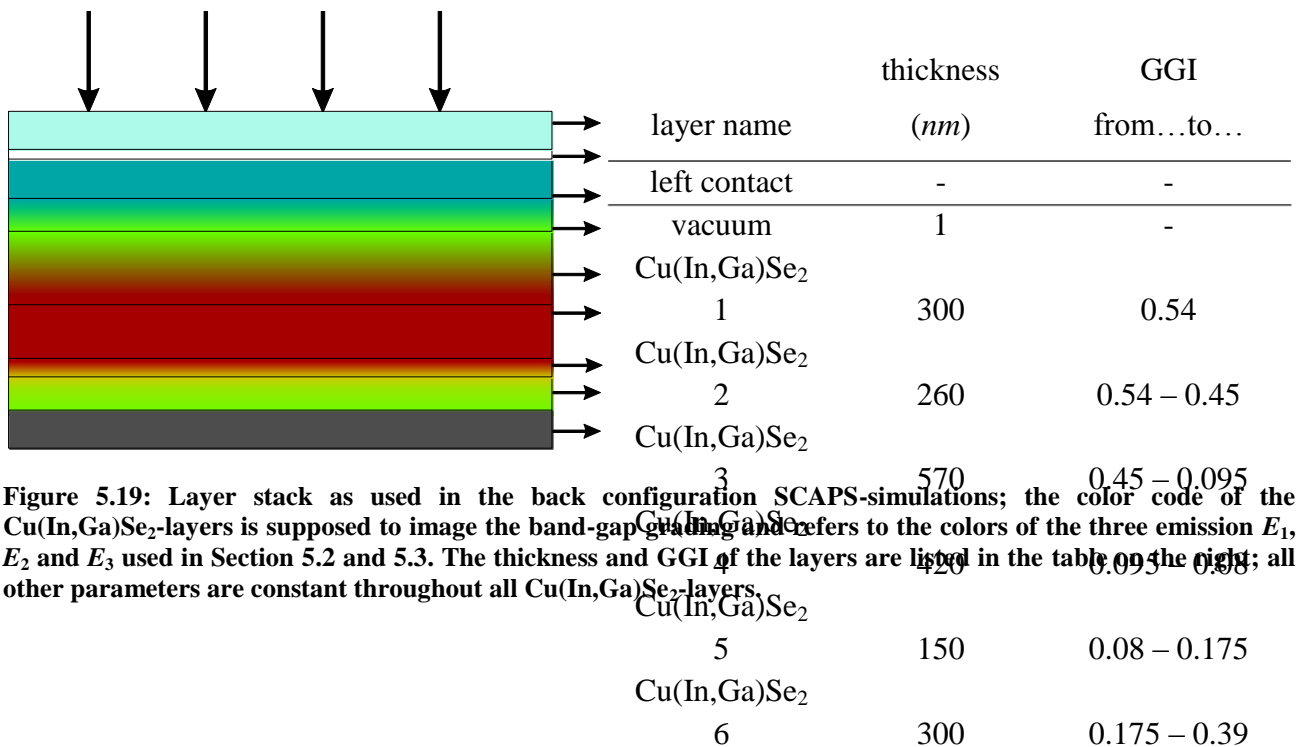
Figure 5.19: Layer stack as used in the back configuration SCAPS-simulations; the color code of the Cu(In,Ga)Se$_2$-layers is supposed to image the band-gap grading and refers to the colors of the three emission E_1, E_2 and E_3 used in Section 5.2 and 5.3. The thickness and GGI of the layers are listed in the table on the right; all other parameters are constant throughout all Cu(In,Ga)Se$_2$-layers.
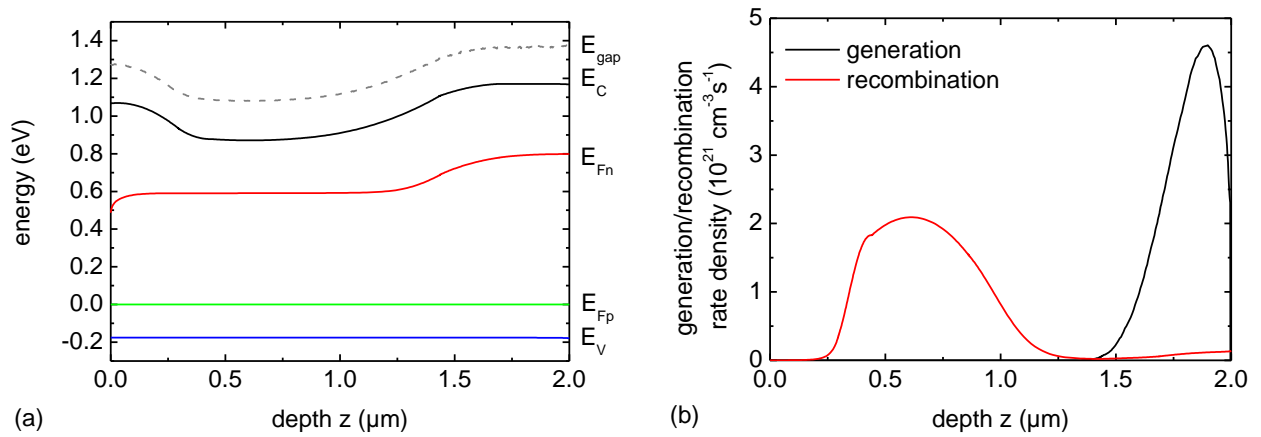
Figure 5.20: (a) Band diagram of the Cu(In,Ga)Se₂ layer obtained from SCAPS simulation for the layer stack shown in Figure 5.18 and for an excitation depth profile corresponding to the one of an electron beam with an electron energy of 10 *keV* from the back and just holding low-injection conditions; the band-gap calculated from SIMS data is added as a dashed line to show the similarity to the simulated band-gap profile. (b) Generation- and recombination-rate depth profiles obtained from this simulation.
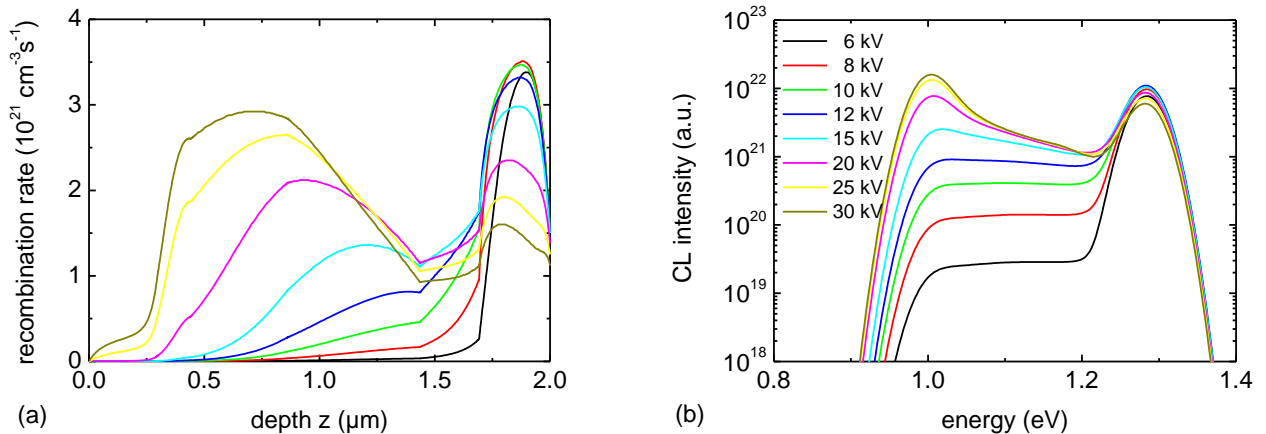

Figure 5.21: (a) Recombination depth profiles obtained from SCAPS simulations for different electron energies E_e of the electron beam (legend see part b of this figure); (b) CL spectra calculated from these recombination depth profiles using Eq.(5.5).

Voltage-dependent excitation can also be described by these simulations by using different generation depth profiles. Moreover the $\mu\tau$-product is adjusted to $5\ 10^{-9}\ cm^2\ V^{-1}$ as obtained in Section 5.2.2. Because the simulation does not run at temperatures as low as 10 *K*, it needs to be performed at room-temperature. The recombination depth profiles are shown in Figure 5.21(a) as obtained from the simulations for voltages from 6 to 30 *kV*. The kinks in the curves occur in the interface regions between two layers due to an imperfect parameterization of the band-gap grading. CL spectra can be calculated from these profiles using Eq.(5.5), if the energy depth profile is replaced by the simulated recombination depth profile in the equation; the results are plotted in Figure 5.21(b). In agreement with the experimental results shown in Figure 5.10(b), an increase of the E_1-emission of about three order of magnitude is observed, while the influence on the intensity of the E_3-emission is only weak, showing a maximum at around 10 - 15 *kV*. Although the spectra

thus show a similar voltage dependence, the intensity ratio IR_{back} is a factor of around 100 lower than in the experiment

5.5.2 Analytical description of the drift process

The drift process can also be described by analytical expressions, which is exemplarily shown in this section for the back configuration. All calculations were performed with Maple 9.5.

For the calculations, an analytical expression has to be defined to describe the shape of the band-gap grading. In this work, the grading is parameterized by a step-like function to

$$E_{gap}(z) = A_2 + \frac{A_1 - A_2}{1 + exp\left(\frac{z - z_0}{dz}\right)}. \tag{5.7}$$

Because the expression for the quasi-electric field E_{qe} needs to be applicable for the analytical integration of Eq. (5.9), the band-gap increase towards the front-contact has to be neglected. The fit and the corresponding fit parameters of the back grading are displayed in Figure 5.22(a). The quasi-electric field $E_{qe}(z)$ is calculated according to Eq. (2.17) and used to determine the drift velocity $v_{drift}(z)$ from Eq. (2.18). Therefore, it is assumed that the drift velocity is able to immediately follow the change in the quasi-electric field. This is the case, if the maximum effective acceleration $a_{eff,max}$

$$a_{eff,max} = \mu_e \left(\frac{dE_{qe}}{dt}\right)_{max} = \mu_e \left(\frac{dE_{qe}}{dz} v_{drift}\right)_{max} = \mu_e^2 \left(\frac{dE_{qe}}{dz} E_{qe}\right)_{max} \tag{5.8}$$

is small compared to the free ballistic acceleration $a_{ballistic}$ in the quasi-electric field E_{qe}: $a_{ballistic} = e\, E_{qe}/m_e^*$ with the effective electron mass $m_e^* = 0.09\, m_e$ [Neu86]. In the present case, $a_{eff,max}$ is found to be $7.5\, 10^{13}\, m\, s^{-2}$, where as the ballistic acceleration is about $10^{18}\, m\, s^{-2}$; thus the relation is fulfilled. An equivalent formulation would be that the average collision time τ_s for intraband scattering (which is in the order of $10^{-15}\, s$ for materials with a large number of localized states [Fon81]) is small compared to the time scale of the drift process.

Hence, the drift time t_{drift} from the depth of excitation z_0 to a depth z can be calculated to

$$t_{drift}(z, z_0) = \int_{z_0}^{z} \frac{1}{\mu_e E_{qe}(z)}\, dz. \tag{5.9}$$

The drift time t_{drift} is plotted as a function of the depth z for excitation at the surface ($z_0 = 0$) and an electron mobility μ_e of $100\, cm^2\, V^{-1}\, s^{-1}$ in Figure 5.22(b) (black line). In this figure, it is beautifully visualized, how the residence time of carriers in the region of the maximum drift field is strongly reduced. The recombination depth profile $R(z,0)$, which is also shown in Figure 5.22(b) (red line) for a lifetime of $\tau_e = 10\, ns$ is calculated using
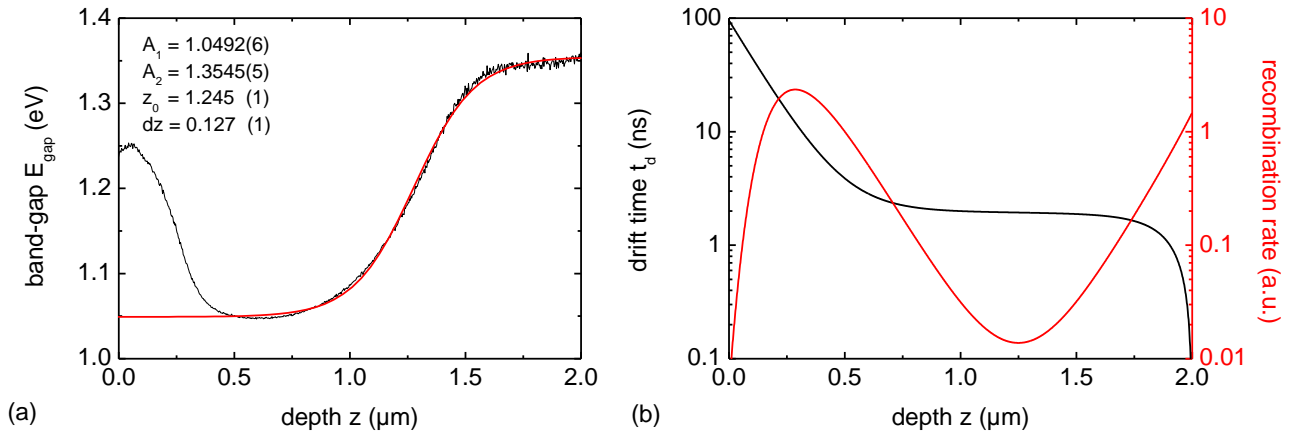
Figure 5.22: (a) Fit to the band-gap profile calculated from SIMS measurements according to Eq.(5.7), showing the corresponding fit parameters in the inset. (b) Drift time $t_{drift}(z,0)$ and recombination rate $R(z,0)$ for carrier excitation directly at the surface.

$$R(z,z_0) = \begin{cases} 0 \, , & z < z_0 \\ \dfrac{d}{dz}\left[1 - exp\left(\dfrac{t_d(z,z_0)}{\tau_e}\right)\right], & z \geq z_0 \, . \end{cases} \qquad (5.10)$$

The recombination depth profile $R(z,0)$ exhibits two main regions of recombination: near the surface (within the first two nanoseconds) and at a depth of more than $1\,\mu m$, thus, near the band-gap minimum. The drift process can be found from Eq. (5.10) to be fully determined by the quasi-electric field $E_{qe}(z)$ and the product of μ_e and τ_e; thus, these two parameters can principally not be determined independently by investigating the CL of band-gap graded material. The influence of the excitation profile $g(z_0)$ at the electron energy E_e can be accounted for by a weighting integral

$$R_{E_e}(z) = \int_0^\infty g_{E_e}(z_0) \, R(z,z_0) \, dz_0 \, , \qquad (5.11)$$

which can only be solved numerically. This way, also voltage-dependent CL can be investigated by this method. The calculations according to Eqns. (5.9) - (5.11) have been performed for the above band-gap grading and $\mu\tau = 5 \ 10^{-9} \ cm^2 \ V^{-1}$ in order to compare it to the results obtained from SCAPS. Again, Eq. (5.5) is used to calculate the corresponding CL spectra plotted in Figure 5.23(a) for voltages from 6 to 30 kV. The spectra are very much comparable to what is shown from the SCAPS-simulations in Figure 5.21(b) concerning the absolute values as well as the voltage dependence of the intensity ratio IR_{back}. The results from both simulations and the experimental values for the intensity ratio IR_{back} are summarized in Figure 5.23(b) by plotting it as a function of the electron energy E_e. Note that the scaling for the experimental values (right scale) differs by a factor of 100 from the scaling for the simulated values.
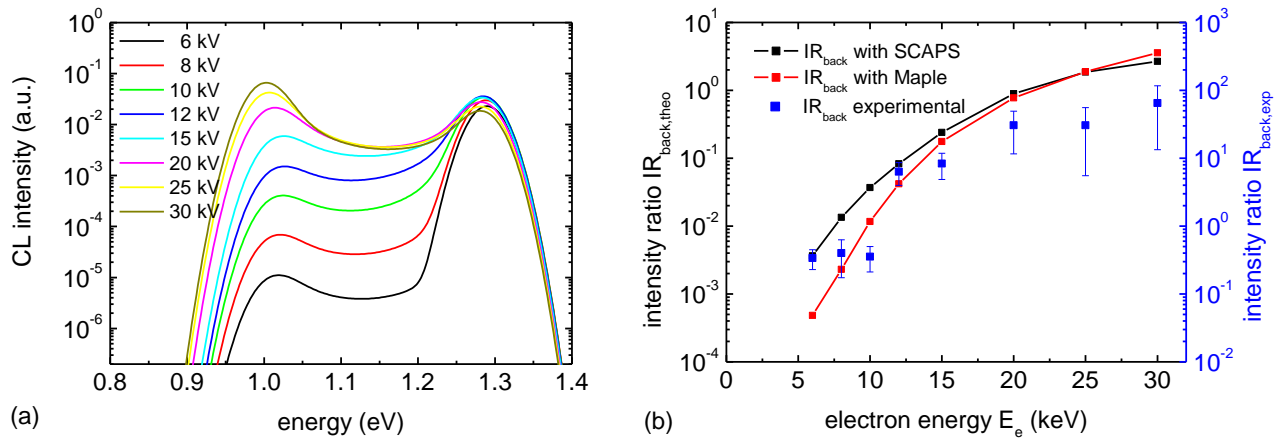
Figure 5.23: (a) Voltage-dependent CL-spectra calculated from the recombination depth profiles obtained using Eq. (5.11); (b) Intensity ratio IR_{back} as a function of electron energy E_e as measured in CL and compared to the ratios obtained from the simulations with SCAPS and Maple.

The drift process can be shown to be very sensitive to the shape of the quasi-electric field: Although the differences between the SIMS-, EDS- and CL-measured profiles are rather small [see Figure 5.1(a) and Figure 5.8(b)], the intensity ratio IR_{back} is about a factor of 10 higher for the field obtained from the TEM-EDS-data and even a factor of 100 higher for the field from the CL-measured band-gap grading in Maple calculations when compared to the results shown in Figure 5.23(b). Thus, the large discrepancy in the absolute intensity ratios may be explained by deviations of the quasi-electric field present in the sample from the shape obtained from the SIMS-measured Ga-profile. Moreover, high-injection effects are not at all considered in the simulations.

5.6 Laterally resolved luminescence of Ga-graded Cu(In,Ga)Se$_2$

All CL and PL spectra detected in plan-view configuration and shown in Sections 5.3 and 5.4 are obtained by averaging over an area, which is large compared to the grain size of the Cu(In,Ga)Se$_2$ layer. In fact, the grain structure can easily be resolved in CL imaging.

In Figure 5.24(a), a secondary electron (SE) image of an area of about 100 μm^2 is shown. The grain structure can be clearly resolved with grain sizes ranging from 100 nm to about 2 μm. The monochromatic CL image at the energy E_1 is collected simultaneously with the SE image and displayed in Figure 5.24(b). The lateral distribution of the CL intensity varies by about a factor of three and exhibits features that can be clearly associated with the grains when comparing the structure to the grain structure in the SE image. The intensity is observed to be reduced at grain boundaries, which is observed for all luminescence energies as well as in polychromatic mode (not shown) and is commonly interpreted as an increase of the non-radiative recombination at grain boundaries [Rom03a; Ott04]. In addition, differences in intensity are also observed between individual grains (light and dark areas).
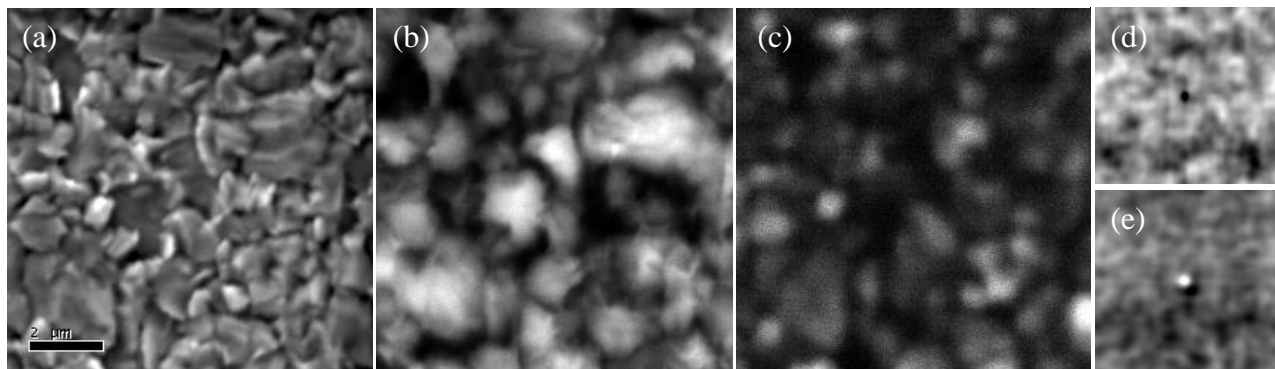
Figure 5.24: Secondary electron (SE) image (a) of the front surface of the Cu(In,Ga)Se$_2$ layer with the monochromatic CL image at the energy $E_1 = 0.97\ eV$ (b) and $E_2 = 1.13\ eV$ (c). The structure of SE and CL images were compared by cross-correlation imaging, which is displayed for the energies E_1 and E_2 in (d) and (e), respectively.

The lateral structures of the SE and the CL image is analyzed by calculating the cross-correlation images, which is a standard technique in 1D- and 2D-signal processing [Tra88; Oph91]. The cross-correlation image shows a negative correlation of -0.22 of the intensities of the SE and the CL image as shown in Figure 5.24(d) (dark spot in the middle), which means that darker areas in the SE image tend to show higher luminescence intensity. Since in the SE image, which contains mainly topological information, steep surfaces and edges tend to be brighter than flat surfaces, the CL intensity at E_1 is found to be higher at flat areas compared to regions with sharp grain shapes.

A CL image at the emission energy E_2 detected at the identical position is displayed in Figure 5.24(c). The CL intensity is generally lower at this energy, but the lateral variation is strongly enhanced to more than a factor of 100 – the dark regions partly represent areas with a luminescence signal below the detection level. The regions of increased CL intensity are smaller in size compared to those at the energy E_1 [see Figure 5.24(b)], but can again be correlated to the grain structure observed in the SE image. In this case, a positive correlation of +0.32 of the two images is found in the cross-correlation image plotted in Figure 5.24(e) (light spot in the middle); hence, the CL intensity at E_2 is relatively high at edges and steep and elevated parts of the surface. Therefore, it can be concluded that different lateral regions equivalent to different grains at the surface, contribute to the CL intensity at E_1 and E_2.

Both monochromatic CL images can also be superimposed as a color composite, as shown in Figure 5.25(b). Here, it is observed how the CL images complement each other: the sample surface is split into "red grains" and "green grains", which hardly overlap (no "yellow grains"). Strictly speaking, this image displays the lateral distribution of intensity ratio IR_{front} normalized to an arbitrary value by the contrast-brightness adjustment. The intensity ratio IR_{front} varies between a minimum value of 10^1 at small, elevated grains and maximum values of above 10^3 at large, deeper-lying grains. In accordance with the observations of Romero et al. [Rom03b], this may be tentatively interpreted to

point towards the existence of a sub-interface at those smaller grains, which hinders excited carriers to proceed on their way towards the minimum band-gap.
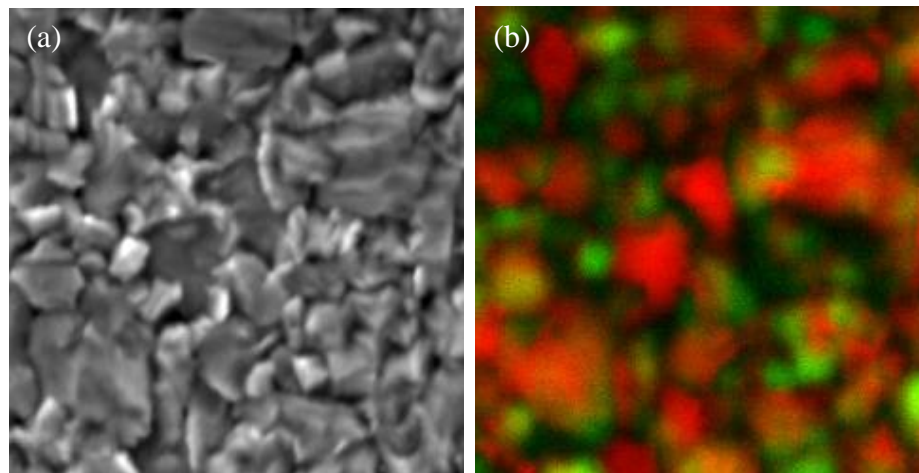

Figure 5.25: (b) Color composite of the two monochromatic CL images at the two peak energies E_2 (green) and E_1 (red) as shown in Figure 5.24(c) and Figure 5.24(b), respectively. The slight shift in position between those two images was corrected by determining the shift between the corresponding SE images (a), using their cross-correlation.

Summary

- The Ga-grading in Cu-poor Cu(In,Ga)Se$_2$ layers is shown to strongly influence its luminescence properties; several qDAP-emissions can be observed in graded films, which can be related to regions of different Ga-content as beautifully visualized in cross-section measurements. In standard front-configuration, the main emission corresponds to the minimum band-gap energy in the layer. [Section 5.1]

- Direct evidence is given for significant drift of excited charge carriers towards the minimum of the band-gap. The results are consistent with a drift through forces induced by the vertical grading in electron affinity in the layer, which is commonly referred to as quasi-electric field. The drift process can be characterized by a charge carrier drift length, which also allows to determine the minority carrier mobility. [Section 5.2]

- A model is developed to describe the influence of the grading on the luminescence signal obtained from the sample, which is also implemented into SCAPS-simulations and analytically described. Monochromatic CL imaging on a cross-section sample is shown to be capable to measure the in-depth band-gap profile. [Sections 5.2 + 5.5]

- The influence of the grading on plan-view CL and PL is investigated in detail. Both PL and CL spectra can be explained only if drift of charge carriers is taken into account. The relative peak intensity in the luminescence spectra is shown to depend strongly on the excitation conditions. In the light of these data and the interpretation presented here the results of recent

work on the plan-view luminescence of graded Cu(In,Ga)Se$_2$ [Ish09; Slo10; Paw11; Zac11] may have to be reconsidered. [Sections 5.3 + 5.4]

- Low-injection conditions are presumed to be present for the lowest PL excitation powers only. All other measurements are performed in the high-injection regime in agreement with the considerations in Section 2.3.1. The high-injection conditions are presumed to strongly influence the drift process. [Sections 5.2, 5.3 + 5.4]

- The lateral distribution of the CL intensity is shown to be strongly influenced by the grain structure and shows considerable variations for different detection energies. [Section 5.6]

6 Characterization of Cu(In,Ga)Se$_2$ absorbers deposited at higher substrate temperature

As described in Chapter 2, high-efficiency Cu(In,Ga)Se$_2$ absorbers are fabricated by a three-stage process at the HZB and exhibit a double-grading of the Ga-content. It is investigated, if an increased substrate temperature has an influence on the shape of the Ga-grading (Section 6.1) as well as the crystal structure (Section 6.3). This may also have an impact on the performance of device made from these absorbers (Section 6.4). The model of the luminescence of graded Cu(In,Ga)Se$_2$ developed in Chapter 5 is applied to investigate the differences in the vertical (grading) as well as lateral homogeneity (Section 6.2). Parts of the results presented in this chapter have been published in [Win09; Haa11a].

6.1 Ga-grading of Cu(In,Ga)Se$_2$ deposited at different temperatures

Figure 6.1(a) shows the Ga-grading how it was measured by the use of SIMS on absorbers deposited at a temperature of 610°C (high temperature – HT) and 530°C (low temperature – LT), respectively. It can be seen that the LT sample exhibits a strong double-grading as it has been discussed in the previous section (GGI between 10 and 55%). The same shape of grading is also found in the HT absorber, but the variation of the GGI is strongly decreased (22 - 40%) compared to the LT sample. A reduction of the Ga-grading with increasing temperature is also observed in the low-temperature regime (300 - 550°C) [Kes04; Rud05; Ish08; Kau09]. The reduced phase separation may be due to a higher In-Ga-interdiffusion [Kau09] and/or the intermixing may become thermodynamically favored [Lud10] at higher temperatures. Very similar profiles are measured by means of TEM-EDS as also plotted in Figure 6.1(a); thus, the flattening of the grading is shown not to be due to the lateral averaging of the SIMS technique, but to a real enhanced intermixing on the local level inside single grains.

While all techniques applied for the determination of the Ga-grading are only sensitive to the elemental distribution within the layer, XRD measures the crystallographic structure. Thus, it gives the additional information if a real alloying of the CuInSe$_2$ and CuGaSe$_2$ phases is established in the absorber layer. The (112)-reflection of the chalcopyrite phase is shown for both HT and LT samples in Figure 6.1(b). The diffraction patterns were fitted and the peak positions were correlated with the GGI according to literature data [Bal08]. The FWHM of the peaks (see Table 6.1) is by far larger than expected for a grain size of a few hundred nanometers according to the Scherrer-equation

[Sch18]. Therefore, the FWHM is interpreted to be due to the inhomogeneous Ga-distribution, thus, it determines the spreading of the GGI as measured with this technique. The data extracted from Figure 6.1(b) are listed in Table 6.1.

High-temperature (HT) samples show one single reflection at 26.98° corresponding to a GGI of around 30±8% indicating a high degree of homogeneity of the vertical Ga-distribution. LT samples exhibit a three peak structure with reflections at 26.74°, 26.97° and 27.28°, corresponding to regions with a GGI of 7±7%, 29±13% and 58±7%. The gallium in-depth distribution cannot be determined from this XRD measurement, but the profiles in Figure 6.1(a) allow to assign the reflections to the front (GGI = 29%), medium (GGI = 7%) and back (GGI = 58%) region of the absorber.

Note that the small peak at around 27.8° in the pattern of the LT sample corresponds to the (103)-reflection of the low-gallium-region. In conclusion, an increase in the intermixing of the elements as well as in the alloying of the quaternary phase is found at higher substrate temperatures.
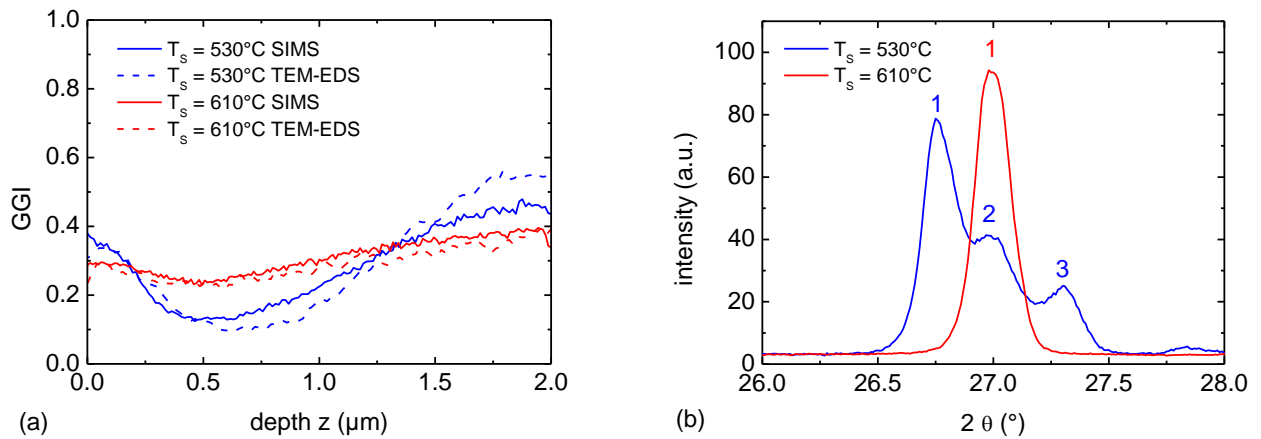
Figure 6.1: (a) Profile of the GGI as measured by SIMS and TEM-EDS for both types of absorbers. (b) Diffraction patterns of both samples showing the (112)-reflection of the chalcopyrite structure.

Peak/Sample	Peak Position 2θ (°)	FWHM (°)	GGI (%)
LT1	26.743 ± 0.004	0.128 ± 0.001	7.4 ± 6.2
LT2	26.969 ± 0.010	0.278 ± 0.011	29.2 ± 13.3
LT3	27.282 ± 0.012	0.142 ± 0.013	58.4 ± 6.6
HT1	26.978 ± 0.001	0.157 ± 0.001	30.0 ± 7.6

Table 6.1: Peak position and width of all four peaks marked in Figure 6.1(b); the GGI is calculated from the peak positions according to [Bal08], whereas the distribution width of the GGI is determined from the peak width.

It has been found that Cu(In,Ga)Se$_2$ absorber layers in record efficiency cells exhibit preferred (220)/(204)-orientation of the grains, which has been shown to develop if higher substrate temperatures and Se-rates are used during the absorber deposition process [Con06]. Therefore, it is worth noticing that for all investigated absorbers, the ratio of the absolute intensities of the (112)- and the (220)/(204)-reflections is between one and three, which means that the layers show only a

very weak texture. The (220)/(204)-texture seems to be slightly higher for the HT samples, but pronounced (112)- and (220)/(204)-textures, as described in [Con06], cannot be found here.

6.2 Cathodoluminescence of Cu(In,Ga)Se$_2$ deposited at different temperatures

The decreased Ga-grading measured in Section 6.1 leads to a reduced variation of the CL emission energy with depth according to Chapter 5. For a minimum GGI of 0.22 and a maximum of 0.4, the DA1-emission energy is calculated to 1.11 and 1.22 eV, respectively [see Figure 2.10(b)]. Typical normalized CL-spectra of both kinds of absorbers are shown in Figure 6.2(a) as they were detected in front configuration. For both deposition temperatures two spectra are exemplarily shown, which were detected at different points of the sample in order to demonstrate the homogeneity of the samples on the *mm*-scale. In both cases, the spectrum is dominated by one broad emission due to qDAP-transitions. While the shape of the spectra is similar, the energy of the emission line is considerably higher for the HT absorber when compared to the LT absorber. The emission of the HT absorber at 1.12 eV can be assigned to the DA1-transition of Cu(In,Ga)Se$_2$ with a GGI of approximately 20-25% [see Figure 2.10(b)], which agrees with the minimum GGI measured by SIMS (see Figure 6.1). Moreover, no DL-emission is detected for HT samples. The luminescence of standard (LT) samples has been discussed in detail in Chapter 5.

An increase of the substrate temperature has already been described to lead to a blue-shift of the CL peak-energy and to a change from (112)- to (220)/(204)-textured films [Ott04]. Therein, the blue-shift is attributed to a "shift of the average band-gap" [Ott04] due to the re-texturing. An increased lateral homogeneity in the CL emission energy is found for (220)/(204)-oriented films [Con06]. In both studies, no information is given on the substrate temperatures during growth or on the shape of the Ga-grading present in the layer.

(a)

(b)
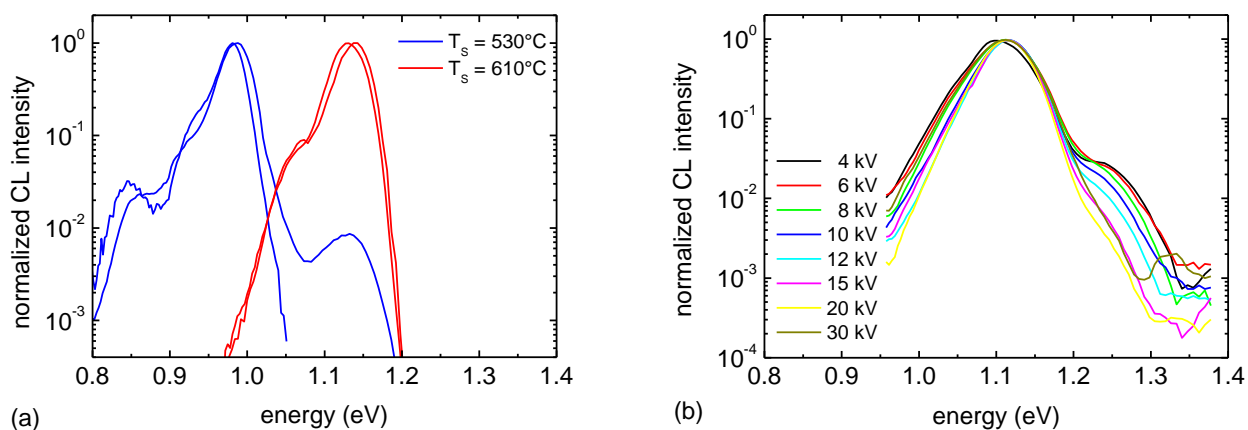
Figure 6.2: (a) Normalized CL spectra of both LT and HT absorbers from the front. (b) Voltage-dependent CL spectra measured in back configuration at HT absorbers.

In this work, the difference in emission energy shown in Figure 6.2(a) is interpreted to be due to the change in the Ga-grading. According to the charge carrier drift model in Section 5.2.2, the emission energy detected from a sample with band-gap grading is determined by the minimum band-gap $E_{gap,min}$ within the layer, if the drift-length L_{Drift} is sufficiently large. This can be found when comparing the CL emission energies of both samples to the minimum Ga-contents shown in Figure 6.1(a) and Table 6.1. Thus, the differences in the Ga-grading described in the previous section finds its counterpart in luminescence spectroscopy. Vice versa, it is possible to measure the band-gap minimum $E_{gap,min}$ by means of CL.

Voltage-dependent measurements on the HT sample were performed from the back and are displayed in Figure 6.2(b) as normalized to the peak maximum. No significant changes in the emission energy can be detected for electron energies ranging from 4 to 30 keV. Note that the emission energy (1.11±0.01 eV) is comparable to the one measured in front configuration as predicted if the emission occurs mainly at the band-gap minimum in double-graded absorbers. For low electron energies a shoulder appears at higher energies. The energy of this peak is determined to be about 1.24±0.01 eV corresponding to a GGI of 43%. Since the intensity ratio IR_{back} is found to be very large (> 40) also in this sample for all electron energies, a strong drift towards $E_{gap,min}$ must be present in the layer although the quasi-electric field is considerably weaker compared to LT samples (about 30% only). The drift length is measured to 600±100 nm by cross-section measurements as described for LT samples in Section 5.2. According to Eq. (2.18), this enlarged drift length can only be explained by an increase of the electron mobility μ_e and/or lifetime τ_e when compared to the standard (LT) samples.
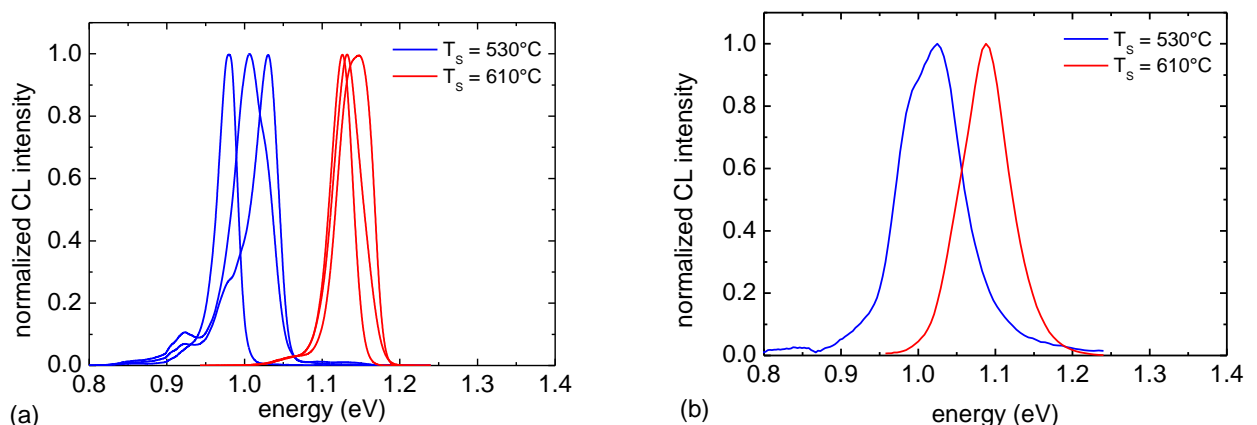
Figure 6.3: (a) Selected normalized CL point spectra measured at 10 K from the front for both types of samples. The spectra were chosen in order to demonstrate the maximum variation of the peak energy within the sample area. (b) CL spectra averaged over 400 μm^2 at room-temperature for both kinds of absorbers in front configuration.

The lateral homogeneity of the CL emission energy can be characterized when detecting point spectra. Figure 6.3(a) shows selected CL spectra taken at single spots on LT and HT samples, respectively. These spots were spread over an area of 400 μm^2 and were chosen to visualize the maximum variation of the peak position. While only a slight variation in the energy of the peak maximum of about 20 meV is observed for HT absorbers, the peak shifts over a range of 80 meV for layers prepared by the LT standard process. How can this shift be interpreted? According to the charge carrier drift model, the lateral distribution of the emission energy E_{qDAP} corresponds to the lateral distribution of the minimum band-gap $E_{gap,min}$, if the drift-length L_{drift} is sufficiently large and if the red-shift can be considered to be constant. Hence, the lateral variation of the peak energy can be explained by a lateral variation of (a) the band-gap minimum $E_{gap,min}$ (i.e. the minimum GGI), (b) the drift length L_{drift} (i.e. the $\mu\tau$-product) or (c) the average amplitude of fluctuations γ_{opt} (i.e. the Cu/III ratio). It has been suggested that these effects can be partially distinguished by investigating the room-temperature luminescence [Sie11]. Variations that are also observed at room-temperature can be assumed to be only due to an inhomogeneous minimum band-gap energy, because the drift length has been shown to rather increase with temperature (hence it is assumed to be sufficiently large) and the potential fluctuations are screened by free carriers at room-temperature [Sie11]. Furthermore, band-to-band recombination is presumed to be the dominant recombination process above 150 K [Kir07]; thus, the CL peak energy can be assumed to be identical to the band-gap.

Room-temperature CL spectra averaged over an area of 400 μm^2 are plotted in Figure 6.3(b) for both kinds of absorbers. The room-temperature band-gap is determined from the peak energy to $E_{gap,LT}$ = 1.01±0.05 eV, $E_{gap,HT}$ = 1.09±0.03 eV, if the error of the measurement is associated with the width of the peak. Slightly larger values of 1.06 and 1.13 eV for the band-gap at room-temperature are calculated from the minimum GGI measured by SIMS of around 0.10 and 0.22 for LT and HT samples, respectively (temperature dependence of the band-gap calculated according to [Yos98]). Point spectra as in Figure 6.3(a) are difficult to measure at room-temperature due to the weakness of the luminescence signal, but they do not indicate a variation of more than 10 meV.

Nevertheless, note that this does not exclude variations of the band-gap to be present in the layer: A lateral variation of the band-gap would in turn induce a lateral quasi-electric field; thus, the carriers will drift towards the point of minimum band-gap. This means that the effective lateral resolution limit for band-gap measurements by luminescence methods is determined by the lateral drift length $L_{drift,lateral}$. Band-gap variations at smaller length scale will not be detected by CL point spectra. To give an estimate of the significance of the effect: a lateral variation in band-gap of 10 meV on a distance of 1 μm leads to a drift length of equally 1 μm according to Eq. (2.18) for a mobility of 100 cm^2 V^{-1} s^{-1} and a lifetime of 10 ns (as presumed at room-temperature, see Section 2.3.2).

However, the lateral homogeneity in emission spectra clearly shows the higher substrate temperature during absorber deposition to lead not only to a reduction of the vertical Ga-grading, but also to a higher degree of lateral homogeneity of the absorber layer.

6.3   Crystal structure of Cu(In,Ga)Se$_2$ deposited at different temperatures

The reduction of the Ga-grading at higher substrate temperature discussed in Section 6.1 leads to the assumption that also the crystal structure of the layer might be influenced by a higher substrate temperature. This has been studied by transmission electron microscopy (TEM). The images are obtained on the very same samples, which were also used in the Sections 6.1 and 6.2.

Figure 6.4 (a) and (b) show bright-field images of the whole layer stack of solar cells made from LT- and HT-absorbers, respectively. The ZnO and the CdS layer can be seen on the top-left, while Mo back-contact layer is found at the bottom-right of the images (LT sample: Mo not visible). The LT-absorber layer exhibits a large number of grains with an average size of about 500 *nm* (traced by black lines). The grain size is reduced even further towards the back-contact, which may be explained by the increase of the Ga-content in this region [Abo08]. In contrast, the HT-sample shows only one large grain in the investigated region reaching from the front- to the back-contact. The grain is confined by two vertical grain-boundaries on both sides and has a width comparable to the film thickness of 2 *μm*.
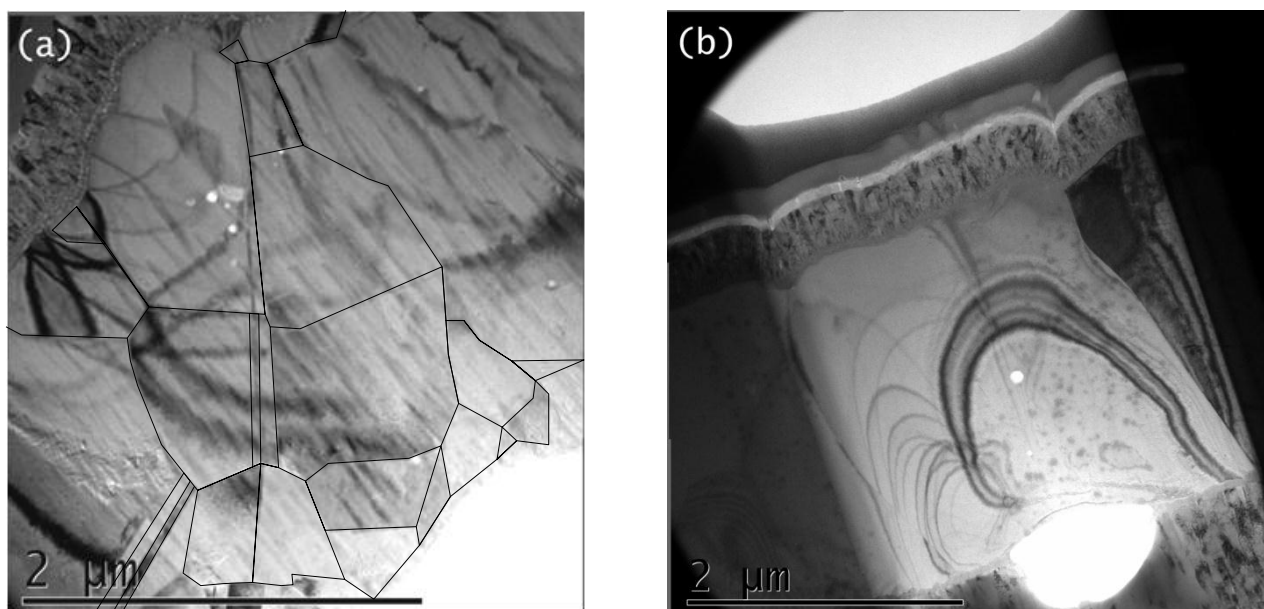
Figure 6.4: TEM bright-field images in cross section configuration of solar cells made from LT (a) and HT (b) absorbers. The grain structure of the LT image is emphasized by black lines. HT layer stack with MgF$_2$ AR-coating.

From these two images it can be concluded that the higher substrate temperature leads not only to an increased homogeneity of the elemental distribution (SIMS) and the crystalline phase (XRD), but also to a strong reduction of the number of grain boundaries. An enlarged grain size of HT absorbers is also found by laterally resolved CL imaging (not shown, images shown for LT absorbers in Section 5.6). As mentioned in Section 5.2, the electrical transport may or may not be limited by the grain boundaries. The absence of horizontal grain boundaries in HT absorbers may be a possible explanation for the increase in the $\mu\tau$-product observed in Section 6.2.

6.4 Performance of devices made from Cu(In,Ga)Se$_2$ deposited at different temperatures

As discussed in Section 2.1.3, both vertical and lateral inhomogeneities as well as grain boundaries are suspected to deteriorate the solar cell performance due to an increase of the saturation current j_0. Thus, it can be assumed that solar cells made from HT absorbers might show lower j_0 and, thus, higher efficiencies when compared to LT absorbers. In Figure 6.5(a), dark and light j-V-characteristics of two typical cells made from HT and LT absorbers without AR-coating are exemplarily displayed. The solar cell parameters are listed in Table 6.2 for both types of absorbers as extracted using the one-diode-model.
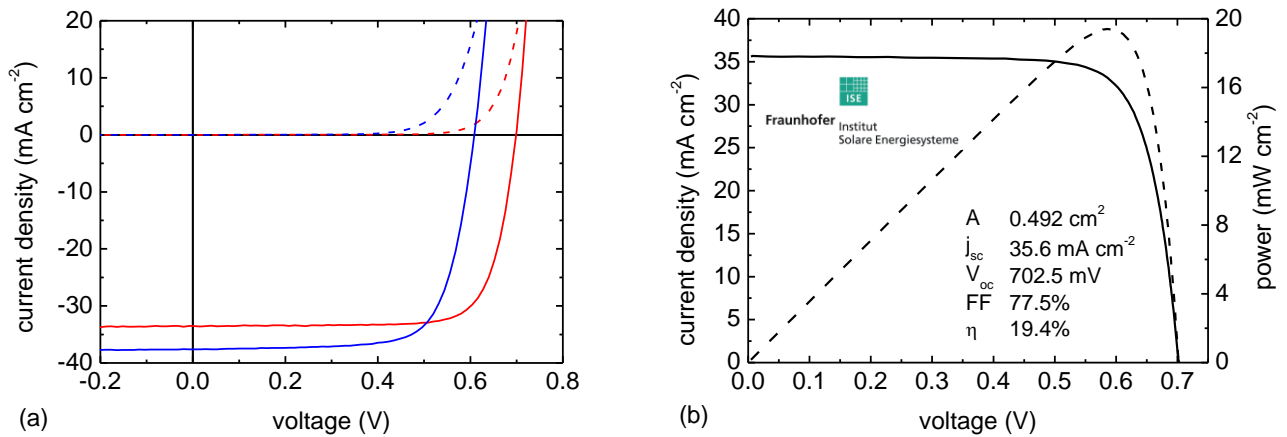
Figure 6.5: (a) j-V-characteristics of two typical cells made from LT and HT absorbers, respectively, without anti-reflection coating. (b) j-V-characteristic and power-voltage curve as certified by Fraunhofer ISE in Freiburg, Germany, under standard AM1.5G conditions for the best cell made from HT absorbers with MgF$_2$ anti-reflection coating; solar cell parameters as inset.

	j_{sc} (mA cm^{-2})	V_{oc} (mV)	FF (%)	η (%)	R_{sh} (kΩ cm^2)	R_s (Ω cm^2)	n_{id}	j_0 (mA cm^{-2})
HT	-33.6(6)	686(6)	76.8(4)	17.7(4)	2.7(6)	0.25(6)	1.52(2)	1.0(0.3) 10^{-6}
LT	-36.7(6)	605(1)	72.6(7)	16.1(3)	1.4(3)	0.29(7)	1.65(6)	2.7(1.3) 10^{-5}

Table 6.2: Solar cell parameters determined from a set of 15 cells made from both LT and HT absorbers without anti-reflection coating and analyzed on the basis of the one-diode model.
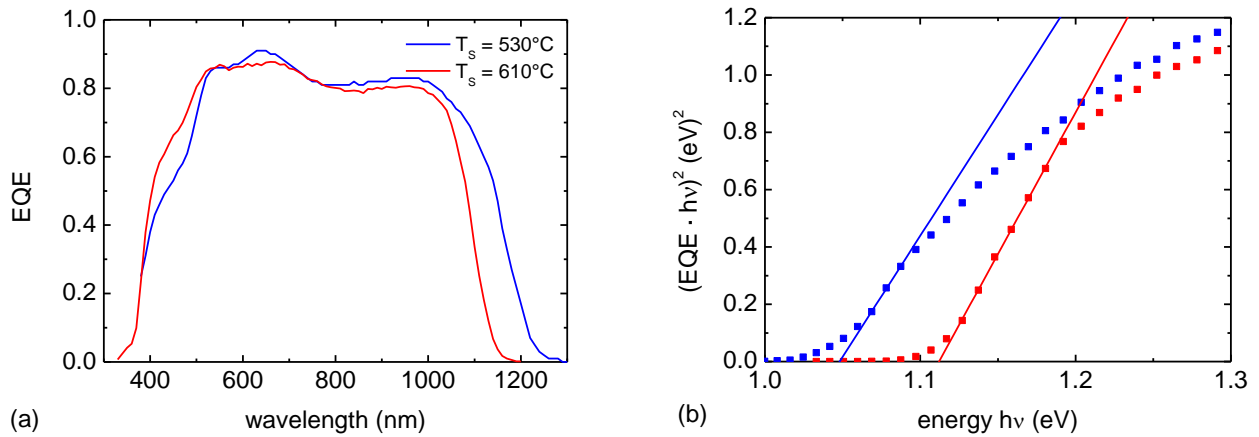
Figure 6.6: (a) *EQE* **spectra of solar cells made from LT and HT absorbers without anti-reflection coating. (b) Determination of the band-gap from the** *EQE* **spectra according to the relation for direct band-gap semiconductors.**

The short circuit current density j_{sc} is reduced for cells from HT absorbers compared to LT absorbers, which can be explained by the increase in the minimum band-gap due to the rather homogeneous Ga-distribution. This assumption can be validated by *EQE* measurements, which are shown in Figure 6.6(a). The onset of the *EQE* in the IR region is shifted to higher wavelengths for the LT absorber when compared to the HT sample. The effective band-gap of a direct semiconductor can be determined by plotting $(EQE\,h\nu)^2$ as a function of $(h\nu)^2$ [Mos59] as done in Figure 6.6(b). The band-gap of the HT sample can be well determined to 1.11±0.02 *eV*, but the LT-data show considerable deviations from the linear shape, which leads to a larger error in band-gap determination (1.05±0.04 *eV*). Both values are consistent with the band-gap minimum determined by room-temperature CL and SIMS.

Apart from the discussed difference in j_{sc}, an increase in fill factor and in open-circuit voltage (of about 80 *mV*) can be observed in the HT case. The higher V_{oc} is found in the one-diode model to be mainly due to the reduction of the saturation current (and the diode ideality factor) as well as a higher shunt resistance and approximately matches the difference in the $E_{gap,min}$: $e\,\Delta V_{oc} \approx \Delta E_{gap,min}$. But in fact, it is commonly assumed that the dominating recombination mechanism in Cu(In,Ga)Se$_2$ solar cells is of Shockley-Read-Hall-type in the space charge region [Rau99b; Kle01; Rau01]. Therefore, the open-circuit voltage in Ga-graded cells should be proportional to the band-gap near the interface [Dul01] and rather independent of $E_{gap,min}$.

The recombination process is alternatively discussed to be governed by enhanced recombination in the bulk due to inhomogeneities [Gra05; Sie11] – either at charged grain boundaries or in the grains due to band-gap- or electrostatic fluctuations. As a strongly increased grain size is observed in Section 6.3, an effective reduction of the number of grain boundaries may also be a possible

explanation for the lower saturation current. H, a small grain size has also been shown to be compatible with high-efficiency performance of the device [Rau09].

Together with the improved fill factor, the higher open-circuit voltage overcompensates the loss in short-circuit current density. Using an MgF$_2$-anti-reflection coating, a certified efficiency of (19.4±0.6)% is obtained as shown in Figure 6.5 (b).

Summary

In conclusion, it has been shown that an increase of the substrate temperature from the standard value of 530°C to 610°C strongly influences the formation of the Cu(In,Ga)Se$_2$ absorber layer. This elevation of the temperature was possible only on a specially developed Na-containing high-temperature resistant glass, but it can be easily integrated in existing industrial technology. The deposition process at higher substrate temperature is shown to lead to

- a homogenization of the Ga-profile and an increase of the optical band-gap,

- a reduction of the lateral variation of the CL peak energy at low temperatures,

- the absence of deep-level emission in low-temperature luminescence spectra,

- an increase of the grain size and, therefore, a strongly reduced number of grain boundaries,

- a decrease of the losses at the p-n-junction (shunt resistance, saturation current), which leads to increased V_{oc} and *FF* of solar cells made from these absorbers,

- an increase of the solar cell efficiency up to 19.4%, which is close to the present world record of 20.3% [Jac10].

Note that the softening point of the glass allows to apply even higher temperatures of up to 700°C, but for solar cells made from absorbers prepared at temperatures above 610°C a decrease of the solar cell performance is observed [Ris09]. It is presumed that the standard deposition process at the HZB needs to be modified in this high temperature regime.

7 Summary and Outlook

The three different issues discussed in this thesis aim for a deeper understanding of Cu(In,Ga)Se$_2$ material properties and solar cell functionality. They can help to achieve Cu(In,Ga)Se$_2$ solar cells of higher efficiencies – in laboratory as well as in industrial process lines.

A separate summary and outlook is given here for each of these issues discussed in the Chapters 4, 5 and 6:

(1) Near-surface ion implantation in Cu(In,Ga)Se$_2$ absorber layers has been studied as a possible method for the fabrication of buffer-free solar cells. SCAPS simulations show the beneficial effect of an n-type surface layer (buried junction) for solar cells suffering from high interface recombination. In order to obtain such a buried junction by means of ion implantation, an annealing procedure has been developed that avoids annealing-induced degradation of the solar cell performance, minimizes the diffusion of the implanted ions, and recovers the solar cell degradation induced by the implantation damage. Buffer-free solar cells made from implanted absorbers showed strongly improved diode characteristics (saturation current density, diode ideality factor), which are comparable to the ones of reference cells with a CdS buffer. A maximum efficiency of 10.2% (11.2% active area) has been obtained for a buffer-free solar cell made from a Cu(In,Ga)Se$_2$ absorber after 20 *keV* Cd-implantation and subsequent thermal treatment.

The good-quality diode behavior points out the potential of this new approach and provides a "proof of concept". It also confirms the importance of an interface inversion for device functionality. Further improvements can be expected for an optimization of the experimental parameters of ion implantation (ion fluence, ion energy) and annealing (temperature, dwell time, heating and cooling ramps). The use of a softer deposition method for ZnO-window deposition may eliminate the losses in short-circuit current density.

(2) A model has been developed for the application of luminescence techniques on band-gap graded semiconductor thin-films. The Ga-grading in Cu(In,Ga)Se$_2$ layers is shown to strongly influence its luminescence properties. Several qDAP-emissions have been detected in the CL and PL spectra and related to the local Ga-contents in different regions of the layer. The distribution of the luminescence signal over the depth of the layer has been mapped and correlated to the band-gap profile. Drift of excited charge carriers towards the

minimum of the band-gap is induced by the quasi-electric field and strongly increases with increasing injection density. It has been shown that this drift also has to be taken considered when explaining the spectra obtained from plan-view CL and PL measurements. Monochromatic CL imaging on a cross-section sample has been shown to be capable to determine the minority carrier mobility by measuring its drift length.

It is found that the knowledge of the shape of both the generation profile and the Ga-grading inherent in the sample is essential for understanding the luminescence signal coming from it. Hence, taking into account the influence of the grading is shown to be crucial for investigations on band-gap-graded $Cu(In,Ga)Se_2$. This approach also opens up the possibility for investigations on the motion of charge carriers in graded-gap $Cu(In,Ga)Se_2$ layers and, thus, can also serve as a method to investigate basic semiconductor properties. A more quantitative evaluation of transport properties would require a more detailed understanding of the recombination at surfaces and grain boundaries and high-injection effects in Cu-poor $Cu(In,Ga)Se_2$ thin-films.

(3) An increase of the substrate temperature from the standard value of 530°C to 610°C has been shown to strongly influence the formation of the $Cu(In,Ga)Se_2$ absorber layer. The higher temperature is found to lead to a reduced vertical Ga-grading, a reduced lateral variation of the CL peak energy at low temperatures, an increase of the grain size, a decrease of the losses at the p-n-junction (shunt resistance, saturation current) and, as a consequence, a considerable increase of the solar cell efficiency up to 19.4%.

This elevation of the temperature was possible only by employing a specially developed Na-containing high-temperature resistant glass, but the integration of the high-temperature process in existing industrial $Cu(In,Ga)Se_2$ deposition technologies would be fairly simple. A further optimization of the deposition process will be necessary for the use of even higher temperatures. This way, an increase of the substrate temperature can be a simple, but important contribution to achieving a further increase of module efficiencies from industrial process lines and $Cu(In,Ga)Se_2$ solar cells with record efficiencies clearly exceeding 20%.

Bibliography

[Abo05]   Abou-Ras D., Kostorz G., Romeo A., Rudmann D., Tiwari A., *Structural and chemical investigations of CBD- and PVD-CdS buffer layers and interfaces in Cu(In,Ga)Se$_2$-based thin film solar cells*, Thin Solid Films 480 (2005) 118-123.

[Abo08]   Abou-Ras D., Caballero R., Kaufmann C.A., Nichterwitz M., Sakurai K., Schorr S., Unold T., Schock H.W., *Impact of the Ga concentration on the microstructure of CuIn$_{1-x}$Ga$_x$Se$_2$*, Physica Status Solidi-Rapid Research Letters 2(3) (2008) 135-137.

[Abo09]   Abou-Ras D., Koch C.T., Kustner V., van Aken P.A., Jahn U., Contreras M.A., Caballero R., Kaufmann C.A., Scheer R., Unold T., Schock H.W., *Grain-boundary types in chalcopyrite-type thin films and their correlations with film texture and electrical properties*, Thin Solid Films 517(7) (2009) 2545-2549.

[Alo02]   Alonso M.I., Garriga M., Rincon C.A.D., Hernandez E., Leon M., *Optical functions of chalcopyrite CuGa$_x$In$_{1-x}$Se$_2$ alloys*, Applied Physics A-Materials Science & Processing 74(5) (2002) 659-664.

[Bal08]   Balboul M.R., Schock H.W., Fayak S.A., El-Aal A.A., Werner J.H., Ramadan A.A., *Correlation of structure parameters of absorber layer with efficiency of Cu(In,Ga)Se$_2$ solar cells*, Applied Physics a-Materials Science & Processing 92(3) (2008) 557-563.

[Bär04]   Bär M., Bohne W., Rohrich J., Strub E., Lindner S., Lux-Steiner M.C., Fischer C.H., Niesen T.P., Karg F., *Determination of the band gap depth profile of the penternary Cu(In$_{1-x}$Ga$_x$)(S$_y$Se$_{1-y}$)$_2$ chalcopyrite from its composition gradient*, Journal of Applied Physics 96(7) (2004) 3857-3860.

[Bas96]   Basol B.M., Kapur V.K., Halani A., Leidholm C.R., Sharp J., Sites J.R., Swartzlander A., Matson R., Ullal H., *Cu(In,Ga)Se$_2$ thin films and solar cells prepared by selenization of metallic precursors*, Journal of Vacuum Science & Technology a-Vacuum Surfaces and Films 14(4) (1996) 2251-2256.

[Bas11]   Bastek J., Stolwijk N., *Diffusion of Zn in polycrystalline Cu(In,Ga)Se$_2$ thin-films*, unpublished work.

[Bau05]   Bauer G.H., Gutay L., Kniese R., *Structural properties and quality of the photoexcited state in Cu(In$_{1-x}$Ga$_x$)Se$_2$ solar cell absorbers with lateral submicron resolution*, Thin Solid Films 480 (2005) 259-263.

[Bau01]   Bauknecht A., Siebentritt S., Albert J., Lux-Steiner M.C., *Radiative recombination via intrinsic defects in Cu$_x$Ga$_y$Se$_2$*, Journal of Applied Physics 89(8) (2001) 4391-4400.

[Bec06]   Beckhoff B., Langhoff N., Kanngiefer B., Wedell R., Wolff H., (Eds.), *Handbook of practical X-ray fluorescence analysis,* Springer-Verlag, Berlin-Heidelberg (2006).

[Ben05]   Benabdeslem M., Benslim N., Bechiri L., Mahdjoubi L., Hannech E.B., Nouet G., *Diffusion of Zn in CuInSe$_2$ bulk crystals*, Journal of Crystal Growth 274(1-2) (2005) 144-148.

[Ben87]   Benninghoven A., Rüdenauer F.G., Werner H.W., *Secondary ion mass spectrometry: basic concepts, instrumental aspects, applications and trends,* Wiley, New York (1987).

[Ber76]   Berz F., Kuiken H.K., *Theory of life time measurements with scanning electron-microscope - steady state*, Solid-State Electronics 19(6) (1976) 437-445.

[Bha04]   Bhattacharya R.N., Contreras M.A., Teeter G., *18.5% copper indium gallium diselenide (CIGS) device using single-layer, chemical-bath-deposited ZnS(O,OH)*, Japanese Journal of Applied Physics Part 2-Letters & Express Letters 43(11B) (2004) L1475-L1476.

[Bin82]   Binsma J.J.M., Giling L.J., Bloem J., *Luminescence of $CuInS_2$ .II. Exciton and near edge emission*, Journal of Luminescence 27(1) (1982) 55-72.

[Blo92]   Blood P., Orton J.W., *The Electrical Characterization of Semiconductors: Majority Carriers and Electron States,* Academic Press, London (1992).

[Bro10]   Brown G., Pudov A., Cardozo B., Faifer V., Bykov E., Contreras M., *Quantitative imaging of electronic nonuniformities in $Cu(In,Ga)Se_2$ solar cells*, Journal of Applied Physics 108(7) (2010) 074516.

[BMU10]   Bundesministerium für Umwelt, Naturschutz und Reaktorsicherheit, *Erneuerbare Energien - Entwicklung in Deutschland 2010*, from: http://www.erneuerbare-energien.de/files/pdfs/allgemein/application/pdf/ee_zahlen_2010_bf.pdf.

[Bur00]   Burgelman M., Nollet P., Degrave S., *Modelling polycrystalline semiconductor solar cells*, Thin Solid Films 361 (2000) 527-532.

[Bur08]   Burgelman M., Marlein J., *Analysis of graded band gap solar cells with SCAPS*, 23rd European Photovoltaic Solar Energy Conference Valencia, (2008) 2151-2155.

[Bur54]   Burstein E., *Anomalous optical absorption limit in InSb*, Physical Review 93(3) (1954) 632-633.

[Cab10]   Caballero R., Izquierdo-Roca V., Fontane X., Kaufmann C.A., Alvarez-Garcia J., Eicke A., Calvo-Barrio L., Perez-Rodriguez A., Schock H.W., Morante J.R., *Cu deficiency in multi-stage co-evaporated $Cu(In,Ga)Se_2$ for solar cells applications: Microstructure and Ga in-depth alloying*, Acta Materialia 58(9) (2010) 3468-3476.

[Cah89]   Cahen D., Noufi R., *Defect chemical explanation for the effect of air anneal on $CdS/CuInSe_2$ solar-cell performance*, Applied Physics Letters 54(6) (1989) 558-560.

[Cah91]   Cahen D., Noufi R., *Surface passivation of polycrystalline, chalcogenide based photovoltaic cells*, Solar Cells 30(1-4) (1991) 53-59.

[Can00]   Canava B., Guillemoles J.F., Yousfi E.B., Cowache P., Kerber H., Loeffl A., Schock H.W., Powalla M., Hariskos D., Lincot D., *Wet treatment based interface engineering for high efficiency $Cu(In,Ga)Se_2$ solar cells*, Thin Solid Films 361 (2000) 187-192.

[Car82]   Carpenter M.K., Streckert H.H., Ellis A.B., *Photoluminescence and Electroluminescence in Graded Cadmium Sulfoselenide Electrodes - Applications to Photoelectrochemical Cell*, Journal of Solid State Chemistry 45(1) (1982) 51-62.

[Coj11]   Cojocaru-Miredin O., Choi P., Wuerz R., Raabe D., *Atomic-scale characterization of the $CdS/CuInSe_2$ interface in thin-film solar cells*, Applied Physics Letters 98(10) (2011) 103504.

[Con02]   Contreras M.A., Romero M.J., Hasoon B.T.E., Noufi R., Ward S., Ramanathan K., *Optimization of CBD CdS process in high-efficiency $Cu(In,Ga)Se_2$-based solar cells*, Thin Solid Films 403 (2002) 204-211.

[Con06]   Contreras M.A., Romero M.J., Noufi R., *Characterization of $Cu(In,Ga)Se_2$ materials used in record performance solar cells*, Thin Solid Films 511 (2006) 51-54.

[Con09]   Contreras M.A., Repins I., Metzger W.K., Romero M., Abou-Ras D., *Se activity and its effect on Cu(In,Ga)Se$_2$ photovoltaic thin films*, Physica Status Solidi A-Applications and Materials Science 206(5) (2009) 1042-1048.

[Cwi08]   Cwil M., Igalson M., Zabierowski P., Siebentritt S., *Charge and doping distributions by capacitance profiling in Cu(In,Ga)Se$_2$ solar cells*, Journal of Applied Physics 103(6) (2008) 063701.

[Die11]   Dietrich J., Abou-Ras D., Rissom T., Unold T., Schock H.W., Boit C., unpublished work.

[Dir98]   Dirnstorfer I., Wagner M., Hofmann D.M., Lampert M.D., Karg F., Meyer B.K., *Characterization of CuIn(Ga)Se$_2$ thin films - II. In-rich layers*, Physica Status Solidi a-Applied Research 168(1) (1998) 163-175.

[Dir99]   Dirnstorfer I., Hofmann D.M., Meister D., Meyer B.K., *Postgrowth thermal treatment of CuIn(Ga)Se-2: Characterization of doping levels in In-rich thin films*, Journal of Applied Physics 85(3) (1999) 1423-1428.

[Dro07]   Drouin D., Couture A.R., Joly D., Tastet X., Aimez V., Gauvin R., *CASINO V2.42 - A fast and easy-to-use modeling tool for scanning electron microscopy and microanalysis users*, Scanning 29(3) (2007) 92-101.

[Dru00]   Drude P., *Zur Elektronentheorie der Metalle*, Annalen der Physik 506(3) (1900) 566-613.

[Dul01]   Dullweber T., Hanna G., Rau U., Schock H.W., *A new approach to high-efficiency solar cells by band gap grading in Cu(In,Ga)Se$_2$ chalcopyrite semiconductors*, Solar Energy Materials and Solar Cells 67(1-4) (2001) 145-150.

[Dut58]   Dutton D., *Fundamental absorption edge in cadmium sulfide*, Physical Review 112(3) (1958) 785-792.

[Eis10]   Eisenbarth T., Unold T., Caballero R., Kaufmann C.A., Schock H.W., *Interpretation of admittance, capacitance-voltage, and current-voltage signatures in Cu(In,Ga)Se$_2$ thin film solar cells*, Journal of Applied Physics 107(3) (2010) 034509.

[Eis98]   Eisgruber I.L., Granata J.E., Sites J.R., Hou J., Kessler J., *Blue-photon modification of nonstandard diode barrier in CuInSe$_2$ solar cells*, Solar Energy Materials and Solar Cells 53(3-4) (1998) 367-377.

[Eng99]   Engelhardt F., Bornemann L., Köntges M., Meyer T., Parisi J., Pschorr-Schoberer E., Hahn B., Gebhardt W., Riedl W., Rau U., *Cu(In,Ga)Se$_2$ solar cells with a ZnSe buffer layer: Interface characterization by quantum efficiency measurements*, Progress in Photovoltaics 7(6) (1999) 423-436.

[Eve71]   Everhart T.E., Hoff P.H., *Determination of kilovolt electron energy dissipation vs penetration depth in solid materials*, Journal of Applied Physics 42(13) (1971) 5837-5846.

[Fis10]   Fischer C.-H., Allsop N.A., Gledhill S.E., Köhler T., Krüger M., Sáez-Araoz R., Fu Y., Schwieger R., Richter J., Wohlfart P., Bartsch P., Lichtenberg N., Lux-Steiner M.C., *The spray-ILGAR® (ion layer gas reaction) method for the deposition of thin semiconductor layers: Process and applications for thin film solar cells*, Solar Energy Materials and Solar Cells 95(6) (2010) 1518-1526.

[Fon81]   Fonash S.J., *Solar Cell Device Physics,* Academic Press, New York (1981).

[Gla05]   Glatzel T., Steigert H., Sadewasser S., Klenk R., Lux-Steiner M.C., *Potential distribution of Cu(In,Ga)(S,Se)$_2$-solar cell cross-sections measured by Kelvin probe force microscopy*, Thin Solid Films 480 (2005) 177-182.

[Glo04]   Gloeckler M., Sites J.R., *Apparent quantum efficiency effects in CdTe solar cells*, Journal of Applied Physics 95(8) (2004) 4438-4445.

[Glo05a]   Gloeckler M., *Device Physics of Cu(In,Ga)Se$_2$ Thin-Film Solar Cells,* PhD Thesis, Colorado State University, Fort Collins, Colorado (2005).

[Glo05b]   Gloeckler M., Sites J.R., *Band-gap grading in Cu(In,Ga)Se$_2$ solar cells*, Journal of Physics and Chemistry of Solids 66(11) (2005) 1891-1894.

[Glo05c]   Gloeckler M., Sites J.R., *Efficiency limitations for wide-band-gap chalcopyrite solar cells*, Thin Solid Films 480 (2005) 241-245.

[Gol03]   Goldstein J., Newbury D.E., Joy D.C., Lyman C.E., Echlin P., Lifshin E., Sawyer L., Michael J.R., *Scanning electron microscopy and x-ray microanalysis,* Kluwer Academic/Plenum Publishers, New York (2003).

[Gra05]   Grabitz P.O., Rau U., Werner J.H., *Modeling of spatially inhomogeneous solar cells by a multi-diode approach*, Physica Status Solidi A-Applications and Materials Science 202(15) (2005) 2920-2927.

[Gre09]   Green M.A., *Do Built-in Fields Improve Solar Cell Performance?*, Progress in Photovoltaics 17(1) (2009) 57-66.

[Gri07]   Grimm A., Klenk R., Lux-Steiner M.C., Visbeck S., *Bulk and interface properties of (Zn,Mg)O buffer layers sputtered in hydrogen-containing atmosphere*, Thin Solid Films 515(15) (2007) 6073-6075.

[Gri10]   Grimm A., Just J., Kieven D., Lauermann I., Palm J., Neisser A., Rissom T., Klenk R., *Sputtered Zn(O,S) for junction formation in chalcopyrite-based thin film solar cells*, Physica Status Solidi-Rapid Research Letters 4(5-6) (2010) 109-111.

[Gri26]   Grimm H.G., Sommerfeld A., *Über den Zusammenhang des Abschlusses der Elektronengruppen im Atom mit den chemischen Valenzzahlen*, Zeitschrift für Physik 36 (1926) 36-59.

[Gui98]   Guillen C., Martinez M.A., Herrero J., *Accurate control of thin film CdS growth process by adjusting the chemical bath deposition parameters*, Thin Solid Films 335(1-2) (1998) 37-42.

[Gus98]   Gustafsson A., Pistol M.E., Montelius L., Samuelson L., *Local probe techniques for luminescence studies of low-dimensional semiconductor structures*, Journal of Applied Physics 84(4) (1998) 1715-1775.

[Gus10]   Gustafsson A., Bolinsson J., Skold N., Samuelson L., *Determination of diffusion lengths in nanowires using cathodoluminescence*, Applied Physics Letters 97(7) (2010) 072114.

[Haa98]   Haalboom T., Godecke T., Ernst F., Ruhle M., Herberholz R., Schock H.W., Beilharz C., Benz K.W., *Phase relations and microstructure in bulk materials and thin films of the ternary system Cu-In-Se*, Ternary and Multinary Compounds 152 249-252, Iop Publishing Ltd**,** Bristol (1998).

[Haa11a]   Haarstrich J., Metzner H., Oertel M., Ronning C., Rissom T., Kaufmann C.A., Unold T., Schock H.W., Windeln J., Mannstadt W., Rudigier-Voigt E., *Increased homogeneity and open-circuit voltage of Cu(In,Ga)Se$_2$ solar cells due to higher deposition temperature*, Solar Energy Materials and Solar Cells 95(3) (2011) 1028-1030.

[Haa11b]   Haarstrich J., Metzner H., Ronning C., Rissom T., Kaufmann C.A., Schock H.W., Mannstadt W., Rudigier-Voigt E., Scheumann V., *Near-interface doping by ion implantation in Cu(In,Ga)Se₂ solar cells*, Thin Solid Films (2011) doi: 10.1016/j.tsf.2010.1012.1090.

[Häd09]   Hädrich M., *Materialwissenschaftliche Untersuchungen an CdTe-CdS-Heterosolarzellen* Friedrich-Schiller-Universität, Jena (2009).

[Häd11]   Hädrich M., Metzner H., Reislöhner U., Kraft C., *Modelling the quantum efficiency of cadmium telluride solar cells*, Solar Energy Materials and Solar Cells 95(3) (2011) 887-893.

[Haf10]   Hafemeister M., Siebentritt S., Albert J., Lux-Steiner M.C., Sadewasser S., *Large Neutral Barrier at Grain Boundaries in Chalcopyrite Thin Films*, Physical Review Letters 104(19) (2010) 196602.

[Han07]   Hanket G.M., Shafarman W.N., McCandless B.E., Birkmire R.W., *Incongruent reaction of Cu(InGa) intermetallic precursors in H_2Se and H_2S*, Journal of Applied Physics 102(7) (2007) 074922.

[Han06]   Hanna G., Glatzel T., Sadewasser S., Ott N., Strunk H.P., Rau U., Werner J.H., *Texture and electronic activity of grain boundaries in Cu(In,Ga)Se₂ thin films*, Applied Physics A-Materials Science & Processing 82(1) (2006) 1-7.

[Har96]   Hariskos D., Ruckh M., Ruhle U., Walter T., Schock H.W., Hedstrom J., Stolt L., *A novel cadmium free buffer layer for Cu(In,Ga)Se₂ based solar cells*, Solar Energy Materials and Solar Cells 41(2) (1996) 345-353.

[Har05]   Hariskos D., Spiering S., Powalla M., *Buffer layers in Cu(In,Ga)Se₂ solar cells and modules*, Thin Solid Films 480 (2005) 99-109.

[Hea04]   Heath J.T., Cohen J.D., Shafarman W.N., *Bulk and metastable defects in $CuIn_{1-x}Ga_xSe_2$ thin films using drive-level capacitance profiling*, Journal of Applied Physics 95(3) (2004) 1000-1010.

[Heg04]   Hegedus S., Shafarman W.N., *Thin-film solar cells: Device measurements and analysis*, Progress in Photovoltaics 12(2-3) (2004) 155-176.

[Heg07]   Hegedus S., Desai D., Thompson C., *Voltage dependent photocurrent collection in CdTe/CdS solar cells*, Progress in Photovoltaics 15(7) (2007) 587-602.

[Hes99]   Heske C., Eich D., Fink R., Umbach E., van Buuren T., Bostedt C., Terminello L.J., Kakar S., Grush M.M., Callcott T.A., Himpsel F.J., Ederer D.L., Perera R.C.C., Riedl W., Karg F., *Observation of intermixing at the buried CdS/Cu(In,Ga)Se-2 thin film solar cell heterojunction*, Applied Physics Letters 74(10) (1999) 1451-1453.

[Het06]   Hetzer M.J., Strzhemechny Y.M., Gao M., Goss S., Contreras M.A., Zunger A., Brillson L.J., *On microscopic compositional and electrostatic properties of grain boundaries in polycrystalline $CuIn_{1-x}Ga_xSe_2$*, Journal of Vacuum Science & Technology B 24(4) (2006) 1739-1745.

[Hie11]   Hiepko K., *Diffusion von Cadmium in polykristallinem Cu(In,Ga)Se₂ für Dünnschichtsolarzellen,* Diploma Thesis, Westfälische Wilhelms-Universität, Münster (2011).

[Hul11]   Hultqvist A., Edoff M., Torndahl T., *Evaluation of Zn-Sn-O buffer layers for $CuIn_{0.5}Ga_{0.5}Se_2$ solar cells*, Progress in Photovoltaics 19(4) (2011) 478-481.

[Ish08]   Ishizuka S., Hommoto H., Kido N., Hashimoto K., Yamada A., Niki S., *Efficiency enhancement of Cu(In,Ga)Se₂ solar cells fabricated on flexible polyimide substrates using alkali-silicate glass thin layers*, Applied Physics Express 1(9) (2008) 092303.

[Ish09]   Ishizuka S., Yamada A., Islam M.M., Shibata H., Fons P., Sakurai T., Akimoto K., Niki S., *Na-induced variations in the structural, optical, and electrical properties of Cu(In,Ga)Se₂ thin films*, Journal of Applied Physics 106(3) (2009) 034908.

[Jac10]   Jackson P., Hariskos D., Lotter E., Paetel S., Wuerz R., Menner R., Wischmann W., Powalla M., *New world record efficiency for Cu(In,Ga)Se₂ thin-film solar cells beyond 20%*, Progress in Photovoltaics (2010) doi: 10.1002/pip.1078.

[Kan82]   Kanaya K., Okayama S., *Penetration and energy-loss theory of electrons in solid targets*, Journal of Physics D-Applied Physics 5(1) (1972) 43-58.

[Kan07]   Kanevce A., Sites J.R., *Impact of nonuniformities on thin Cu(In,Ga)Se₂ solar cell performance*, Symposium on Thin-Film Compound Semiconductor Photovoltaics held at the 2007 MRS Spring Meeting, San Francisco, CA, (2007) 293-298.

[Kar02]   Karpov V.G., Compaan A.D., Shvydka D., *Effects of nonuniformity in thin-film photovoltaics*, Applied Physics Letters 80(22) (2002) 4256-4258.

[Kau09]   Kaufmann C.A., Caballero R., Unold T., Hesse R., Klenk R., Schorr S., Nichterwitz M., Schock H.W., *Depth profiling of Cu(In,Ga)Se₂ thin films grown at low temperatures*, Solar Energy Materials and Solar Cells 93(6-7) (2009) 859-863.

[Kaw98]   Kawashima T., Adachi S., Miyake H., Sugiyama K., *Optical constants of CuGaSe₂ and CuInSe₂*, Journal of Applied Physics 84(9) (1998) 5202-5209.

[Kaz79]   Kazmerski L.L., *Grain-boundary and interdiffusion studies in compound semiconductor thin-films and devices utilizing auger-electron spectroscopy and secondary ion mass-spectroscopy*, Thin Solid Films 57(1) (1979) 99-106.

[Kes04]   Kessler F., Rudmann D., *Technological aspects of flexible CIGS solar cells and modules*, Solar Energy 77(6) (2004) 685-695.

[Kie10]   Kieven D., Grimm A., Lauermann I., Rissom T., Klenk R., *Band alignment at Sb₂S₃/Cu(In,Ga)Se₂ heterojunctions and electronic characteristics of solar cell devices based on them*, Applied Physics Letters 96(26) (2010) 262101.

[Kij08]   Kijima S., Nakada T., *High-temperature degradation mechanism of Cu(In,Ga)Se₂-based thin film solar cells*, Applied Physics Express 1(7) (2008) 075002.

[Kir07]   Kirchartz T., Rau U., Kurth M., Mattheis J., Werner J.H., *Comparative study of electroluminescence from Cu(In,Ga)Se₂ and Si solar cells*, Thin Solid Films 515(15) (2007) 6238-6242.

[Kle68]   Klein C.A., *Bandgap dependence and related features of radiation ionization energies in semiconductors*, Journal of Applied Physics 39(4) (1968) 2029-2038.

[Kle01]   Klenk R., *Characterisation and modelling of chalcopyrite solar cells*, Thin Solid Films 387(1-2) (2001) 135-140.

[Kni04]   Kniese R., Lammer M., Rau U., Powalla M., *Minority carrier collection in CuGaSe₂ solar cells*, Thin Solid Films 451 (2004) 430-433.

[Kni09]   Kniese R., Powalla M., Rau U., *Evaluation of electron beam induced current profiles of Cu(In,Ga)Se₂ solar cells with different Ga-contents*, Thin Solid Films 517(7) (2009) 2357-2359.

[Kön02]   Köntges M., Reineke-Koch R., Nollet P., Beier J., Schaffler R., Parisi J., *Light induced changes in the electrical behavior of CdTe and Cu(In,Ga)Se$_2$ solar cells*, Thin Solid Films 403 (2002) 280-286.

[Kov81a]   Kovalenko V.F., Peka G.P., Shepel L.G., *Photoluminescent Methods for Determination of Graded Band-Gap Semiconductor Parameters .1. Analysis of Methods*, Physica Status Solidi a-Applied Research 65(2) (1981) 529-534.

[Kov81b]   Kovalenko V.F., Peka G.P., Shepel L.G., *Photoluminescence Methods for Determination of Graded Band-Gap Semiconductror Parameters .2. Experimental Investigation of Al$_x$Ga$_{1-x}$As*, Physica Status Solidi A-Applied Research 66(1) (1981) 407-414.

[Lau09]   Lauer K., Laades A., Ubensee H., Lawerenz A., *Study on the time decay of excess carriers in solar silicon*, Materials Science and Engineering B-Advanced Functional Solid-State Materials 159-60 (2009) 202-205.

[Lia03]   Liao D.X., Rockett A., *Cd doping at the CuInSe$_2$/CdS heterojunction*, Journal of Applied Physics 93(11) (2003) 9380-9382.

[Liu94]   Liu X.X., Sites J.R., *Solar-cell collection efficiency and its variation with voltage*, Journal of Applied Physics 75(1) (1994) 577-581.

[Lud10]   Ludwig C.D.R., Gruhn T., Felser C., Schilling T., Windeln J., Kratzer P., *Indium-Gallium Segregation in CuIn$_x$Ga$_{1-x}$Se$_2$: An Ab Initio-Based Monte Carlo Study*, Physical Review Letters 105(2) (2010) 025702.

[Lun05]   Lundberg O., Edoff M., Stolt L., *The effect of Ga-grading in CIGS thin film solar cells*, Thin Solid Films 480 (2005) 520-525.

[Mal09]   Malm U., Edoff M., *2D device modelling and finite element simulations for thin-film solar cells*, Solar Energy Materials and Solar Cells 93(6-7) (2009) 1066-1069.

[Mar97]   Marudachalam M., Birkmire R.W., Hichri H., Schultz J.M., Swartzlander A., Al-Jassim M.M., *Phases, morphology, and diffusion in CuIn$_x$Ga$_{1-x}$Se$_2$ thin films*, Journal of Applied Physics 82(6) (1997) 2896-2905.

[Mat87]   Matson R.J., Noufi R., Bachmann K.J., Cahen D., *CdS induced homojunction formation in crystalline p-CuInSe$_2$*, Applied Physics Letters 50(3) (1987) 158-160.

[Mat07]   Mattheis J., Rau U., Werner J.H., *Light absorption and emission in semiconductors with band gap fluctuations - A study on Cu(In,Ga)Se$_2$ thin films*, Journal of Applied Physics 101(11) (2007) 113519.

[Met09]   Metzger W.K., Repins I.L., Romero M., Dippo P., Contreras M., Noufi R., Levi D., *Recombination kinetics and stability in polycrystalline Cu(In,Ga)Se$_2$ solar cells*, Thin Solid Films 517(7) (2009) 2360-2364.

[Mia10]   MiaSolé, *MiaSolé Achieves 15.7% Efficiency with Commercial-Scale CIGS Thin Film Solar Modules*, from:
http://www.miasole.com/sites/default/files/MiaSole_release_Dec_02_2010.pdf.

[Mig75]   Migliorato P., Shay J.L., Kasper H.M., Wagner S., *Analysis of electrical and luminescent properties of CuInSe$_2$*, Journal of Applied Physics 46(4) (1975) 1777-1782.

[Min01]   Minemoto T., Hashimoto Y., Satoh T., Negami T., Takakura H., Hamakawa Y., *Cu(In,Ga)Se$_2$ solar cells with controlled conduction band offset of window/Cu(In,Ga)Se$_2$ layers*, Journal of Applied Physics 89(12) (2001) 8327-8330.

[Mos54]   Moss T.S., *The interpretation of the properties of indium antimonide*, Proceedings of the Physical Society of London Section B 67(418) (1954) 775-782.

[Mos59]   Moss T.S., *Optical Properties of Semiconductors,* Butterworth Scientific Publications, London (1959).

[Mud98]   Mudryi A.V., Bodnar I.V., Gremenok V.F., Victorov I.A., Patuk A.I., Shakin I.A., *Free and bound exciton emission in CuInSe$_2$ and CuGaSe$_2$ single crystals*, Solar Energy Materials and Solar Cells 53(3-4) (1998) 247-253.

[Nag03]   Naghavi N., Spiering S., Powalla M., Cavana B., Lincot D., *High-efficiency copper indium gallium diselenide (CIGS) solar cells with indium sulfide buffer layers deposited by atomic layer chemical vapor deposition (ALCVD)*, Progress in Photovoltaics 11(7) (2003) 437-443.

[Nag10]   Naghavi N., Abou-Ras D., Allsop N., Barreau N., Bucheler S., Ennaoui A., Fischer C.H., Guillen C., Hariskos D., Herrero J., Klenk R., Kushiya K., Lincot D., Menner R., Nakada T., Platzer-Björkman C., Spiering S., Tiwari A.N., Torndahl T., *Buffer layers and transparent conducting oxides for chalcopyrite Cu(In,Ga)(S,Se)$_2$ based thin film photovoltaics: present status and current developments*, Progress in Photovoltaics 18(6) (2010) 411-433.

[Nag07]   Nagle T., *Quantum Efficiency as a Device-Physics Interpretation Tool for Thin-Film Solar Cells,* Colorado State University, Fort Collins, Colorado (2007).

[Nak98]   Nakada T., Kume T., Mise T., Kunioka A., *Superstrate-Type Cu(In,Ga)Se$_2$ thin film solar cells with ZnO buffer layers*, Japanese Journal of Applied Physics Part 2-Letters & Express Letters 37(5A) (1998) L499-L501.

[Nak99]   Nakada T., Kunioka A., *Direct evidence of Cd diffusion into Cu(In,Ga)Se$_2$ thin films during chemical-bath deposition process of CdS films*, Applied Physics Letters 74(17) (1999) 2444-2446.

[Nak00]   Nakada T., *Nano-structural investigations on Cd-doping into Cu(In,Ga)Se$_2$ thin films by chemical bath deposition process*, Thin Solid Films 361 (2000) 346-352.

[Nas06]   Nastasi M., Mayer J.W., *Ion Implantation and Synthesis of Materials,* Springer-Verlag, Berlin-Heidelberg (2006).

[Neu86]   Neumann H., *Optical-properties and electronic band-structure of CuInSe$_2$*, Solar Cells 16(1-4) (1986) 317-333.

[Nic09]   Nichterwitz M., Abou-Ras D., Sakurai K., Bundesmann J., Unold T., Scheer R., Schock H.W., *Influence of grain boundaries on current collection in Cu(In,Ga)Se$_2$ thin-film solar cells*, Thin Solid Films 517(7) (2009) 2554-2557.

[Nie95]   Niemegeers A., Burgelman M., Devos A., *On the CdS/CuInSe$_2$ conduction-band discontinuity*, Applied Physics Letters 67(6) (1995) 843-845.

[Nis03]   Nishiwaki S., Satoh T., Hashimoto Y., Shimakawa S.I., Hayashi S., Negami T., Wada T., *Preparation of Zn doped Cu(In,Ga)Se$_2$ thin films by physical vapor deposition for solar cells*, Solar Energy Materials and Solar Cells 77(4) (2003) 359-368.

[Nou86]   Noufi R., Matson R.J., Powell R.C., Herrington C., *The role of oxygen in CuInSe$_2$ thin-films and CdS/CuInSe$_2$ devices*, Solar Cells 16(1-4) (1986) 479-493.

[Ohn98]   Ohnesorge B., Weigand R., Bacher G., Forchel A., Riedl W., Karg F.H., *Minority-carrier lifetime and efficiency of Cu(In,Ga)Se$_2$ solar cells*, Applied Physics Letters 73(9) (1998) 1224-1226.

[Oph91]   Ophir J., Cespedes I., Ponnekanti H., Yazdi Y., Li X., *Elastography - a quantitative method for imaging the elasticity of biological tissues*, Ultrasonic Imaging 13(2) (1991) 111-134.

[Osi82]   Osinskii V.I., Malyshev S.A., Ryzhkov M.P., *Minority-Carrier Transport and Radiative Recombination in $Al_xGa_{1-x}As$ Variable-Composition Structure*, Physica Status Solidi A-Applied Research 74(1) (1982) 43-50.

[Osi85]   Osinskii V.I., Malyshev S.A., Melnikov S.L., Ryzhkov M.P., *Photo-generated carriers in structures with nonlinear band-gap changes*, Physica Status Solidi A-Applied Research 89(1) (1985) 283-292.

[Ott04]   Ott N., Hanna G., Rau U., Werner J.H., Strunk H.P., *Texture of $Cu(In,Ga)Se_2$ thin films and nanoscale cathodoluminescence*, Journal of Physics-Condensed Matter 16(2) (2004) S85-S89.

[Ott01]   Otte K., Lippold G., Hirsch D., Gebhardt R.K., Chasse T., *Conductivity type conversion of p-type $CuInSe_2$ due to hydrogenation*, Applied Surface Science 179(1-4) (2001) 203-208.

[Ott03]   Otte K., Lippold G., Neumann H., Schindler A., *Hydrogen in $CuInSe_2$*, Journal of Physics and Chemistry of Solids 64(9-10) (2003) 1641-1647.

[Pal04]   Palm J., Probst V., Karg F.H., *Second generation CIS solar modules*, Solar Energy 77(6) (2004) 757-765.

[Pan75]   Pankove J.I., *Optical Processes in Semiconductors,* Dover Publications, Inc., New York (1975).

[Par07]   Parish C.M., Russell P.E., *Scanning Cathodoluminescence Microscopy*, Advances in Imaging and Electron Physics 147 1-135, Elsevier Academic Press Inc, San Diego (2007).

[Paw11]   Pawlowski M., Zabierowski P., Bacewicz R., Marko H., Barreau N., *Photoluminescence as a tool for investigations of the junction region in $Cu(In,Ga)Se_2$-based solar cells*, Thin Solid Films (2011) doi: 10.1016/j.tsf.2010.1012.1237.

[Per05]   Persson C., Zhao Y.J., Lany S., Zunger A., *n-type doping of $CuInSe_2$ and $CuGaSe_2$*, Physical Review B 72(3) (2005)

[Per05]   Persson C., Zhao Y.J., Lany S., Zunger A., *n-type doping of $CuInSe_2$ and $CuGaSe_2$*, Physical Review B 72(3) (2005) 035211.

[Pis09]   Pistor P., Caballero R., Hariskos D., Izquierdo-Roca V., Wachter R., Schorr S., Klenk R., *Quality and stability of compound indium sulphide as source material for buffer layers in $Cu(In,Ga)Se_2$ solar cells*, Solar Energy Materials and Solar Cells 93(1) (2009) 148-152.

[Pla03]   Platzer-Björkman C., Lu J., Kessler J., Stolt L., *Interface study of $CuInSe_2/ZnO$ and $Cu(In,Ga)Se_2/ZnO$ devices using ALD ZnO buffer layers*, Thin Solid Films 431 (2003) 321-325.

[Poo06]   Poortmans J., Arkhipov V., *Thin Film Solar Cells: Fabrication, Characterization and Applications,* John Wiley and Sons Ltd., Chichester (2006).

[Pud05]   Pudov A.O., Kanevce A., Al-Thani H.A., Sites J.R., Hasoon F.S., *Secondary barriers in $CdS-CuIn_{1-x}Ga_xSe_2$ solar cells*, Journal of Applied Physics 97(6) (2005) 064901.

[Pue96]   Puech K., Zott S., Leo K., Ruckh M., Schock H.W., *Determination of minority carrier lifetimes in $CuInSe_2$ thin films*, Applied Physics Letters 69(22) (1996) 3375-3377.

[Ram03a] Ramanathan K., Contreras M.A., Perkins C.L., Asher S., Hasoon F.S., Keane J., Young D., Romero M., Metzger W., Noufi R., Ward J., Duda A., *Properties of 19.2% efficiency ZnO/CdS/CuInGaSe$_2$ thin-film solar cells*, Progress in Photovoltaics 11(4) (2003) 225-230.

[Ram03b] Ramanathan K., Hasoon F.S., Smith S., Young D.L., Contreras M.A., Johnson P.K., Pudov A.O., Sites J.R., *Surface treatment of CuInGaSe$_2$ thin films and its effect on the photovoltaic properties of solar cells*, Journal of Physics and Chemistry of Solids 64(9-10) (2003) 1495-1498.

[Rau99a] Rau U., Braunger D., Herberholz R., Schock H.W., Guillemoles J.F., Kronik L., Cahen D., *Oxygenation and air-annealing effects on the electronic properties of Cu(In,Ga)Se$_2$ films and devices*, Journal of Applied Physics 86(1) (1999) 497-505.

[Rau99b] Rau U., Schock H.W., *Electronic properties of Cu(In,Ga)Se$_2$ heterojunction solar cells- recent achievements, current understanding, and future challenges*, Applied Physics A-Materials Science & Processing 69(2) (1999) 131-147.

[Rau09] Rau U., Taretto K., Siebentritt S., *Grain boundaries in Cu(In,Ga)(Se,S)$_2$ thin-film solar cells*, Applied Physics A-Materials Science & Processing 96(1) (2009) 221-234.

[Rec00] Rechid J., Kampmann A., Reineke-Koch R., *Characterising superstrate CIS solar cells with electron beam induced current*, Thin Solid Films 361 (2000) 198-202.

[Rec01] Rechid J., Reineke-Koch R., *Determining the sheet resistance of superstrate CIS-solar cells by planar electron beam induced current measurements*, Thin Solid Films 387(1-2) (2001) 243-245.

[Reg04] Rega N., *Photolumineszenz von epitaktischen Cu(In,Ga)Se$_2$-Schichten,* PhD-thesis, Freie Universiät, Berlin (2004).

[Reg05] Rega N., Siebentritt S., Albert J., Nishiwaki S., Zajogin A., Lux-Steiner M.C., Kniese R., Romero M.J., *Excitonic luminescence of Cu(In,Ga)Se$_2$*, Thin Solid Films 480 (2005) 286-290.

[Rei10] Reislöhner U., Metzner H., Ronning C., *Hopping Conduction Observed in Thermal Admittance Spectroscopy*, Physical Review Letters 104(22) (2010) 226403.

[Rei02] Reiß J., *Generation und Rekombination von Ladungsträgern in CuInS$_2$-basierten Dünnschicht-Solarzellen,* PhD-Thesis, Freie Universität Berlin, Berlin (2002).

[Rep08] Repins I., Contreras M.A., Egaas B., DeHart C., Scharf J., Perkins C.L., To B., Noufi R., *19.9%-efficient ZnO/CdS/CuInGaSe$_2$ solar cell with 81.2% fill factor*, Progress in Photovoltaics 16(3) (2008) 235-239.

[Rep06] Repins I.L., Stanbery B.J., Young D.L., Li S.S., Metzger W.K., Perkins C.L., Shafarman W.N., Beck M.E., Chen L., Kapur V.K., Tarrant D., Gonzalez M.D., Jensen D.G., Anderson T.J., Wang X., Kerr L.L., Keyes B., Asher S., Delahoy A., Von Roedern B., *Comparison of device performance and measured transport parameters in widely-varying Cu(In,Ga)(Se,S)$_2$ solar cells*, Progress in Photovoltaics 14(1) (2006) 25-43.

[Ren10] Renewable Energy Policy Network for the 21st Century, *Renewables 2010 - Global Status Report*, from:
http://www.ren21.net/Portals/97/documents/GSR/REN21_GSR_2010_full_revised%20Sept2010.pdf.

[Ris09] Rissom T., personal communication (2009).

[Roc91]   Rockett A., Birkmire R.W., *CuInSe$_2$ for photovoltaic applications*, Journal of Applied Physics 70(7) (1991) R81-R97.

[Roc03]   Rockett A., Liao D., Heath J.T., Cohen J.D., Strzhemechny Y.M., Brillson L.J., Ramanathan K., Shafarman W.N., *Near-surface defect distributions in Cu(In,Ga)Se$_2$*, Thin Solid Films 431 (2003) 301-306.

[Rom03a]   Romero M.J., Ramanathan K., Contreras M.A., Al-Jassim M.M., Noufi R., Sheldon P., *Cathodoluminescence of Cu(In,Ga)Se$_2$ thin films used in high-efficiency solar cells*, Applied Physics Letters 83(23) (2003) 4770-4772.

[Rom03b]   Romero M.J., Jones K.M., AbuShama J., Yan Y., Al-Jassim M.M., Noufi R., *Surface-layer band gap widening in Cu(In,Ga)Se$_2$ thin films*, Applied Physics Letters 83(23) (2003) 4731-4733.

[Rud05]   Rudmann D., Bremaud D., Zogg H., Tiwari A.N., *Na incorporation into Cu(In,Ga)Se$_2$ for high-efficiency flexible solar cells on polymer foils*, Journal of Applied Physics 97(8) (2005) 084903.

[Rus09]   Rusu M., Bär M., Lehmann S., Sadewasser S., Weinhardt L., Kaufmann C.A., Strub E., Röhrich J., Bohne W., Lauermann I., Jung C., Heske C., Lux-Steiner M.C., *Three-dimensional structure of the buffer/absorber interface in CdS/CuGaSe$_2$ based thin film solar cells*, Applied Physics Letters 95(17) (2009) 173502.

[Sad03]   Sadewasser S., Ishii K., Glatzel T., Lux-Steiner M.C., *Electronic surface properties of ultrahigh vacuum grown polycrystalline CuGaSe$_2$*, Polycrystalline Semiconductors VII, Proceedings 93 319-324, Trans Tech Publications Ltd, Zurich-Uetikon (2003).

[Sah57]   Sah C.T., Noyce R.N., Shockley W., *Carrier generation and recombination in p-n junctions and p-n junction characteristics*, Proceedings of the Institute of Radio Engineers 45(9) (1957) 1228-1243.

[Sch18]   Scherrer P., *Bestimmung der Größe und der inneren Struktur von Kolloidteilchen mittels Röntgenstrahlen*, Nachrichten von der Gesellschaft der Wissenschaften zu Göttingen 2 (1918) 98&.

[Sch91]   Schmid D., Jäger-Waldau G.J., Schock H.W., *Diffusion length measurements and modeling of CuInSe$_2$-(Zn,Cd)S solar cells*, 10th European Photovoltaic Solar Energy Conference, Lisbon, (1991) 935-938.

[Sch93]   Schmid D., Ruckh M., Grunwald F., Schock H.W., *Chalcopyrite defect chalcopyrite heterojunctions on the basis of CuInSe$_2$*, Journal of Applied Physics 73(6) (1993) 2902-2909.

[Sch96]   Schmid D., Ruckh M., Schock H.W., *A comprehensive characterization of the interfaces in Mo/CIS/CdS/ZnO solar cell structures*, Solar Energy Materials and Solar Cells 41-2 (1996) 281-294.

[Sch92]   Schmidt T., Lischka K., Zulehner W., *Excitation-power dependence of the near-band-edge photoluminescence of semiconductors*, Physical Review B 45(16) (1992) 8989-8994.

[Sch00a]   Schmitt M., Rau U., Parisi J., *Charge carrier transport via defect states in Cu(In,Ga)Se$_2$ thin films and Cu(In,Ga)Se$_2$/CdS/ZnO heterojunctions*, Physical Review B 61(23) (2000) 16052-16059.

[Sch98]   Schön J.H., Arushanov E., Kulyuk L.L., Micu A., Shaban D., Tezlevan V., *Electrical and optical characterization of ion-implanted CuGaSe$_2$ single crystals*, Journal of Applied Physics 84(3) (1998) 1274-1278.

[Sch99]   Schön J.H., Oestreich J., Schenker O., Riazi-Nejad H., Klenk M., Fabre N., Arushanov E., Bucher E., *n-type conduction in Ge-doped CuGaSe$_2$*, Applied Physics Letters 75(19) (1999) 2969-2971.

[Sch00b]   Schön J.H., *Extrinsic doping of CuGaSe$_2$ single crystals*, Journal of Physics D-Applied Physics 33(3) (2000) 286-291.

[Sch04]   Schulmeyer T., Hunger R., Klein A., Jaegermann W., Niki S., *Photoemission study and band alignment of the CuInSe$_2$(001)/CdS heterojunction*, Applied Physics Letters 84(16) (2004) 3067-3069.

[Sey11]   Seyrling S., Chirila A., Güttler D., Blösch P., Pianezzi F., Verma R., Bücheler S., Nishiwaki S., Romanyuk Y.E., Rossbach P., Tiwari A.N., *CuIn$_{1-x}$Ga$_x$Se$_2$ growth process modifications: Influences on microstructure, Na distribution, and device properties*, Solar Energy Materials and Solar Cells 95(6) (2011) 1477-1481.

[Sha75]   Shay J.L., Wermick J.H., *Ternary Chalcopyrite Semiconductors: Growth, Electronic Properties, and Applications,* Pergamon Press, (1975).

[Shi06]   Shimakawa S., Kitani K., Hayashi S., Satoh T., Hashimoto Y., Takahashi Y., Negami T., *Characterization of Cu(In,Ga)Se$_2$ thin films by time-resolved photoluminescence*, Physica Status Solidi A-Applications and Materials Science 203(11) (2006) 2630-2633.

[Shi08]   Shimakawa S., Hashimoto Y., Hayashi S., Satoh T., Negami T., *Annealing effects on Zn$_{1-x}$Mg$_x$O/CIGS interfaces characterized by ultraviolet light excited time-resolved photoluminescence*, Solar Energy Materials and Solar Cells 92(9) (2008) 1086-1090.

[Shi07]   Shirakata S., Nakada T., *Time-resolved photoluminescence in Cu(In,Ga)Se$_2$ thin films and solar cells*, Thin Solid Films 515(15) (2007) 6151-6154.

[Shk84]   Shklovskii B.I., Efros A.L., *Electronic properties of doped semiconductors,* Springer-Verlag, Berlin (1984).

[Sie02]   Siebentritt S., *Wide gap chalcopyrites: material properties and solar cells*, Thin Solid Films 403 (2002) 1-8.

[Sie03]   Siebentritt S., Schuler S., *Defects and transport in the wide gap chalcopyrite CuGaSe$_2$*, Journal of Physics and Chemistry of Solids 64(9-10) (2003) 1621-1626.

[Sie04a]   Siebentritt S., *Alternative buffers for chalcopyrite solar cells*, Solar Energy 77(6) (2004) 767-775.

[Sie04b]   Siebentritt S., Rega N., Zajogin A., Lux-Steiner M.C., *Do we really need another PL study of CuInSe$_2$?*, Physica Status Solidi C 1(9) (2004) 2304-2310.

[Sie05a]   Siebentritt S., *Hole transport mechanisms in CuGaSe$_2$*, Thin Solid Films 480 (2005) 312-317.

[Sie05b]   Siebentritt S., Beckers I., Riemann T., Christen J., Hoffmann A., Dworzak M., *Reconciliation of luminescence and Hall measurements on the ternary semiconductor CuGaSe$_2$*, Applied Physics Letters 86(9) (2005) 091909.

[Sie06]   Siebentritt S., Papathanasiou N., Lux-Steiner M.C., *Potential fluctuations in compensated chalcopyrites*, Physica B-Condensed Matter 376 (2006) 831-833.

[Sie10]   Siebentritt S., Igalson M., Persson C., Lany S., *The electronic structure of chalcopyrites-bands, point defects and grain boundaries*, Progress in Photovoltaics 18(6) (2010) 390-410.

[Sie11]   Siebentritt S., *What limits the efficiency of chalcopyrite solar cells?*, Solar Energy Materials and Solar Cells 95(6) (2011) 1471-1476.

[Slo10]   Slobodskyy A., Slobodskyy T., Ulyanenkova T., Doyle S., Powalla M., Baumbach T., Lemmer U., *In-depth analysis of the $CuIn_{1-x}Ga_xSe_2$ film for solar cells, structural and optical characterization*, Applied Physics Letters 97(25) (2010) 251911.

[Sol11]   Solar Frontier, *Solar Frontier Sets New Efficiency Record in Thin-Film CIS Technology*, from: http://www.solar-frontier.com/news/109.

[Str62]   Stratton R., *Diffusion of Hot and Cold Electrons in Semiconductor Barriers*, Physical Review 126(6) (1962) 2002-2014.

[Str02]   Strzhemechny Y.M., Smith P.E., Bradley S.T., Liao D.X., Rockett A.A., Ramanathan K., Brillson L.J., *Near-surface electronic defects and morphology of $CuIn_{1-x}Ga_xSe_2$*, Journal of Vacuum Science & Technology B 20(6) (2002) 2441-2448.

[Sug08]   Sugiyama M., Kinoshita A., Miyama A., Nakanishi H., Chichibu S.F., *Formation of Zn-doped $CuInSe_2$ films by thermal annealing using dimethylzinc*, Journal of Crystal Growth 310(4) (2008) 794-797.

[Sug00]   Sugiyama T., Chaisitsak S., Yamada A., Konagai M., Kudriavtsev Y., Godines A., Villegas A., Asomoza R., *Formation of pn homojunction in Cu(InGa)Se_2 thin film solar cells by Zn doping*, Japanese Journal of Applied Physics Part 1-Regular Papers Short Notes & Review Papers 39(8) (2000) 4816-4819.

[Sze81]   Sze S.M., *Physics of Semiconductor Devices,* John Wiley & Sons, New York (1981).

[Tel72]   Tell B., Shay J.L., Kasper H.M., *Room-temperature electrical properties of 10 I-III-VI$_2$ semiconductors*, Journal of Applied Physics 43(5) (1972) 2469-2470.

[Tel76]   Tell B., Wagner S., Bridenbaugh P.M., *Motion of p-n-junctions in $CuInSe_2$*, Applied Physics Letters 28(8) (1976) 454-455.

[Tot98]   Toth M., Phillips M.R., *Monte Carlo modeling of cathodoluminescence generation using electron energy loss curves*, Scanning 20(6) (1998) 425-432.

[Tra88]   Trahey G.E., Hubbard S.M., Vonramm O.T., *Angle independent ultrasonic blood-flow detection by frame-to-frame correlation of b-mode images*, Ultrasonics 26(5) (1988) 271-276.

[Tur01]   Turcu M., Kötschau I.M., Rau U., *Band alignments in the Cu(In,Ga)(S,Se)$_2$ alloy system determined from deep-level defect energies*, Applied Physics A-Materials Science & Processing 73(6) (2001) 769-772.

[Wag98]   Wagner M., Dirnstorfer I., Hofmann D.M., Lampert M.D., Karg F., Meyer B.K., *Characterization of CuIn(Ga)Se_2 thin films - I. Cu-rich layers*, Physica Status Solidi a-Applied Research 167(1) (1998) 131-142.

[Wan09]   Wang L., Fu Y., *Sample Preparation for Transmission Electron Microscopy using a Focused Ion Beam*, Ion Beams in Nanoscience and Technology Springer Verlag, Berlin Heidelberg (2009).

[War90]   Warren B.E., *X-ray diffraction,* Dover Publications, Mineola (1990).

[Web07]   Weber A., Kötschau I., Schock H.W., *Monitoring In-Ga interdiffusion during chalcopyrite fortuation in Ga_xS_y-(Cu,In) photovoltaic precursor layers*, Thin Solid Films 515(15) (2007) 6252-6255.

[Wei95]   Wei S.H., Zunger A., *Band offsets and optical bowing of chalcopyrites and Zn-based II-VI alloys*, Journal of Applied Physics 78(6) (1995) 3846-3856.

[Wei03]   Weinhardt L., Bär M., Muffler H., Fischer C.H., Lux-Steiner M.C., Niesen T.P., Karg F., Gleim T., Heske C., Umbach E., *Impact of Cd^{2+}-treatment on the band alignment at the ILGAR-ZnO/CuIn(S,Se)$_2$ heterojunction*, Thin Solid Films 431 (2003) 272-276.

[Wer88]   Werner J.H., *Schottky Barrier and pn-Junction I/V plots - Small-Signal Evaluation*, Applied Physics a-Materials Science & Processing 47(3) (1988) 291-300.

[Wer05]   Werner J.H., Mattheis J., Rau U., *Efficiency limitations of polycrystalline thin film solar cells: case of $Cu(In,Ga)Se_2$*, Thin Solid Films 480-481 (2005) 399-409.

[Wil09]   Williams D.B., Carter C.B., *Transmission electron microscopy: a textbook for materials science, part 1 to 4,* Springer Science and Business Media, New York (2009).

[Win09]   Windeln J., Schock H.W., Felser C., Metzner H., Mannstadt W., Klenk R., Gruhn T., Kaufmann C.A., Rudigier-Voigt E., Speit B., Haag M., Rissom T., Kieven D., Ludwig C., Haarstrich J., Oertel M., *comCIGS - integrative framework of experimental and virtual lab*, 24th EU PVSEC Hamburg, (2009) 2443-2445.

[Yac86]   Yacobi B.G., Holt D.B., *Catholuminescence scanning electron-microscopy of semiconductors*, Journal of Applied Physics 59(4) (1986) R1-R24.

[Yac90]   Yacobi B.G., Holt D.B., *Cathodoluminescence Microscopy of Inorganic Solids,* Plenum Press, New York (1990).

[Yak94]   Yakushev M.V., Neumann H., Tomlinson R.D., Rimmer P., Lippold G., *Influence of proton implantation on the properties of $CuInSe_2$ single-crystals (II)*, Crystal Research and Technology 29(3) (1994) 417-426.

[Yan02]   Yan Y., Jones K.M., Abushama J., Young M., Asher S., Al-Jassim M.M., Noufi R., *Microstructure of surface layers in $Cu(In,Ga)Se_2$ thin films*, Applied Physics Letters 81(6) (2002) 1008-1010.

[Yos98]   Yoshino K., Shimizu T., Fukuyama A., Maeda K., Fons P.J., Yamada A., Niki S., Ikari T., *Temperature dependence of photoacoustic spectra in $CuInSe_2$ thin films grown by molecular beam epitaxy*, Solar Energy Materials and Solar Cells 50(1-4) (1998) 127-132.

[Yos00]   Yoshino K., Yokoyama H., Maeda K., Ikari T., *Crystal growth and photoluminescence of $CuIn_xGa_{1-x}Se_2$ alloys*, Journal of Crystal Growth 211(1-4) (2000) 476-479.

[Yu75a]   Yu P.W., Faile S.P., Park Y.S., *Cadmium-diffused $CuInSe_2$ junction diode and photovoltaic detection*, Applied Physics Letters 26(7) (1975) 384-385.

[Yu75b]   Yu P.W., Park Y.S., Faile S.P., Ehret J.E., *Electroluminescence and photovoltaic detection in Cd-implanted $CuInSe_2$ p-n-junction diodes*, Applied Physics Letters 26(12) (1975) 717-719.

[Yu76a]   Yu P.W., *Radiative recombination in melt-grown and Cd-implanted $CuInSe_2$*, Journal of Applied Physics 47(2) (1976) 677-684.

[Yu76b]   Yu P.W., Park Y.S., Grant J.T., *Electroluminescence in Br-implanted, Cl-implanted, and Zn-implanted $CuInSe_2$ p-n-junction diodes*, Applied Physics Letters 28(4) (1976) 214-216.

[Zac11]   Zachmann H., Puttnins S., Yakushev M.V., Luckert F., Martin R.W., Karotki A.V., Gremenok V.F., Mudryi A.V., *Fabrication and characterisation of Cu(In,Ga)Se$_2$ solar cells on polyimide*, Thin Solid Films (2011) doi: 10.1016/j.tsf.2010.1012.1211.

[Zar89]   Zarem H.A., Lebens J.A., Nordstrom K.B., Sercel P.C., Sanders S., Eng L.E., Yariv A., Vahala K.J., *Effect of Al mole fraction on carrier diffusion lengths and lifetimes in Al$_x$Ga$_{1-x}$As*, Applied Physics Letters 55(25) (1989) 2622-2624.

[Zeg95]   Zegadi A., Alsaffar I.S., Yakushev M.V., Tomlinson R.D., *Photoacoustic-spectroscopy use in the analysis of ion-implanted CuInSe$_2$ single-crystals*, Review of Scientific Instruments 66(8) (1995) 4095-4101.

[Zha98]   Zhang S.B., Wei S.H., Zunger A., Katayama-Yoshida H., *Defect physics of the CuInSe$_2$ chalcopyrite semiconductor*, Physical Review B 57(16) (1998) 9642-9656.

[Zie03]   Ziegler J.F., Biersack J.P., Littmark U., *The stopping and range of ions in solids*, Pergamon, New York (2003).

[Zot97]   Zott S., Leo K., Ruckh M., Schock H.W., *Radiative recombination in CuInSe$_2$ thin films*, Journal of Applied Physics 82(1) (1997) 356-367.

Appendix
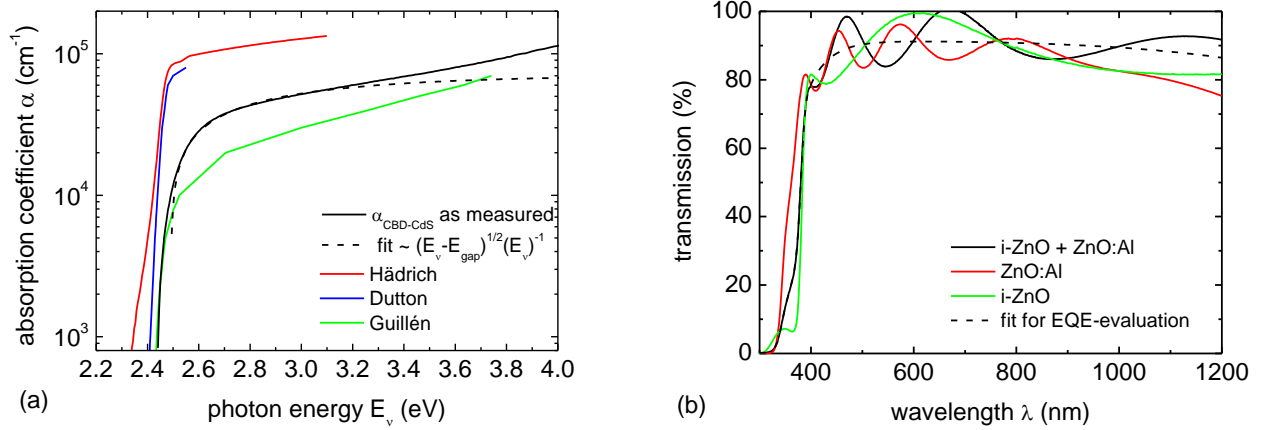
Figure A1: (a) Absorption coefficient of CdS as measured on the CBD-CdS used in this study and compared to the literature values for CBD-CdS [Gui98], single-crystalline CdS [Dut58] and CdS deposited by close-space sublimation (CSS) [Häd09]. The measured data are fitted according to the absorption relation for direct semiconductors [Mos59]; the band-gap is determined to 2.491±0.001 *eV*. (b) Transmission spectra of an intrinsic and an Al-doped ZnO layer and of the commonly used double-layer. The band-gaps are determined to 3.20±0.10 *eV* (i-ZnO) and 3.41±0.12 *eV* (ZnO:Al) (larger due to Burstein-Moss-shift [Bur54; Mos54]). The transmission spectrum of the double-layer is fitted (ignoring the interferences) for *EQE*-evaluations (dashed line).
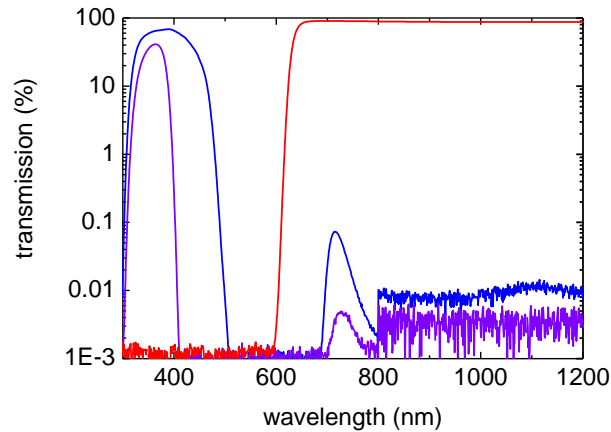
Figure A2: Transmission spectra of the optical filters used for blue-bias illumination in the *EQE*-measurements for cells with CdS (blue line – combination of Schott Color Glass BG3 and S8612) and without CdS (violet line – combination of Schott Color Glass UG1 and S8612) buffer layer and red-bias illumination (Schott Color Glass RG630). The transmission at wavelengths above 500 *nm* is reduced by at least a factor of 10^3.

(a)

(b)
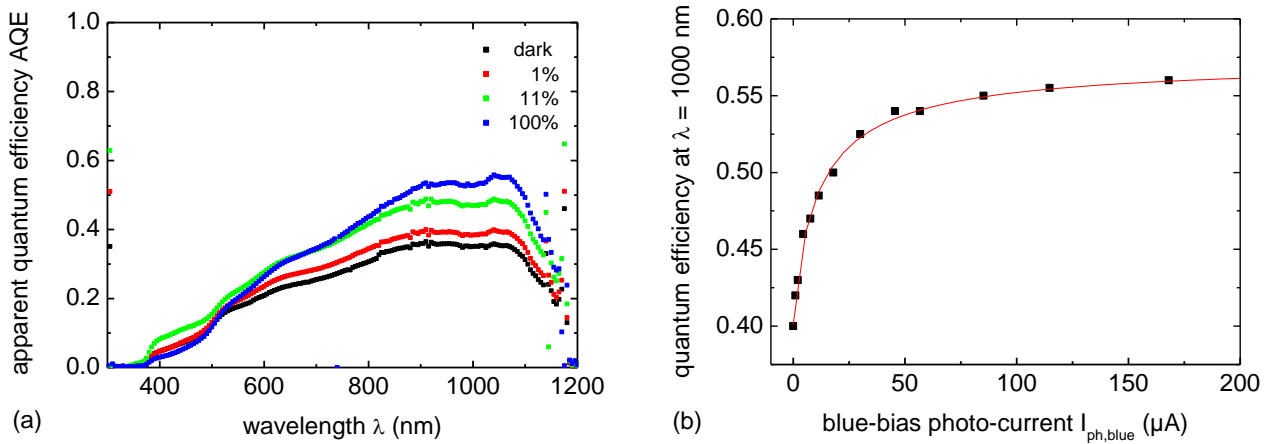
Figure A3: (a) *AQE*-spectra of a solar cell made from Cd-implanted absorbers with CdS buffer layer under blue-light bias of different intensities. The increase of the quantum efficiency is commonly interpreted to be due to meta-stable defects in the buffer layer, which lead to an higher effective doping level if light is absorbed in the buffer (photo-doping) [Eis98; Kön02; Glo04]. This may lead to both reduced interface recombination and an enlarged SCR width. The latter effect causes an increase of the *IQE* especially in the long-wavelength region. **(b)** *AQE* at $\lambda = 1000$ *nm* as a function of the blue-bias light intensity (represented by the blue-light photo-current $I_{ph,blue}$ induced in the cell); an increase from 0.4 in the dark to 0.56 is measured. It is concluded that blue-bias light is needed to obtain the *EQE* as active under real working conditions (AM1.5 illumination).

(a)

(b)
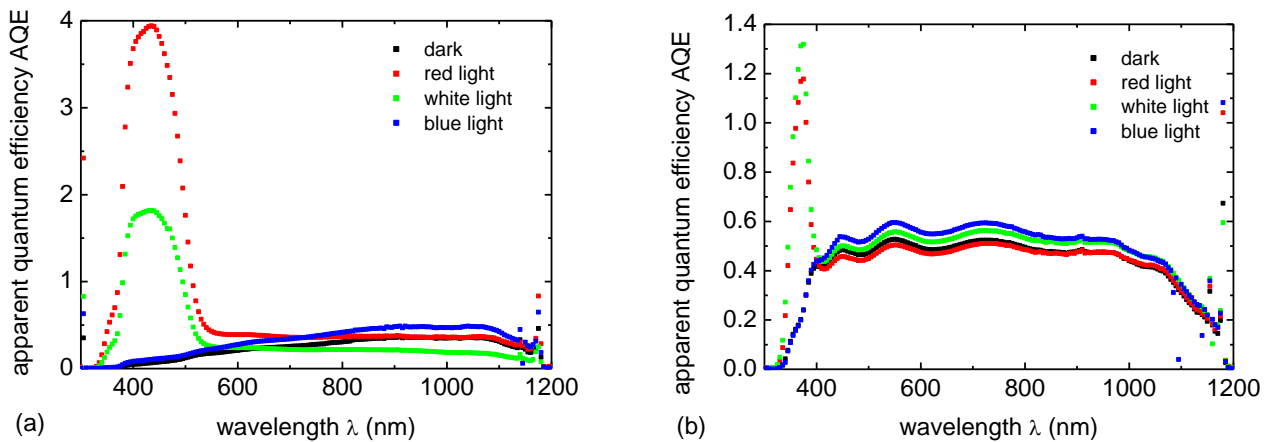
Figure A4: *AQE*-spectra of Cd-implanted devices without defect annealing with **(a)** and without **(b)** CdS buffer layer under different illumination conditions (transmission of the filters see Figure A2, intensity equivalent to 11% AM1.5). The slightly increased collection under blue-light bias shown in Figure A3 may also lead to an apparent increase of the *AQE* in the region of absorption in the CdS and i-ZnO (see Figure A1), respectively, if red-light bias is used. The photo-doping is now caused by the spectral light, when the spectral light is in the absorption range of the CdS and i-ZnO, respectively. This leads to a periodical modulation of the bias-generated photo-current with the chopping frequency of the spectral light, which will be registered by the lock-in amplifier in addition to the direct spectral photo-current. Both effects are superimposed if white bias-light is used. Such an enormous *AQE*-effect has been described in the literature under forward bias only [Eng99; Kön02; Glo04]; at 0 *V*, only a slight increase is observed for standard cells [Glo04]. This strong *AQE* at 0 *V* in these cells may be due to the poor collection properties of the cells, which allow for the large, real improvements of the *IQE* under blue-light bias. The occurrence of the *AQE*-effect also in a cell without CdS buffer can only be explained by photo-doping effects in the i-ZnO in terms of this model.
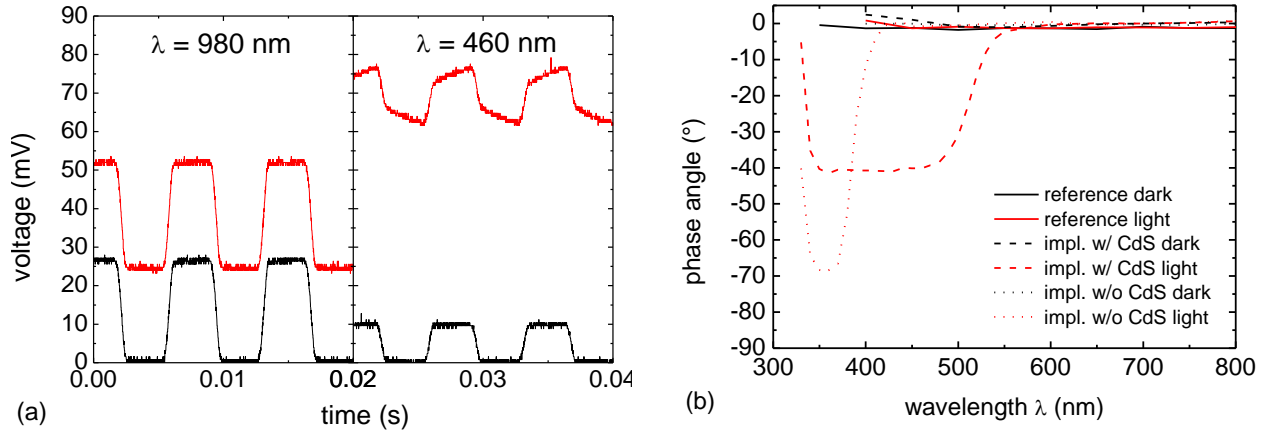
Figure A5: The strong *AQE*-effect under red-light bias is illustrated in this figure by a careful analysis of the photo-current signal. In part (a), the input-signal of the lock-in amplifier is plotted as a function of time for the cell measured in Figure A4 and under very weak red-light bias for two different spectral wavelengths as measured with an oscilloscope. The black lines represent the signal without and the red lines with bias illumination. The shape of both black lines is determined by the chopper modulation of the light beam. Switching on the red-light bias, leads to a shift of the whole signal to higher photo-currents at $\lambda = 980$ *nm* – the bias-induced photo-current is constant over time as it is supposed to be and will not be registered by the lock-in. At $\lambda = 460$ *nm*, the shift is significantly larger at the same bias-intensity and the shape of the signal is changes additionally. The stronger shift can be understood when considering the increase of the *AQE* described in Figure A3. The changes in signal-shape point towards slow capture and emission processes taking part in photo-doping. Lifetimes in the order of 100 *ms* are measured. The distortion of the signals also leads to a de-synchronization of the input signals coming from the cell (photo-current) and directly from the chopper at the lock-in amplifier. This can be measured as a shift of the phase angle as plotted in part (b) of this figure for different cells and bias illumination.

A: General device properties			Front	Back	
barrier height $\Delta\phi_{bn} = E_C - E_F$, $\Delta\phi_{bp} = E_F - E_V$	$\Delta\phi_b$	eV	$\Delta\phi_{bn} = 0$	$\Delta\phi_{bp} = 0.2$	
electron/hole thermal velocities	$s_{e/h}$	$cm\ s^{-1}$	10^7	10^7	
reflectivity	R		0.05	0.8	
B: Layer properties			**ZnO**	**CdS**	**Cu(In,Ga)Se$_2$**
layer thickness	d	nm	200	50	3000
relative permittivity	$\varepsilon/\varepsilon_0$		9	10	13.6
electron mobility	μ_e	$cm^2\ V^1\ s^{-1}$	100	100	100
hole mobility	μ_h	$cm^2\ V^{-1}s^{-1}$	25	25	25
carrier concentration	$N_{D/A}$	cm^{-3}	N_D: 1 10^{18}	N_D: 1.1 10^{18}	N_A: 2 10^{16}
band-gap energy	E_{gap}	eV	3.3	2.4	1.15
conduction band density of states	N_C	cm^{-3}	2.2 10^{18}	2.2 10^{18}	2.2 10^{18}
valence band density of states	N_V	cm^{-3}	1.8 10^{19}	1.8 10^{19}	1.8 10^{19}
electron affinity	χ_e	eV	4.0	3.8	4.1
C: Gaussian-distributed defect states			**ZnO**	**CdS**	**Cu(In,Ga)Se$_2$**
donor/acceptor defects density	N_{DG}, N_{AG}	cm^{-3}	N_{DG}: 1 10^{17}	N_{AG}: 1 10^{18}	N_{DG}: 1 10^{14}
defect mean energy	E_{DG}, E_{AG}	eV	mid-gap	mid-gap	mid-gap
defect distribution width	w_G	eV	0.1	0.1	0.1
electron capture cross-section	σ_e	cm^2	1 10^{-12}	1 10^{-17}	5 10^{-13}
hole capture cross-section	σ_h	cm^2	1 10^{-15}	1 10^{-12}	1 10^{-15}

Table A1: Baseline case parameter set adapted from [Glo05a] for the SCAPS simulations in Sections 5.5.1 and 4.1. Deviations from this set are mentioned in the text.

	j_{sc} (mA cm^{-2})	V_{oc} (mV)	FF (%)	η (%)	R_{sh} (kΩcm^2)	R_s (Ωcm^2)	n_{id}	j_0 (mA cm^{-2})
Ref (B1)	31.2(8)	0.582(4)	0.68(1)	12.4(4)	0.8(3)	0.14(1)	2.01(9)	4.8(2.3) 10^{-4}
Cd (B1)	29.3(9)	0.607(3)	0.60(2)	10.7(5)	0.3(1)	0.18(1)	2.3 (2)	1.1(0.8) 10^{-3}
Zn (B1)	31.4(4)	0.592(3)	0.69(1)	12.9(2)	0.6(2)	0.15(3)	1.94(8)	2.4(1.2) 10^{-4}
Mg (B1)	30.8(9)	0.431(9)	0.58(2)	7.8(7)	0.3(1)	0.16(4)	2.5 (2)	4.1(2.5) 10^{-2}
Ref (C1)	31.4(4)	0.592(3)	0.69(1)	12.9(2)	0.7(2)	0.15(3)	1.94(8)	2.4(1.2) 10^{-4}
Cd (C1)	31.9(4)	0.534(9)	0.67(2)	11.4(8)	0.8(3)	0.14(1)	1.9 (1)	7.6(5.2) 10^{-4}
Zn (C1)	30.5(3)	0.451(5)	0.57(1)	7.8(2)	0.3(1)	0.16(1)	2.69(4)	4.5(0.8) 10^{-2}
Mg (C1)	28.3(6)	0.344(9)	0.45(1)	4.3(2)	0.09(1)	0.17(2)	3.65(9)	6.6(1.1) 10^{-1}

Table A2: Solar cell parameters determined from a set of eight cells made from Cd-, Zn- and Mg-implanted absorbers with CdS buffer layer after annealing according to procedure B1 and C1, respectively. The parameters of the corresponding reference cells are listed for comparison.

	j_{sc} (mA cm^{-2})	V_{oc} (mV)	FF (%)	η (%)	R_{sh} (kΩcm^2)	R_s (Ωcm^2)	n_{id}	j_0 (mA cm^{-2})
Ref (B1)	23(1)	0.39(1)	0.47(2)	4.1(0.4)	0.08(1)	0.15(1)	2.55(5)	4.4(1.6) 10^{-2}
Cd (B1)	8(4)	0.55(3)	0.41(7)	2.0(1.3)	0.16(2)	0.07(2)	1.8 (1)	4.3(7.6) 10^{-5}
Zn (B1)	21(4)	0.53(3)	0.44(7)	4.9(1.7)	0.08(4)	0.09(2)	2.1 (2)	1.0(1.6) 10^{-3}
Mg (B1)	7(2)	0.37(2)	0.29(5)	0.8(0.4)	0.06(1)	0.10(3)	2.7 (2)	4.5(4.3) 10^{-3}
Ref (C1)	17(1)	0.37(1)	0.37(3)	2.3(0.3)	0.04(1)	0.17(1)	2.34(4)	1.7(0.3) 10^{-2}
Cd (C1)	23(1)	0.56(2)	0.54(9)	7.1(1.4)	0.12(5)	0.09(2)	1.8 (2)	1.9(2.2) 10^{-4}
Zn (C1)	19(1)	0.35(4)	0.51(3)	3.3(0.5)	0.14(5)	0.11(4)	3.0 (3)	2.8(1.5) 10^{-1}
Mg (C1)	16(1)	0.12(2)	0.38(2)	0.9(0.1)	0.03(1)	0.35(3)	2.3 (1)	1.4(0.4) 10^{0}

Table A3: Solar cell parameters determined from a set of eight cells made from Cd-, Zn- and Mg-implanted absorbers without buffer layer after annealing according to procedure B1 and C1, respectively. The parameters of the corresponding reference cells are listed for comparison.

	j_{sc} (mA cm^{-2})	V_{oc} (mV)	FF (%)	η (%)	R_{sh} (kΩcm^2)	R_s (Ωcm^2)	n_{id}	j_0 (mA cm^{-2})
Ref (B1)	28.6(5)	0.41(2)	0.52(5)	6.1(0.9)	0.12(6)	0.18(1)	2.41(6)	3.4(1.4) 10^{-2}
Cd (B1)	12 (4)	0.54(3)	0.41(11)	2.9(1.7)	0.10(4)	0.08(1)	1.9 (1)	1.4(1.4) 10^{-4}
Zn (B1)	26.1(9)	0.52(2)	0.43(9)	5.9(1.5)	0.08(4)	0.11(1)	2.3 (3)	3.3(3.9) 10^{-3}
Mg (B1)	9 (2)	0.35(6)	0.31(5)	1.0(0.5)	0.06(1)	0.11(2)	2.9 (2)	1.6(1.3) 10^{-2}
Ref (C1)	27.1(9)	0.41(1)	0.46(5)	5.1(0.7)	0.06(2)	0.17(2)	2.45(6)	3.0(6.4) 10^{-2}
Cd (C1)	28.0(6)	0.55(1)	0.58(7)	9.0(1.3)	0.17(9)	0.09(2)	2.0 (2)	7.4(7.0) 10^{-4}
Zn (C1)	22 (1)	0.36(3)	0.51(4)	3.9(0.7)	0.15(7)	0.11(5)	3.0 (3)	2.4(1.9) 10^{-1}
Mg (C1)	16 (1)	0.19(2)	0.36(2)	1.1(0. 1)	0.03(1)	0.47(2)	3.4 (3)	1.5(0.3) 10^{0}

Table A4: Solar cell parameters determined from a set of eight cells made from Cd-, Zn- and Mg-implanted absorbers without buffer layer after annealing according to procedure B1 and C1, respectively, and after post-annealing. The parameters of the corresponding reference cells are listed for comparison.

List of figures

List of tables

List of symbols and abbreviations

Symbols

A_{ill}	illuminated area
A	average atomic mass of a sample
A_G	relative shading of the grid
$A_{ZnO}, A_{inv}, \ldots$	absorptance of the respective layers
AQE	apparent quantum efficiency
$a_{ballistic}$	free ballistic acceleration
$a_{e,h}$	Bohr-radius of electron or holes
$a_{eff,max}$	maximum effective acceleration
d	layer thickness
d_{inv}	inversion layer thickness
D	diffusion coefficient
D_{crit}	critical diffusion coefficient
e	elementary charge
E	electric field
E_1, E_2, E_3	emission energies observed in band-gap graded $Cu(In,Ga)Se_2$ assigned to regions of different GGI
E_A	ionization energy of acceptor defects
E_{BB}	band-to-band recombination energy
E_{BX}	bound-exciton binding energy
E_{be}	average energy of backscattered electrons
E_C	conduction band energy
E_D	ionization energy of donor defects
E_{DA}	donor-acceptor pair transition energy
E_{DG}, E_{AG}	mean energy of Gaussian defects
E_{DL}	energy of recombination via deep-levels in the band-gap
E_{detect}	CL detection energy in monochromatic imaging
E_e	electron energy

E_{EHP}	average energy needed for e-h-pair generation
E_{Fn}	electron quasi-Fermi level
E_{Fp}	hole quasi-Fermi level
E_{FX}	free-exciton binding energy
E_{gap}	band-gap
$E_{gap,min}$	minimum band-gap energy in the graded layer
E_{qDAP}	qDAP transition energy
E_{qe}	quasi-electric field
E_V	valence band energy
E_{Vac}	vacuum level energy
EQE	external quantum efficiency
EQE_{CL}	external quantum efficiency of cathodoluminescence
E_ν	photon energy
FF	fill factor
f_R	loss factor of EQE_{CL} due to reflections
G_0	number of e-h-pairs excited by one incident electron
g	e-h-pair generation density
g_i	e-h-pair generation density of the i-th volume element
g_m	mean e-h-pair generation density
$g_{m,K\text{-}O}$	mean e-h-pair generation density according to Kanaya-Okayama
$g_{m,MC}$	mean e-h-pair generation density from Monte-Carlo methods
H	interface recombination factor
h	planck constant
I_b	electron beam current
I_{CL}	luminescence intensity
IR_{back}	CL peak intensity ratio in back configuration
IR_{front}	CL peak intensity ratio in front configuration
j_0	diode saturation current density
j_n	conduction-band current density

j_{ph}	generated photo-current density	T	sample temperature
j_{sc}	short-circuit current density	T_{crit}	critical temperature for diffusion
K	compensation ratio	T_e	effective electron temperature
k	power exponent in power dependent luminescence analysis	$T_{lattice}$	effective lattice temperature
k_B	Boltzmann constant	t_{ann}	annealing time
L_{coll}	combined collection length	t_{drift}	drift time
L_{diff}	diffusion length	V_{bi}	built-in field
L_{drift}	drift length	V_{oc}	open-circuit voltage
L_{opt}	optical losses of a solar cell	v_{drift}	drift velocity
m_e	electron mass	w_g	width of the generation density distribution
m_e*	effective electron mass	w_G	distribution width of Gaussian defects
N_A	acceptor concentration		
N_C	conduction band density of states	w_n	width of the injection density distribution
N_D	donor concentration		
N_{DG}, N_{AG}	density of Gaussian donor/acceptor defects	w_{SCR}	width of the space-charge region
		x,y	lateral coordinates
N_e	number of incident electrons hitting the sample during one charge carrier lifetime	x_{90}	lateral 90% quantile of electron energy deposition
		Y_{be}	electron backscatter yield
N_I	density of ionized defects	Z	average atomic number of a sample
N_V	valence band density of states		
N_{ph}	number of incident photons per lifetime	z	depth coordinate
		z'	depth of origin of the emission at E_{detect}
n	free electron density		
n_{id}	diode ideality factor	z_0	depth of excitation of e-h-pairs
n_1, n_2	refractive indices	z_{90}	vertical 90% quantile of electron energy deposition
P	power		
p	free hole density	z_{max}	depth of local intensity maxima observed in CL profiling in cross-section geometry
R	reflectivity		
$R(g_k)$	relative generation of e-h-pairs at or below the generation density g_k		
		α	absorption coefficient
$R(\Delta n)$	relative generation of e-h-pairs at or below the injection density Δn	χ_e	electron affinity
		ΔE_C	conduction band off-set
$R(z,z_0)$	recombination in the depth z after excitation at z_0	$\Delta \phi_b$	electron barrier height
		Δn	electron injection density
R_s	series resistance	Δn_m	mean electron injection density
R_{sh}	shunt resistance	$\Delta n_{m,min}$	minimum mean electron injection density
r	distance of donor- and acceptor-like defects		
S_e	electron Seebeck coefficient	ΔV_i	i-th volume element
s_e, s_h	thermal velocity of electrons and holes	Δz_{max}	shift of the peak maximum z_{max} relative to the origin of the emission z'

$\varepsilon(z)$, $\varepsilon(x)$	energy loss per depth and lateral distance
ε	relative permittivity
ε_0	dielectric permittivity of free space
γ	average amplitude of fluctuation
γ_{opt}	average amplitude of fluctuation being active in optical transitions
λ	wavelength
μ_e/μ_h	electron/hole mobility
η	solar cell efficiency
η_{rad}	radiative recombination efficiency
ν	frequency
θ_c	critical angle of total internal reflection
ρ	mass density
σ	standard deviation
σ_e/σ_h	electron/hole capture cross section
τ_e/τ_h	electron/hole lifetime
$\tau_{e,free}$	free electron lifetime (before trapping)
$\tau_{e,trap}$	electron lifetime in a trap state

Abbreviations

ALE	atomic layer epitaxy
AQE	apparent quantum efficiency
AR	anti-reflective
BB	band-to-band
BF	bound-to-free
BX	bound-exciton
Casino	monte-carlo simulation of electron trajectory in solids
CBD	chemical bath deposition
CGSe	$CuGaSe_2$
CIGSe	$Cu(In,Ga)Se_2$
CISe	$CuInSe_2$
CL	cathodoluminescence
CSS	close-space sublimation
CTE	coefficient of thermal expansion
Cu/III	atomic ratio [Cu]/([Ga]+[In])

C-V	capacitance-voltage
DA	donor-acceptor pair
DC	direct current
DTA	differential thermo-analysis
EBIC	electron beam induced current
EDS	energy dispersive X-ray spectroscopy
e-h-pair	electron-hole-pair
EL	electroluminescence
EQE	external quantum efficiency
FB	free-to-bound
FWHM	full-width half maximum
FX	free-exciton
GGI	atomic ratio [Ga]/([Ga]+[In])
HT	high-temperature, T = 610°C
HZB	Helmholtz-Zentrum Berlin
IFK	Institut für Festkörperphysik Jena
ILGAR	ion layer gas reaction
j-V	current density-voltage
LLS	laser-light scattering
LT	low-temperature, T = 530°C
MPP	maximum power point
PE	partial electrolyte
PL	photoluminescence
PLE	photoluminescence excitation spectroscopy
qDAP	quasi-donor-acceptor pair
RF	radio-frequency
RTP	rapid thermal processing
SCAPS	solar cell capacitance simulator, a thin-film device simulator
SCR	space-charge region
SE	secondary electron
SEM	scanning electron microscopy
SIMS	secondary ion mass spectroscopy
SRIM	stopping and range of ions in matter, a monte-carlo code
STEM	scanning transmission electron microscopy
TEM	transmission electron microscopy
XRD	X-ray diffraction
XRF	X-ray fluorescence spectroscopy

List of publications and presentations

Haarstrich J., Metzner H., Oertel M., Ronning C., Rissom T., Kaufmann C.A., Unold T., Schock
H.W., Windeln J., Mannstadt W., Rudigier-Voigt E.,
*Increased homogeneity and open-circuit voltage of Cu(In,Ga)Se$_2$ solar cells due to higher
deposition temperature*,
Solar Energy Materials and Solar Cells **95**(3) (2011) 1028-1030.

Haarstrich J., Metzner H., Ronning C., Rissom T., Kaufmann C.A., Schock H.W., Mannstadt W.,
Rudigier-Voigt E., Scheumann V.,
Near-interface doping by ion implantation in Cu(In,Ga)Se$_2$ solar cells,
Thin Solid Films (2011), doi: 10.1016/j.tsf.2010.1012.1090.
also presented as a poster on the Spring Meeting of the European Material Research Society
(EMRS) in June 2010 in Strasburg and as a talk on the "First International Workshop on CIGS
Solar Cell Technology" (part of the Second Thin-Film Week) in April 2010 in Berlin.

Haarstrich J., Metzner H., Ronning C., Undisz A., Rissom T., Kaufmann C.A., Schock H.W.
Luminescence properties of Ga-graded Cu(In,Ga)Se$_2$ thin films
presented as a talk on the Frühjahrstagung of the Deutsche Physikalische Gesellschaft DPG in
March 2011 in Dresden and submitted to Thin Solid Films.

Windeln J., Schock H.W., Felser C., Metzner H., Mannstadt W., Klenk R., Gruhn T., Kaufmann
C.A., Rudigier-Voigt E., Speit B., Haag M., Rissom T., Kieven D., Ludwig C., Haarstrich J.,
Oertel M.,
comCIGS - integrative framework of experimental and virtual lab,
Proceedings of the 24th EU PVSEC Hamburg (2009).

Oertel M., Götz S., Cieslak J., Haarstrich J., Metzner H., Wesch W.,
*Measurement of the zinc oxide-molybdenum specific contact resistance for applications in
Cu(In,Ga)Se$_2$-technology*,
Thin Solid Films (2011) doi: 10.1016/j.tsf.2010.1012.1183.

Lebenslauf

Persönliche Daten

Name   Jakob Haarstrich geb. Reinisch
Adresse   Herderstraße 47
                07743 Jena

Geboren   am 07.02.1982
                in Bergisch Gladbach

Familienstand verheiratet
Kinder   2

Schulbildung

08/1988 – 06/2001   Besuch der Freien Waldorfschule in Wiesbaden
                            Abschluss: Abitur

Zivildienst

07/2001 – 07/2002   offiziell: Anderer Dienst im Ausland,
                            Camphill Kyle Community, Co. Kilkenny, Irland

Studium und beruflicher Werdegang

10/2002 – 09/2003   Studium Physik (Diplom) an der Friedrich-Schiller-Universität Jena

10/2003 – 06/2007   Studium Physik und Mathematik für das Lehramt am Gymnasium an der Friedrich-Schiller-Universität Jena, Abschluss: 1. Staatsexamen

05/2006 – 11/2006   Staatsexamensarbeit am Institut für Festkörperphysik der Friedrich-Schiller-Universität Jena zum Thema „Einfluss der Prozessbedingungen auf das Ätzverhalten von ionenbestrahltem $LiNbO_3$"

07/2007 bis heute   Wissenschaftlicher Mitarbeiter und Doktorand am Institut für Festkörperphysik der Friedrich-Schiller-Universität Jena Arbeitsgruppe Dünnschichtphotovoltaik

Ehrenwörtliche Erklärung

Ich erkläre hiermit ehrenwörtlich, dass ich die vorliegende Arbeit selbständig, ohne unzulässige Hilfe Dritter und ohne Benutzung anderer als der angegebenen Hilfsmittel und Literatur angefertigt habe. Die aus anderen Quellen direkt oder indirekt übernommenen Daten und Konzepte sind unter Angabe der Quelle gekennzeichnet.

Bei der Auswahl und Auswertung folgenden Materials haben mir die nachstehend aufgeführten Personen in der jeweils beschriebenen Weise unentgeltlich geholfen:

- Die $Cu(In,Ga)Se_2$ Absorberschichten wurden von Dr. Thorsten Rissom am HZB abgeschieden.
- Dr. W. Mannstadt und V. Scheumann führten die SIMS-Messungen bei der Schott AG in Mainz durch und stellten die Daten zur Verfügung.
- Proben, die von Marc Teichmann im Rahmen seiner Diplomarbeit am IFK hergestellt und vermessen wurden, wurden auch in dieser Arbeit verwendet.
- Die TEM-Bilder und TEM-EDS Spektren wurden am Institut für Materialwissenschaft und Werkstofftechnologie der FSU Jena von Dr. A. Undisz aufgenommen.
- Die Ionenimplantationen wurden von Gerald Lenk durchgeführt.

Weitere Personen waren an der inhaltlich-materiellen Erstellung der vorliegenden Arbeit nicht beteiligt. Insbesondere habe ich hierfür nicht die entgeltliche Hilfe von Vermittlungs- bzw. Beratungsdiensten (Promotionsberater oder andere Personen) in Anspruch genommen. Niemand hat von mir unmittelbar oder mittelbar geldwerte Leistungen für die Arbeiten erhalten, die im Zusammenhang mit dem Inhalt der vorgelegten Dissertation stehen.

Die Arbeit wurde bisher weder im In- noch im Ausland in gleicher oder ähnlicher Form einer anderen Prüfungsbehörde vorgelegt.
Die geltende Prüfungsordnung der Physikalisch-Astronomischen Fakultät ist mir bekannt.

Ich versichere ehrenwörtlich, dass ich nach bestem Wissen die reine Wahrheit gesagt und nichts verschwiegen habe.

Jena, den 11. Juli 2011 _____

Jakob Haarstrich